UNIVERSITÀ DEGLI STUDI DI TRIESTE

XXIX CICLO DEL DOTTORATO DI RICERCA IN

NANOTECNOLOGIE

New protocols to process advanced materials for the rewenable energy

Settore scientifico-disciplinare: **FIS/03**

DOTTORANDO
NICOLA CEFARIN

COORDINATORE
PROF. LUCIA PASQUATO

SUPERVISORE DI TESI
DR. MASSIMO TORMEN

ANNO ACCADEMICO 2015/2016

UNIVERSITÀ DEGLI STUDI DI TRIESTE

GRADUATE SCHOOL OF NANOTECHNOLOGY

XXIX CYCLE – 2014/2016

New Protocols to Process Advanced Materials for Renewable Energy

Candidate

Cefarin Nicola

Advisor

Dr. Tormen Massimo

Institutions

Università degli studi di Trieste
Piazzale Europa, 1
34127 Trieste, Italy
www.units.it
Graduate School of Nanotechnology
c/o Dipartimento di Fisica
Università di Trieste
Via A.Valerio, 2
34127 Trieste, Italy
www.nanotech.units.it

CNR – Istituto Officina dei Materiali
Laboratorio TASC
Area Science Park – Basovizza
Edificio MM
S.S. 14, km 163.5
34149 Trieste, Italy

LBL - Lawrence Berkeley National Laboratory
1 Cyclotron Rd
Berkeley, CA 94720
United States

JCAP - Joint Center for Artificial Photosynthesis
Lawrence Berkley National Laboratory
1 Cyclotron Road, Mail Stop 30R0205
Berkeley, CA 94720
United State

Molecular Foundry
Lawrence Berkley National Laboratory
67 Cyclotron Rd
Berkeley, CA 94720
United States

Table of Contents

Abbreviations

a.u.: arbitrary unit

AFM: atomic force microscopy

AM: air mass

Au: gold

CB: conduction band

cps: counts per second

c-TiO_2: compact-TiO_2

DMF: dimethylformamide

DSSC: dye sensitized solar cell

Eg: energy band gap

ETM: electron transporting material

eV: electron-volt

FAPI: formamidinium lead iodide

FF: fill factor

FTO: fluorine doped tin oxide

HTM: hole transporting material

IPA: isopropyl alcohol

ITO: indium tin oxide

J_{SC}: short circuit current density

LBNL: Lawrence Berkeley National Laboratory

LED: light emitting diode

LP-VASP: low pressure vapor assisted solution process

MABr: methylammonium bromide

MAI: methylammonium iodide

MAPI: methylammonium lead iodide

pc-AFM: photoconductive atomic force microscopy

PCE: power conversion efficiency

PL: photoluminescence

PMMA: poly(methyl methacrylate)

p-SC: perovskite solar cell

PV: photovoltaic

R_S: series resistance

R_{SH}: shunt resistance

RT: room temperature

SC: solar cell

SEM: scanning electron microscopi

Spiro-OMeTAD: 2,2',7,7'-tetrakis-(N,N-di-4-methoxyphenylamino)-9,9'-spirobifluorene

ss-DSSC soli state-dye sensitized solar cell

UV-vis: ultraviolet-visible

VB: valence band

V_{OC}: open-circuit voltage

XRD: X-ray diffraction

η: efficiency

Thesis Abstract

In this thesis growth control of organo-lead halide perovskite photoactive semiconductor layers is achieved by development of different synthetic processes. The optoelectronic properties of the as synthesized materials are characterized, and their suitability for fabrication of highly efficient PV devices is evaluated.

The hybrid organo-lead halide perovskite is an interesting material for photovoltaic technology due to its optoelectronic properties which allow to reach highly efficient solar cells (from ~4% to > 20%) in less than 8 years.[1–3] The chemical-physical properties as well as the morphology of the photoactive layer are highly dependent on the synthetic process used for the deposition, and some of these properties can be easily tuned by varying the chemical composition of the material (e.g. band gap), thereby making this material a versatile component of multijunction architectures.[4,5]

This Ph.D. project is focused on two different approaches that can improve the efficiency of the PV devices. First, efforts to direct the growth of organo-lead halide perovskite crystals are being discussed and evaluated. Electrical properties in these materials are affected by the orientation of the facets, and the fabrication approach of the p-SC should take in account a finite control of the halide perovskite deposition process. Thus, a layer of well faceted grains was deposited to study the facet dependence of the photo-generated current by means of photoconductive atomic force microscopy.

Second, I used nano-imprinting techniques to pattern organo-lead halide perovskites. Interestingly, in silicon based solar cells, the absorbing material is micro-structured to avoid radiation/material losses due to the optical phenomena such as light reflection.[6] The same strategy is here proposed to induce the total internal reflection phenomenon at the interface between the methylammonium lead iodide perovskite and the hole transporting material (Spiro-OMeTAD) exploiting the difference in refractive index between the two materials.

In the first chapter, a general introduction to the need of developing highly efficient and cost-effective solar cells is provided. The energy crisis and the photovoltaic (PV) technology are briefly described. Then, the physics of a solar cell and the existing PV

technologies are reported as well as an historical overview to introduce the perovskite-based solar cells, starting from the dye-sensitized solar cell (DSSC). Hence, the optoelectronic properties of the organo-lead halide perovskite are reported, followed by the description of the deposition methods. The chapter concludes with some general information about the characterization of the solar cell efficiency.

In the second chapter, the low pressure vapor assisted solution process (LP-VASP) is reported as useful method to deposit organo-lead halide perovskite: the layer is here characterized. Moreover the synthesis and the deposition of cubic-like methylammonium lead iodide crystals is described.

In the third chapter, the fabrication and characterization of solar cell devices are described. The final device has an efficiency close to 16% and hysteresis is almost not present. In particular the photoactive material is deposited with three different methods: the LP-VASP, the sequential dipping deposition and the combination of both of them. Then the PL and pc-AFM characterization of the layers described in chapter 2 are reported.

In the fourth chapter, it is reported the idea to design, develop and apply nanoimprint lithography for patterning of the photoactive material. Silicon masters with suitable nano-structures (pyramids and V-groove) were fabricated and used to transfer the desired pattern on the semiconducting layer.

1. Park, N.-G., Grätzel, M. & Miyasaka, T. *Organic-Inorganic Halide Perovskite Photovoltaics*. *Organic-Inorganic Halide Perovskite Photovoltaics* (2016). doi:10.1007/978-3-319-35114-8_4
2. Zhang, W., Eperon, G. E. & Snaith, H. J. Metal halide perovskites for energy applications. *Nat. Energy* 16048 (2016). doi:10.1038/nenergy.2016.48
3. Manser, J. S., Christians, J. A. & Kamat, P. V. Intriguing Optoelectronic Properties of Metal Halide Perovskites. (2016). doi:10.1021/acs.chemrev.6b00136
4. Zheng, L. *et al.* Morphology control of the perovskite films for efficient solar cells. *Dalt. Trans.* **44,** 10582–10593 (2015).
5. Nazeeruddin, M. K. & Snaith, H. Methylammonium lead triiodide perovskite solar cells: A new paradigm in photovoltaics. *MRS Bull.* **40,** 641–645 (2015).
6. Dzhafarov, T. in *Solar Cells - Research and Application Perspectives* (ed. Morales-Acevedo, A.) 386 (InTech, 2016).

1. Introduction

This chapter gives a brief introduction to the main topics that represent the subject of this thesis: photovoltaic (PV) technology, the physics of a solar cell, and organo-lead halide perovskite as a new promising material for PV technology.

1.1. The Energy Crisis: a Techno-Economical Overview

The energy demand increases year after year leading the community to face the energetic problem from several points of view. Despite the general trend of the increasing energy demand it is important to highlight that this growth slowed down in the last two years: the yearly increase, averaged in the last 10-years period, is about 1.9% while in 2014 the world consumption increased 1.1% and in 2015 around 1.0%.[1] The increasing energy demand comes mainly from the developing countries belonging to the Asian and African continents while among the countries the main users are China as well as the United States followed by India.[2] it is well known, that electricity (18.1%) is one of the energy supply and it is mainly produced from fossil sources as coal, oil (petroleum) and natural gases.[3] These resources exist in a limited amount and according to recent studies and projections published by BP (British Petroleum) they should be finished in the next two hundred of years.[2]As reported in the graphs below the 66.7% of the generated electricity comes from fossil fuels, 10.6% from the nuclear conversion and around 23% from clean and renewable resources as hydro and others (geothermal, wind and solar).[3]

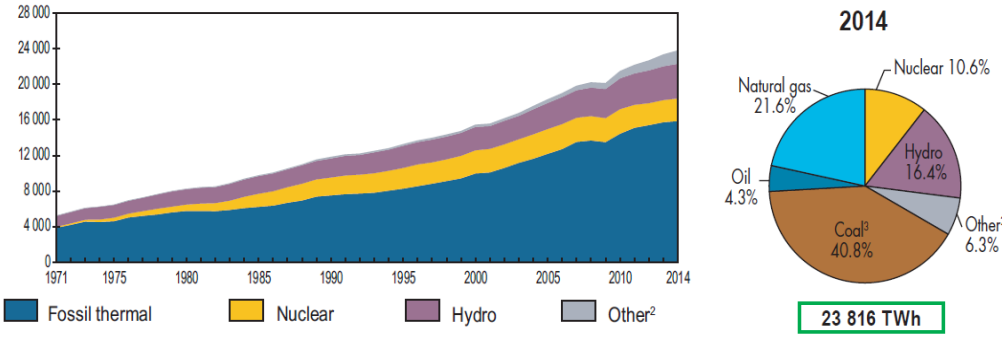

Figure 1.1: On the left **the world electricity generation1 from 1971 to 2014 by fuel (TWh). On the right the fuel shares of electricity generation in 2014.**[3]

While the deposits are running out of the nonrenewable material (fossil fuels and elements as uranium for nuclear production), the formation of new veins suitable for the extraction process is too slow (millions of years): from this point of view in the last decades the problem of finding alternative resource to generate electricity and more energy is raised.

Moreover the nonrenewable sources entail several environmental issues: the CO_2 production, the main responsible for the greenhouse effect and the consequent world temperature increase,[4] the emission of pollutants as side products, and the poisoning of the soil or the seas due to accidental spills during the extraction or transport processes.

The world community is not new to these aspects, while several international and national agencies have pushed the political-economical organs to adopt solutions to face and solve the aforementioned issues. The so called renewable sources are the most promising candidates to produce clean energy: basically this sources are “unlimited” and a huge amount of energy could be generated from their conversion. The renewable sources are appealing due to the fact that the production of CO_2 pollutants is limited, lowering the general poisoning of the planet due to the fossil fuels and the generated waste.

Although at this point it is easy to understand that the future the renewable sources will become the main type of energy supply, at the moment economical factors are still favoring the use of fossil fuels. To date the electricity cost produced with the green technologies is still higher than that one generated with the conventional energy implants.

Thanks to the improvements linked to scientific and technological research and by knocking down the production costs with large scale productions, the generation costs of the green electricity are getting closer and closer to the parity with fossil fuels. In particular, in some regions of the world sun radiations converted with the photovoltaic (PV) devices gives electricity with comparable cost to that of electricity produced with fossil sources.[5]

Since the present Ph.D. project is focused on the photovoltaic technology the introduction to the others clean sources as hydro and wind will not be treated here in order to keep the reading as light as possible.

1.2. Photovoltaic Technology

The PV technology is based on the physic of the semiconducting materials where the sunlight radiation is converted into electrical energy. This is due to the so called photovoltaic effect that has its origins in the photoelectric effect, experimentally demonstrated for the first time by the Edmonde Bequerelle in 1839.

The quantity of light absorbed by a semiconductor depends on the band gap energy but also on the spectrum of the incoming light. The sun can be considered as a black body at 6000K and its spectrum is shown in **Figure 1.2**.

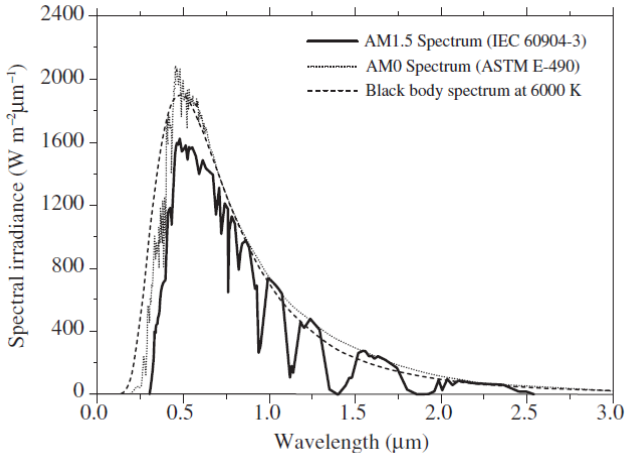

Figure 1.2: Spectral distribution of the solar spectra outside the atmosphere (AM0) and at the earth's surface at α ≈ 45° (AM1.5) compared to the black body spectrum.

It is important to take into account that the light passing through the Earth atmosphere is attenuated, with the consequential change in the solar spectrum. This is due to the interaction of photons with the different molecules present in the air as for example water, oxygen and carbon dioxide. The attenuation effect is characterized by the "Air Mass" coefficient $AM = 1/\cos\alpha$,where α is the angle between the solar ray and the Zenith **Figure 1.3**).

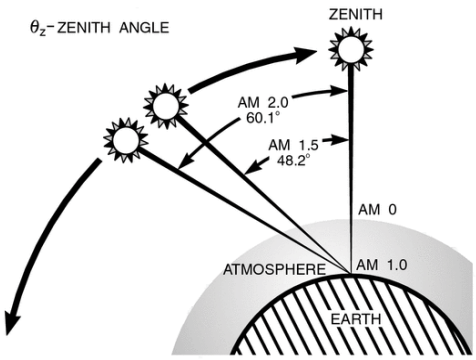

Figure 1.3: Air mass index for different angles.

Thus AM0 corresponds to the spectrum outside the atmosphere, AM1on the earth's surface when the rays are perpendicular meanwhile spectrum with higher air mass coefficient like AM3 correspond to the sunlight during morning and evening when is almost horizontal. The AM1.5 is considered the standard value for characterization of solar devices and corresponds to the average illumination a PV-module receives during the day. In order to have a standard spectrum for the efficiency characterization of the devices, also the intensity of the incoming sunlight is generally normalized to 1000W/m^2.

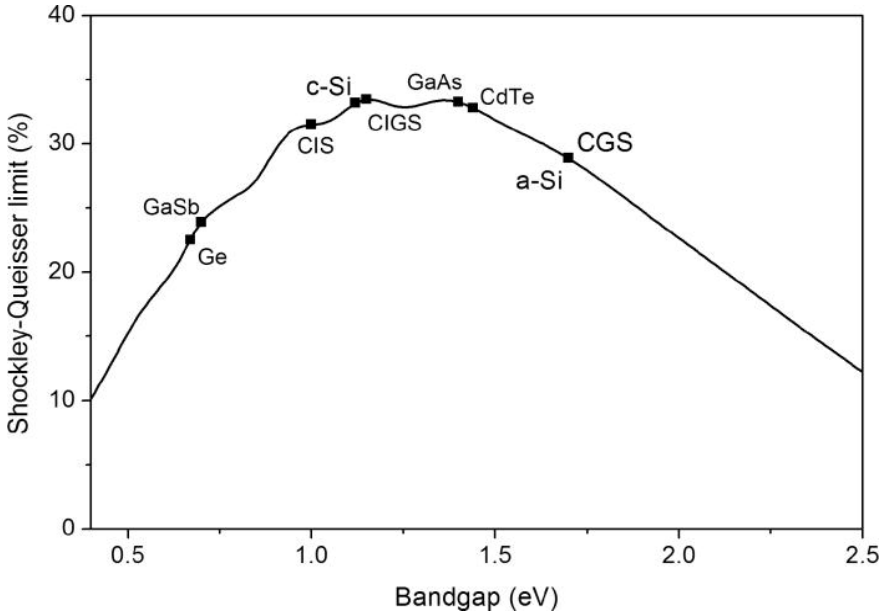

Figure 1.4: Limiting efficiency curve for a single band-gap solar cell under AM1.5 illumination. The points represent the best experimental single band-gap cells fabricated to date.

In the present graph the black line represents the "Shockley-Quessier" limit (SQ-limit) under AM1.5 conditions: in particular the line shows the theoretical maximum efficiency as a function of the semiconductor band gap (**Figure 1.4**). The SQ-limit is valid only for single junction SC whereas with the multi-junction technology it is possible to overcome this efficiency limit.

From the SQ-limit curve it is possible to appreciate that for the semiconductors with band gap between 1.0eV and 1.5 eV the highest expected efficiencies are around 31-33%. The next page shows the NREL chart with the updated (January 2017) Best Research-Cell Efficiencies for the different technologies and semiconducting materials. Moreover, it is interesting to follow the efficiency improvements made in the last 40 years for a specific type of SC (**Figure 1.5**).

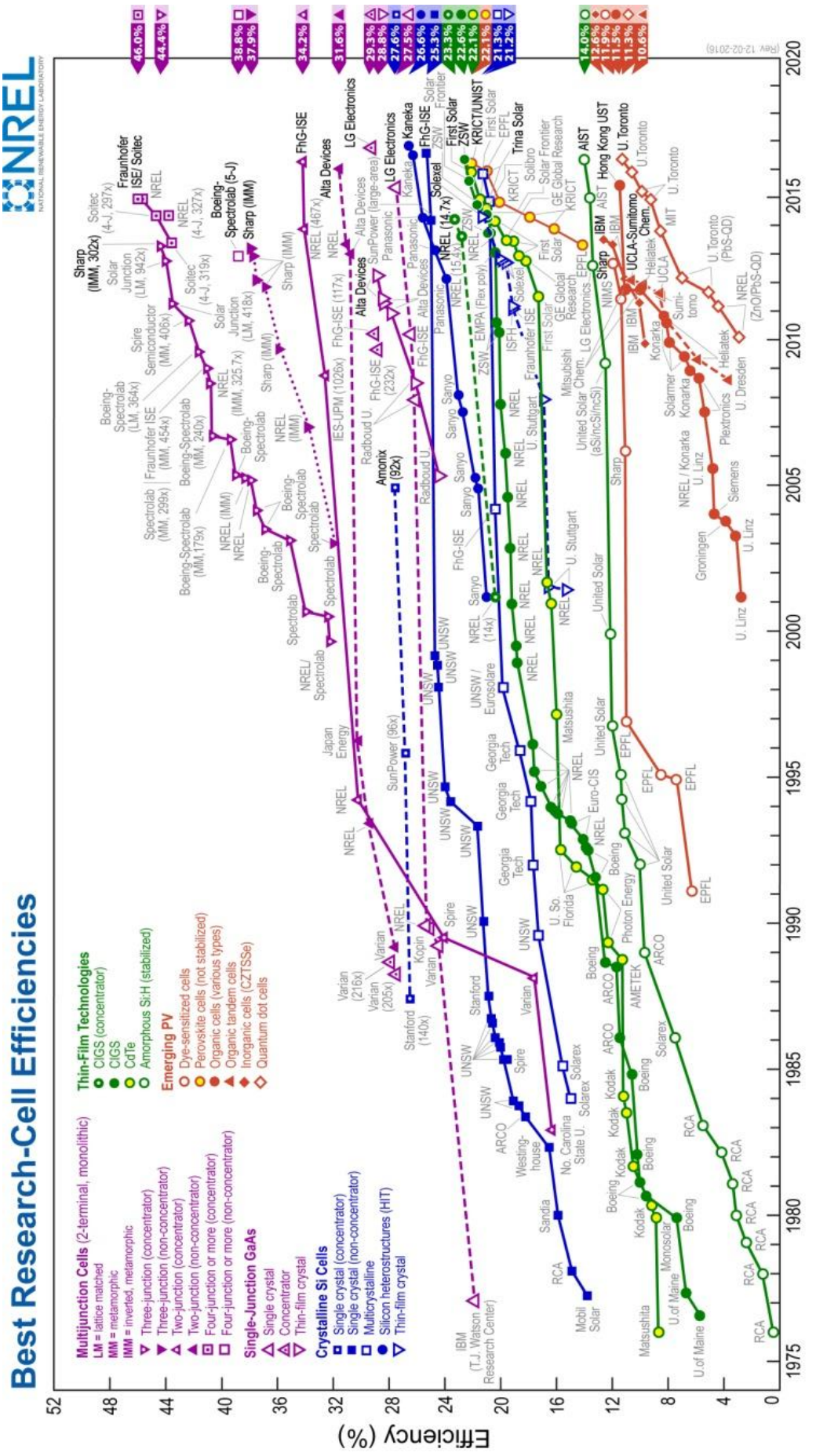

Figure 1.5: Efficiency chart of PV technology (updated January, 2017)[10]

1.3. Solar Cell Physics

The photovoltaic effect is responsible for the conversion of the light energy into electrical energy. In general this phenomenon occurs in a semiconductor due to its electronic structure: this class of materials has a valence band (VB) of occupied states and a conduction band (CB) of unoccupied conductive levels divided by a difference in energy, called band gap or energy gap (E_g) (**Figure 1.6**).

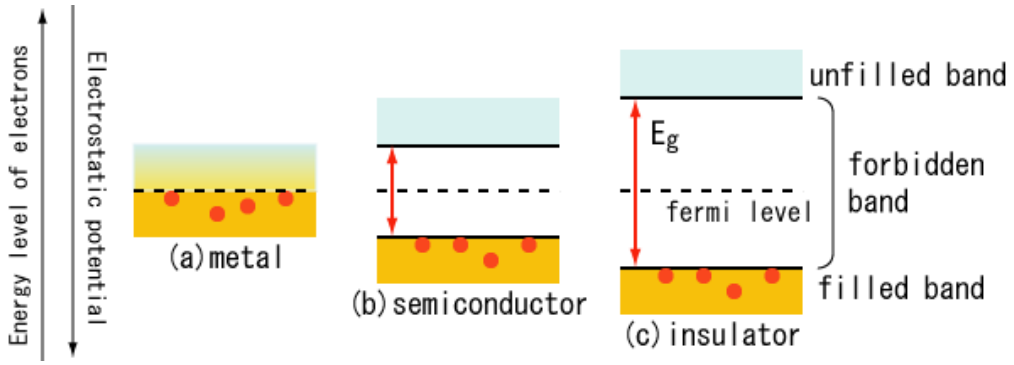

Figure 1.6: Electronic structure at the edge bands for a metal (a), a semiconductor (b) and an insulator (c). Downloaded from https://commons.wikimedia.org/wiki/File:BandGap-Comparison-withfermi-E.PNG

The entire process might be divided in two main steps:

1. Creation of the electron-hole pair by photon absorption;
2. Collection of the carriers to the electrodes.

In general when the light radiation hits the photoactive material, the photon energy (E_{hv}) is transferred to the VB electrons and three different scenario are possible (**Figure 1.7**). With $E_{hv} = E_g$ the electron may be promoted from the VB to the CB generating a single charge pair. Also when $E_{hv} > E_g$ the electron may be excited from the VB to the CB, then it loses the energy excess through thermalization process and relax to the CB minimum. In the end if $E_{hv} < E_g$ the electron absorbs the radiation and relax again to the VB.

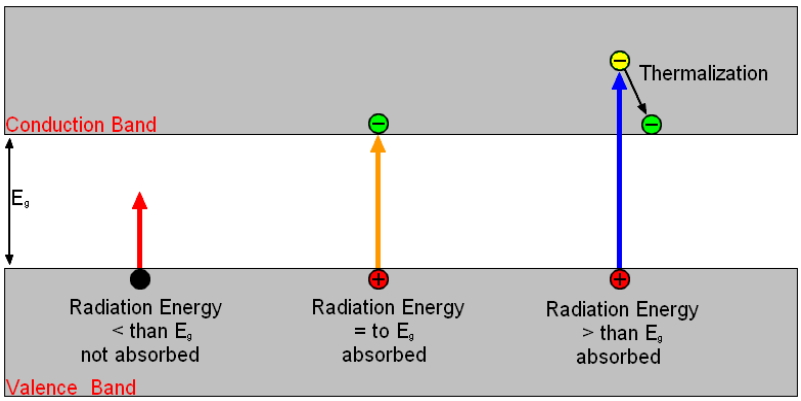

Figure 1.7: Scheme of the excitation due to photovoltaic effect. Example of excitation by photon with energy lower (red) equal (orange) and higher (blue) than E_g.

At this point it is important to introduce the concept of direct and indirect band gap since it deeply affects the probability of the absorption process (quantified by the absorption coefficient, α). This classification is due to the electronic structure of the semiconducting material: as reported in **Figure 1.8** it depends by the VB and CB overlapping in the reciprocal space (k-space). In a direct band gap semiconductors (GaAs, GaInP, CdTe, and Cu(InGa)Se_2) the transition probability from states close to the maximum of the VB and the minimum of the CB occurs virtually without transfer of momentum, and the absorption coefficient depends on the dipole transition elements and the density of initial and final electron states (**Figure 1.8a**). For the indirect band gap materials (Si and Ge), due to the small momentum associated to the absorbed photon, the energy-momentum conservation would not allow transition between the maximum of the VB and the minimum of the CB, as they are lying in different positions of the reciprocal space. In order to fulfill the momentum conservation the process of absorption of a photon requires the availability of phonons (either emitted or absorbed) providing the missing momentum (**Figure 1.8b**):

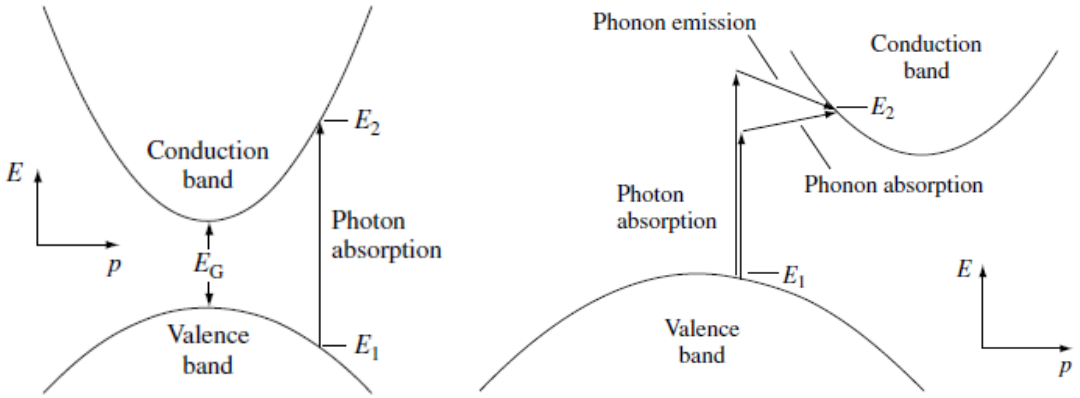

Figure 1.8:a) Photon absorption in a direct band gap semiconductor for an incident photon with energy hν = $E_2 - E_1$> EG. b) Photon absorption in an indirect band gap semiconductor for a photon with energy hν< $E_2 - E_1$ and a photon with energy hν> $E_2 - E_1$. Energy and momentum in each case are conserved by the absorption and emission of a phonon, respectively.[6]

After photon absorption the formed electron-hole pairs have to be separated and collected to the electrodes (second step), located at the opposite sides of the device. Depending on the material the electron-hole pair exists as separated carriers at room temperature (RT) as mostly in silicon and inorganic semiconductors or as a bound state (called exciton) as in organic semiconductors. In the case of halide perovskite the electrons and the holes dissociate at RT (as Silicon) and are thus free to migrate to the electrodes thanks to a built-in electric field generated from the diode configuration.

Two main architectures are found in PV devices: one is based on a p-n junction and the other on a p-i-n junction. In the first case the field is limited to the depletion region of the diode while in the second the field is extended over the whole intrinsic layer. Separation and collection are more efficient for higher internal electric field due to the built-in voltage (V_{bi}) present in higher band gap materials: this process results to be more efficient in the high band gap semiconductors.

1.4. Photovoltaic Generations

The first solar cell based on Silicon semiconductor was fabricated by the researchers Daryl Chapin, Calvin Souther Fuller and Gerald Pearson on April 25, 1954 at Bell Laboratories.[7] At the beginning the cost to produce a solar cell was high, so the devices were mainly used only for forefront technologies such as space applications; in particular the first module was installed in 1958 on the Vanguard I satellite.[8] The PV technology from that moment evolved for the next 60 years: several materials have been studied and optimized and engineering shrewdness has progressed, leading to high efficient and cheaper solar cells. The birth of different kinds of devices induced to classify them in three main generations:

- 1st generation: p-n junction based on crystalline silicon (c-Si);
- 2nd generation: thin film SC (cadmium telluride CdTe, copper indium gallium diselenide CIGS, amorphous thin-film silicon a-Si);
- 3rd generation: emerging technologies (organic SC, polymer SC, dye-sensitized SC, quantum dot SC, Perovskite SC).

The first generation of solar cells includes the devices with p-n junction based on doped bulk c-Si. In turn it is possible to divide the c-Si in two sub-classes, depending on the nature of the material: it is possible to have mono-crystalline (mono-Si) and multi/poly-crystalline (multi-Si or poly-Si) (**Figure 1.9**). In particular the photoactive layer (Si wafer) is properly doped creating n-type and p-type regions necessary to enhance the field driving the electrons and holes towards the electrodes after the formation of free carriers upon absorption of a photon. The best mono-Si device has reached a power to conversion efficiency of 25.3% due to the high purity of the photoactive layer while the

cheaper poly-Si solar cells reached an efficiency (η) of 21.2%.[10] In the last 15 years the production of the poly-Si technology increased and now covers around 70% of total market while at the same time around 23% of the devices are based on the mono-Si semiconductor: at the state of the art this class of PV covers over the 90% of the total market.[9]

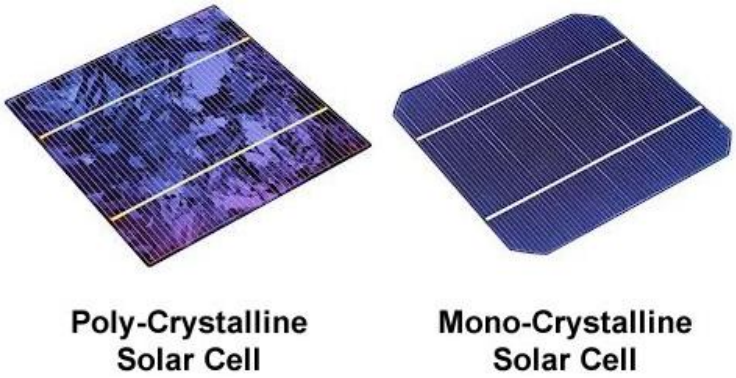

Figure 1.9: Poly-Crystalline solar cell and Mono-Crystalline solar cell.

Since high production costs was one of the first issues met for the technology development and scaling up, the researchers tried to figure out how to decrease the price of the whole process. They noticed the main factor affecting the overall cost(around the 65%) was the price of the silicon wafer while only the remaining 35% was due to the cell fabrication and the module assembly (**Figure 1.10**):[6]

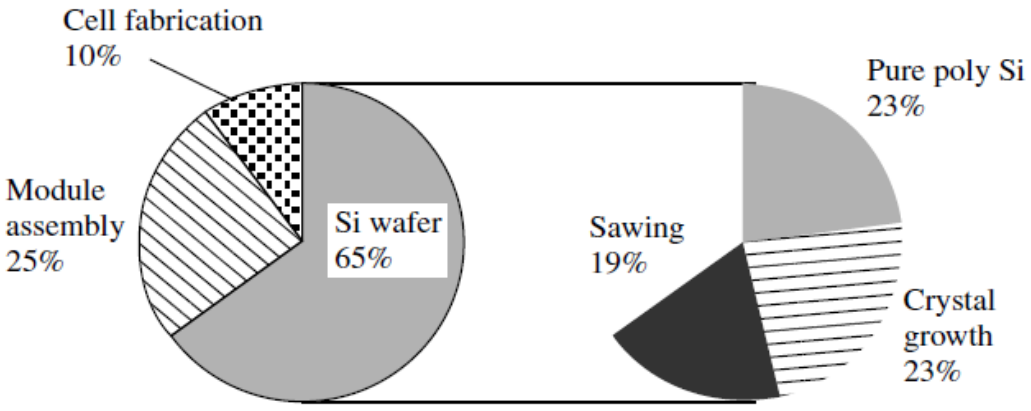

Figure 1.10: Cost breakdown of a silicon module.[6]

For this reason different semiconducting materials were taken in consideration leading to a new class of thin film solar cells, grouped in the so called second photovoltaic generation. The devices are characterized by the use of less semiconducting material since a thinner photoactive layer (from 1 to 10 microns) replaces the usual thicker wafer of the Si-based solar cell (200 microns). These devices are based on semiconducting materials of direct band gap, such as cadmium telluride (CdTe), copper indium gallium

diselenide (CIGS) or amorphous thin-film silicon (a-Si). Although in 2015 the production covers only the 7% of the market share in the recent past (2009) they had reached the 17%.[9] In general this class of solar cells was born to provide a cheaper alternative to the usual Si-based SC, obtained however at the price of lower efficiencies. While the a-Si SCs have a stabilized PCE of 14%, in the last years both the CdTe and the CIGS based devices were optimized closing the efficiency gap with the poly-Si SC, establishing the new record values to 22.1% and 22.6%, respectively.[10] Other advantages of these SCs are the shortest energy payback time among all the solar technologies (CdTe)[11] and the possibility to fabricate flexible cells on low weight plastic substrates (CIGS) (**Figure 1.11**). There are still some issues to solve as for example the lower long term stability due to the faster degradation compared to the Si-based SC, the toxicity of cadmium (CdTe)[12] and the limited amount of indium reserves (CIGS).[13]

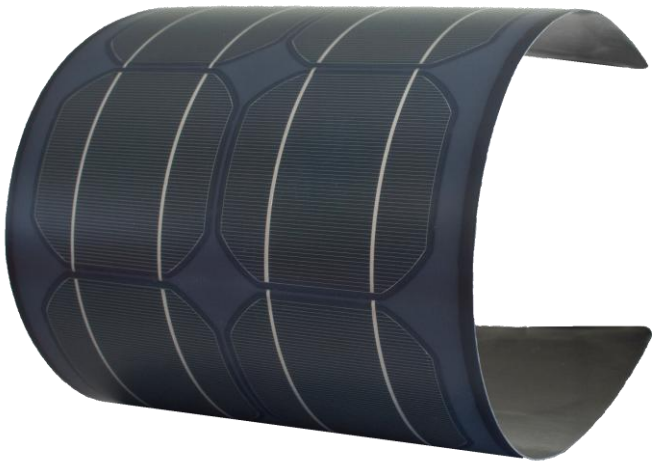

Figure 1.11: CIGS solar cells form a flexible module on plastic substrate.

The third generation photovoltaic cells include a pool of all the emerging technologies as for example the copper zinc tin sulfide (CZTS) SC, the organic SC, the polymer SC, the dye-sensitized solar cell (DSSC) and the Perovskite SC (p-SC). In this class are usually present also the so called tandem SC (two different stacked SC), the multi-junction (MJ) SC and the concentrator photovoltaics (CPV). The first two kinds of devices are composed by a stack of solar cells with different band gaps (from two up to four) resulting in high efficiency (from 31.6% up to 46.0%)[10], yet very expensive, cells. On the other side the CPV exploits mirrors and lenses to redirect and focus the radiation onto PV devices (usually the MJ-SC).

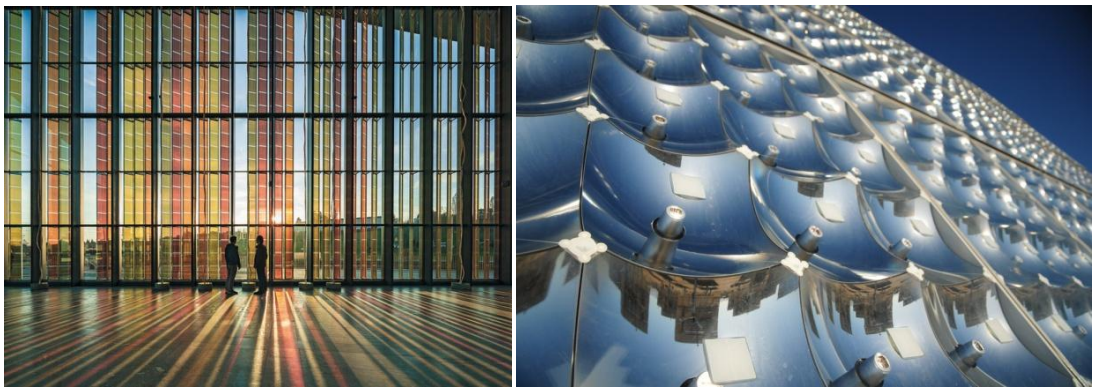

Figure 1.12: On the left the DSSC-panels installed at EPFL's SwissTech Convention Center. On the right a picture of the Concentrator PV (CPV).

The emerging SCs have been deeply studied in the last 15 years reaching up to now efficiencies between the 10 and 12%: only the dye-sensitized SC also known as "Grätzel cell" are older being born in the first 90s. The DSSCs are very interesting since it is possible to fabricate semi-transparent and colorful devices (**Figure 1.12**) giving the possibility to apply this technology also where the visual impact is a critical point. From the research on DSSC, through several optimizations, a new type of SC based on perovskite organic-inorganic semiconductor has emerged.

1.4.1. From the DSSC to the Perovskite-SC (p-SC)

In 1988 the DSSC was studied by Brian O'Regan and Michael Grätzel at UC Berkeley, in California (USA). Then the two researchers moved to the École Polytechnique Fédérale de Lausanne (EPFL) in Switzerland and in 1991 for the first time they published a paper on this kind of SC. The device is basically consisting of three main parts: there is a meso-porous TiO_2 scaffold, a dye (or photosensitizer) absorbing layer and the iodide liquid electrolyte. The radiation is absorbed by the photoactive layer (the dyes) creating excited electrons; those are injected into the TiO_2 transporting material and collected to the back contact. At the same time the oxidized photosensitizer is regenerated accepting electrons from present in the electrolyte solution. The so formed I_3^- is again reduced to I^- accepting electrons from the counter electrode. One of the main disadvantages of this architecture is the use of the iodide electrolyte: it partially absorbs the visible light (λ = 430 nm) and is responsible for the corrosion of the counter electrode (Pt or Au).[14]

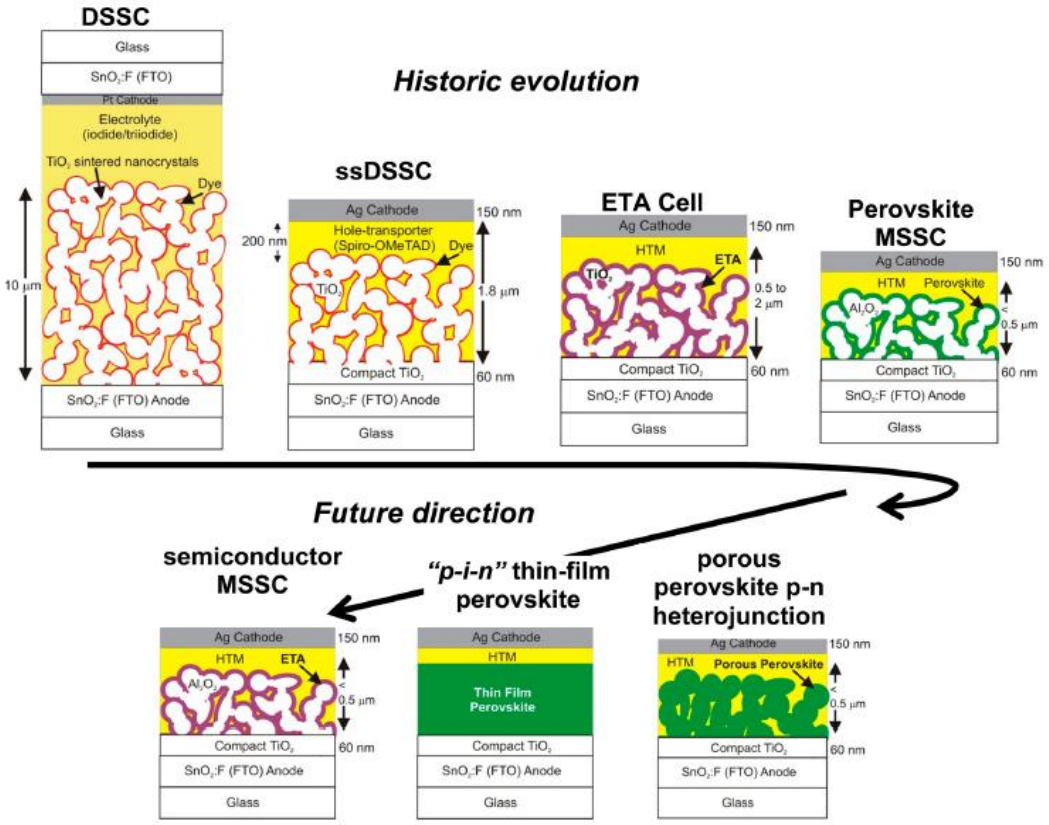

Figure 1.13: Historic evolution of the solar cell technology, starting from the electrolyte-based mesoscopic DSSC, the ssDSSC (with an organic p-type hole conductor), the ETA cell (with an Extremely Thin Absorber semiconductor layer), to the MSSC (with a perovskite absorber in a meso-superstructured architecture). On the bottom three evolutions of the "Grätzel cell".[15]

For this reason the natural evolution of the device was aiming at the replacement of the aforementioned electrolyte with a solid hole transporting material (HTM), that was found to be the organic 2,2',7,7'-tetrakis-(N,N-di-4-methoxyphenylamino)-9,9'-spirobifluorene (Spiro-OMeTAD), and leading to the branching of a new research line the so called solid state DSSC (ss-DSSC). Once the HTM was optimized different materials were explored to find more advanced photoactive absorbers: among these the methylammonium lead halide ($CH_3NH_3PbX_3$, X = I, Br and/or Cl) perovskite showed good properties.

In the years between 2006 and 2008 T. Miyasaka used this semiconductor to fabricate the first perovskite-based SC[15] and in 2009 for the first time he published about a sensitized solar cell with $CH_3NH_3PbI_3$ as photoactive layer and the iodide/triiodide red-ox couple with a PCE of 3.8%.[16] In 2011 at the Sungkyunkwan University, in Suwon (Korea), under N. G. Park's supervision the researchers optimized the TiO_2 nanocrystalline surface (still meso-porous) and obtained a SC with the final efficiency of 6.54%.[17] Also in

this case, as well as for the Grätzel cell, the main problem is the liquid electrolyte responsible for perovskite degradation or dissolution.[16,17]

The research groups lead by Grätzel, Park, Miyasaka and Snaith at that point decided to use the Spiro-OMeTAD to replace the iodide/triiodide electrolyte. After the optimization of the perovskite layer ($CH_3NH_3PbI_3$ and $CH_3NH_3PbI_{3-x}Cl_x$) they were able to reach efficiencies between 8% and 10%,[18,19] which were higher than the best ss-DSSC (7%).[20] This new material showed from the beginning outstanding properties which allow to overcome some fundamental and technical limitations: with a thickness of 500 nm, the perovskite layer absorbs completely and in a broader range the light resulting in a better photoactive material than the usual dyes. This aspect is very important considering that the thickness limitation (2 μm) for the ss-DSSC is one of the main reasons for the low light absorption and photocurrent generation exhibited by these devices.

The meso-superstructured solar cells (MSSC) composed by the TiO_2 porous scaffold, the perovskite photo-absorber and the organic HTM (Spiro-OMeTAD) became in very short time a hot topic among the emerging PV technologies. Since relatively high efficiencies were reached in few years and within few optimizations, the research community focused its attention to the optimization of the device while the perovskite properties were still unknown or only partially understood and characterized. At the Oxford University Henry J. Snaith, trying to study and clarify perovskite's semiconducting features, decided to fabricate a SC replacing the conductive TiO_2 scaffold with the insulating meso-porous Al_2O_3: in this new architecture the electrons are not anymore injected into the porous inert scaffold but are rather collected to the electrode passing through the same photoactive layer. Surprisingly the generated electricity with high efficiency (10.9%) proves the perovskite layer to act as an excellent intrinsic electron transporting layer and exhibiting low losses, since the open-circuit photovoltage generated is 1.1 V considering the band gap is around 1.55 eV.[19]

The evidences coming from this work suggested the possibility to avoid the use of the meso-porous TiO_2 scaffold, simplifying the architecture of the device to a thin film p-i-n (or n-i-p) structure: in particular the new stack is composed by a layer of planar and compact TiO_2 (n-type), the perovskite photoactive layer (i-type) and the Spiro-OMeTAD as organic HTL (p-type).

At that point the scientific community split in two big schools of thought: the first

one still focused on the meso-porous SC (**Figure 1.14a**) with Grätzel as main exponent and the second one betting on the new planar architecture (**Figure 1.14b**) promoted by Snaith.

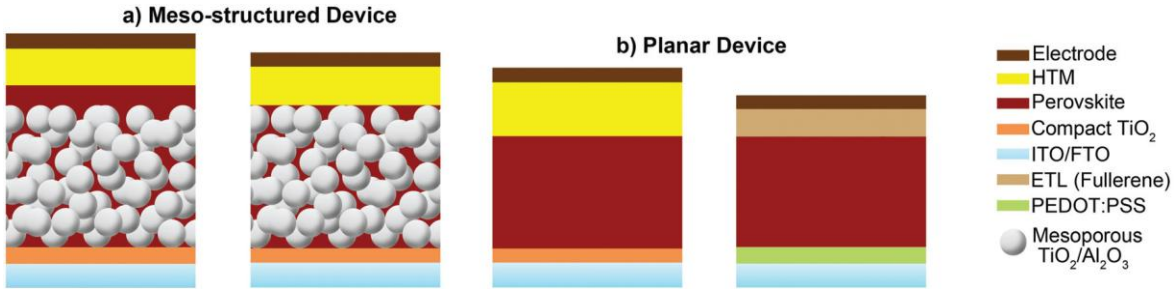

Figure 1.14: Diagram of the structure of (a) the meso-structured p-SC and (b) the planar p-SC.[21]

1.5. Perovskite Properties

Perovskite is the name of a crystallographic family including a huge amount of materials with relatively different properties. The discovery of the first oxide perovskite ($CaTiO_3$) is dated back to the 1839 by German mineralogist Gustav Rose, who decided to name this mineral family in honor of the Russian mineralogist Lev Aleksevich von Perovski. Among the several materials present in this family this project is focused on the hybrid organic-inorganic lead halide perovskites. These were first characterized in the late 70sby Weber while for the first implementation of a tin-based perovskite in a thin-film transistor it is necessary to wait for Mitzi's studies during the first 90s. As before reported the first p-SC was reported in 2009 while in 2014 the first organometal halide perovskite LED (Pe-LED) device was reported.[22]

1.5.1. Lattice Structure

The hybrid organic-inorganic metal halide perovskite (**Figure 1.15**) has the following general formula ABX_3 (or AMX_3): A stands for a cationic component usually an organic small molecule ($CH_3NH_3^+$) or an inorganic element as Cs^+, B is a metallic atom of $Pb^{2+}$and/or Sn^{2+} and X indicates one halide atom amongst Cl^-, Br^- and/or I^-.

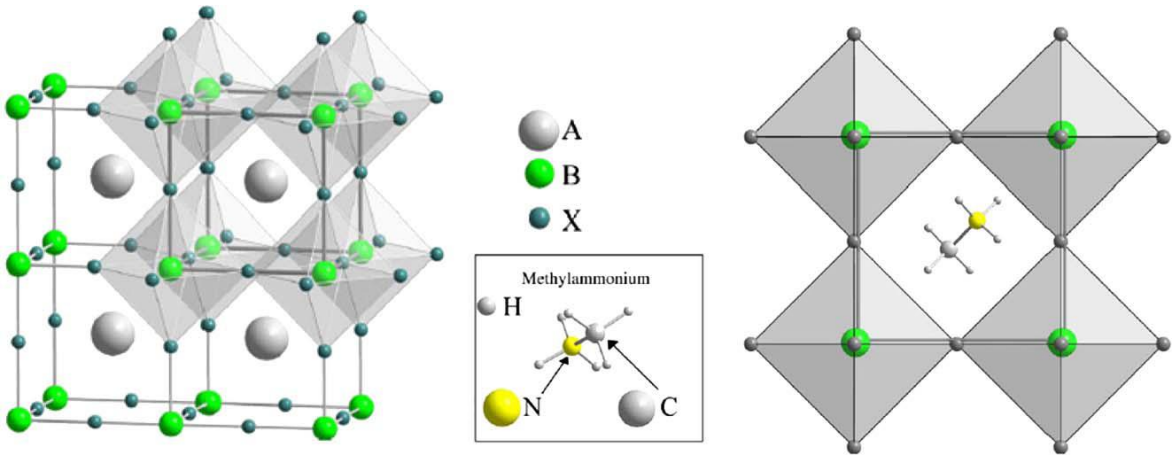

Figure 1.15:Unit cell of ABX_3Perovskite structure. The BX_6 corner-sharing octahedra are evidenced.[23]

In the usual ABX_3 structure the B component has an octahedral coordination with 6 X (halide) atoms while the A-site forms with 12 X atoms the AX_{12} polyhedron in cuboctahedral coordination.

The most common and deeply studied perovskite is the methylammonium lead iodide Perovksite ($CH_3NH_3PbI_3$) since was the first discovered surprisingly with excellent qualities. This specie, also known with acronym MAPI ($MAPbI_3$), exist in three different phases here reporter in order of increasing temperature: orthorhombic (T < 165 K), Tetragonal (165–327 K) and Cubic (T > 327 K).[24] The characteristics of the semiconducting material depend strongly on the morphology of the films and this gives the possibility to tune some physical, chemical and optoelectronic properties by varying specific synthesis parameters.

In order to be as clear as possible in the next paragraphs MAPI's properties are reported to give a general overview of these materials for PV applications, while some particular cases are mentioned to show its great prospective.

1.5.2. Electronic Structure, Optical and Charge Carrier Properties

From the first experiments $MAPbI_3$ resulted in a very promising material for the photovoltaic technology due to excellent physical-chemical properties. The energy band gap ($E_g \approx 1.6$ eV) allows to absorb along all the visible spectra (from $\lambda \approx 800$) maximizing the collection of the impinging photons while the high absorption coefficients $\alpha_{(\lambda)}$ (4.3 x

10^5 cm^{-1} at λ = 360 nm and 1.5 x 10^4 cm^{-1} at λ = 550 nm) ensure a high conversion rate of the photons in excited electrons. Moreover $MAPbI_3$ $\alpha_{(\lambda)}$ has values comparable or even higher than those of the high efficient organic SC and in the same range of the other PV semiconductors (**Figure 1.16**).[25,26]

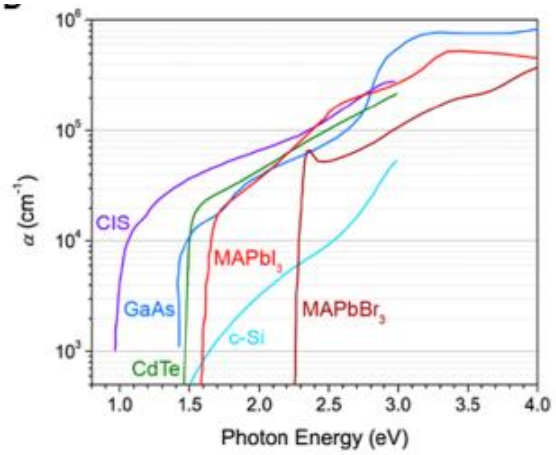

Figure 1.16: Experimentally determined absorption coefficients for $CH_3NH_3PbI_3$, $CH_3NH_3PbBr_3$and a number of other PV-relevant direct gap materials and indirect gap c-Si.[26]

The conduction band overlaps with the valence band (**Figure 1.17**) because the electronic structure at the band edges is mainly governed by the basic BX_6 electronic structure: this brings to be a direct band gap material.[27,28]

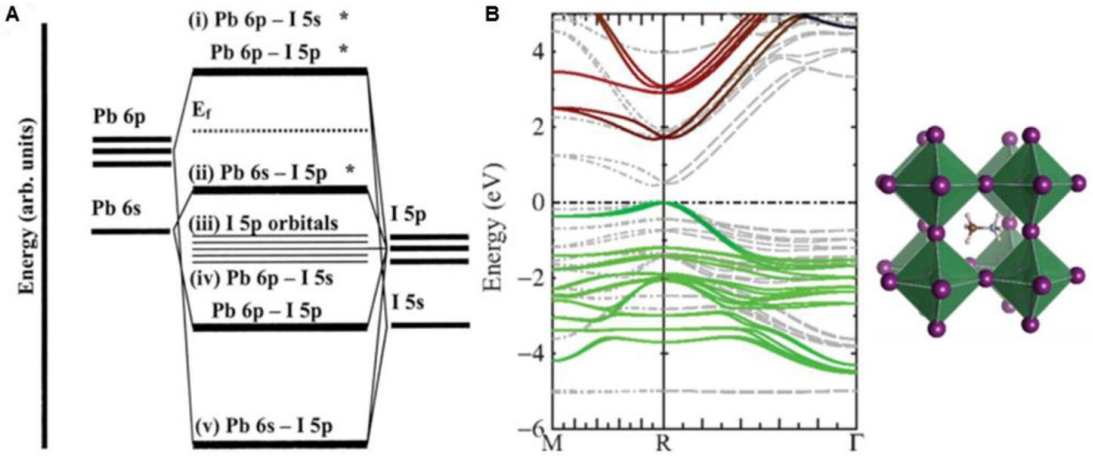

Figure 1.17: A) Bonding diagram of isolated $[PbI_6]^{4-}$octahedral. (B) Calculated electronic band structure of $CH_3NH_3PbI_3$: orbital contributions are indicated by I 5p (green), Pb 6p (red), and Pb 6s (blue).[26]

Among all the intriguing perovskite properties there are the carrier long diffusion lengths (0.1-1 μm for the polycrystalline layer and 175 μm for the single crystal) and high charge carrier mobility (up to ~100 cm^2/Vs) due to the low recombination rate and long lifetime (~100 ns).[21,28] Researchers explained with these good qualities, better electron-

hole separation (due to exciton binding energy comparable to the thermal energy) and reduced recombination losses, both necessary for the high efficiencies of the p-SC.

1.5.3. Perovskite Family as a "Coffee Blend"

Although the first perovskite studied and used for the p-CS was the $MAPbI_3$, thanks to the ABX_3 structure many components may be varied creating new materials. It is possible to change the organic methylammonium cation with other organic and inorganic species and the same might be done with the metallic site and the halide elements. It is possible to obtain pure, mixed and "multi-component mixed" phases: tuning the chemical composition it is possible to synthesize new semiconductors characterized by different properties: in particular it is possible to act on the band gap, the moisture stability, the photo-segregation, the recombination processes and many others.

One of the most interesting aspects is the possibility to tune the band gap (E_g) changing the chemical composition. The advantage in adjusting the energy gap results useful for the fabrication of the Si/perovskite tandem SC. From the theoretical calculations for the optimal working device it is necessary to stack onto the Si-SC (energy band gap of 1.1 eV) a cell with a suitable band gap that in this case is around E_g = 1.7 eV (**Figure 1.18**). It is important to keep in mind for a single SC the optimal absorption needs a semiconductor with a band gap between 1 and 1.5 eV, so increasing the band gap for the Perovskite is useful only to fabricate tandem SCs.

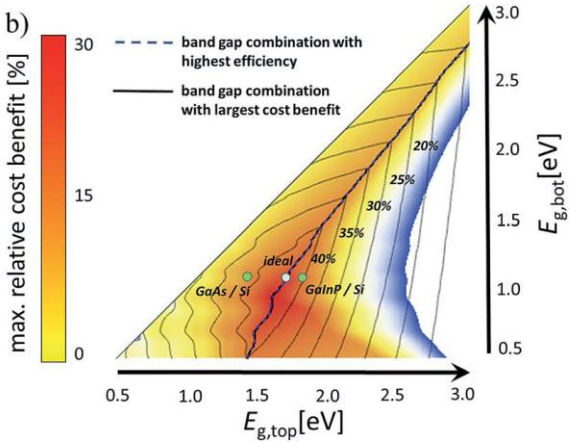

Figure 1.18: Maximum relative cost benefit as a function of top cell band-gap $E_{g,top}$ and bottom cell band-gap $E_{g,bot}$ for the two-SC configuration. The contours show the limiting efficiencies for the corresponding band-gap combination. The blue dotted line represents the band-gap pairing with the highest efficiency for a given $E_{g,top}$, $E_{g,bot}$.[30]

Hereafter some strategies to tune the perovskite band gap are reported. The substitution of the halide atoms was the first approach explored: as previously reported $CH_3NH_3PbI_3$ has an energy gap around 1.6 eV, while the pure bromide analogue

($CH_3NH_3PbBr_3$) absorbs at lower wavelengths (λ ≈ 540 nm) due to a higher band gap (E_g ≈ 2.3 eV) and the methylammonium lead chloride ($CH_3NH_3PbCl_3$)has a even wider bad gap E_g ≈ 2.88 eV (λ ≈ 430 nm). Even more interesting is the possibility to synthesize mixed phases $CH_3NH_3PbI_{3-x}Br_x$ (**Figure 1.19**) simply varying the I/Br ratio and tuning the final band gap (between 1.6-2.3 eV).[29]

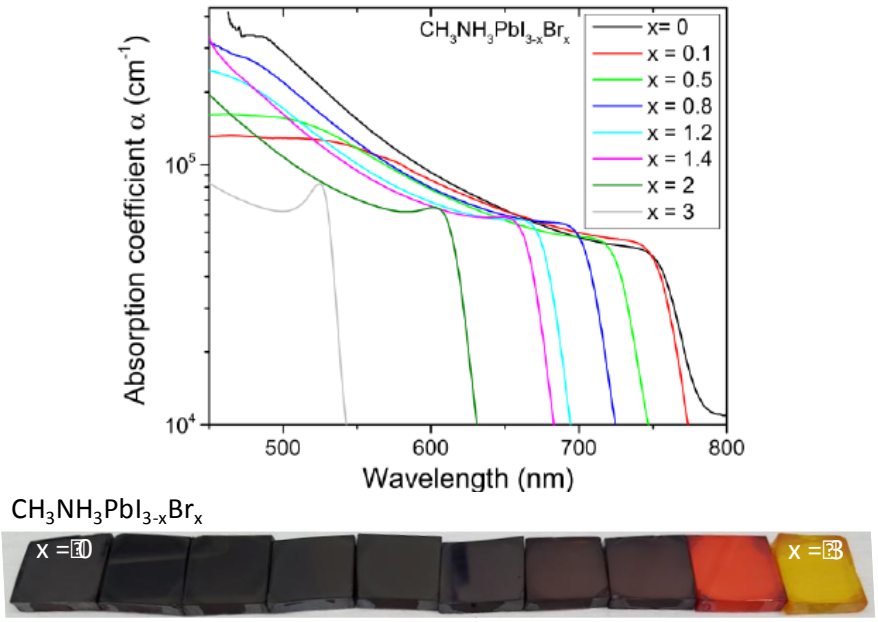

Figure 1.19: On top the absorption coefficient of $CH_3NH_3PbI_{3-x}Br_x$ samples extracted from transmittance and diffuse reflectance measurements. On the bottom the colorful samples with increasing Br-content.[30]

In the same way it is possible to have mixed Cl/Br perovskite as alloys, while the Cl/I mixed perovskite does not exist due to the large dimension difference between the two anions: the size mismatch of the lattices is so big to destabilize the whole system.

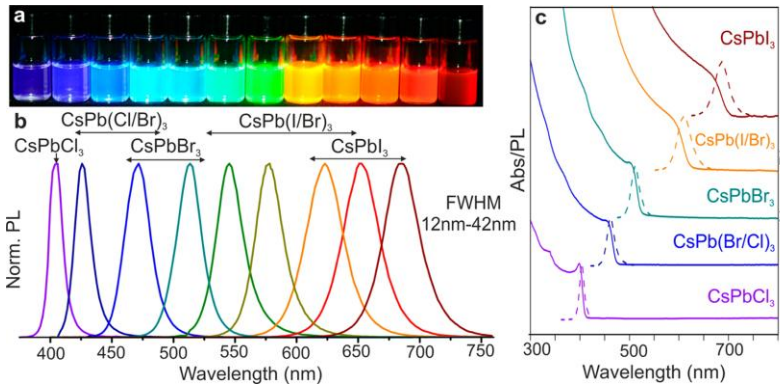

Figure 1.20: Absorbance and photoluminescence of $CsPbX_3$ (X = Cl, Br, and I) nanocrystals.

Also the A-site may have different species leading to new compounds as for example the cesium lead iodide ($CsPbI_3$) and the formamidinium lead iodide

($(NH_2)_2CHPbI_3$, $FAPbI_3$). In particular $CsPbI_3$ semiconductor is subjected to the halide substitution in the same way of $MAPbI_3$: in the **Figure 1.20** it is possible to observe the photoluminescence and the absorbance of the $CsPb(I_{(1-x)}Br_x)_3$ and $CsPb(Br_{(1-x)}Cl_x)_3$ nanocrystals going from 400 to 700 nm.

Another organic cation (formamidinium, FA^+) was used to replace the Cs element or the MA^+: in this case the band gap of the resulting $FAPbI_3$ is slightly reduced to 1.48 eV compared to $MAPbI_3$. At the same time the material showed higher photo-stability and lower moisture-stability (perovskite black phase turns in non-perovskite yellow phase) than $MAPbI_3$. If the FA cation is partially substituted with the MA cation, the stability of the black phase is increased at the expense of the photo-stability. In $FAPbX_3$ it is also possible to change the halide composition/ratio to tune the band gap (from 1.48 eV) and the same is possible obtain in the partial substitution at multiple lattice sites as for the $FA_{0.83}Cs_{0.17}Pb(I_{(1-x)}Br_x)_3$ (**Figure 1.21**).

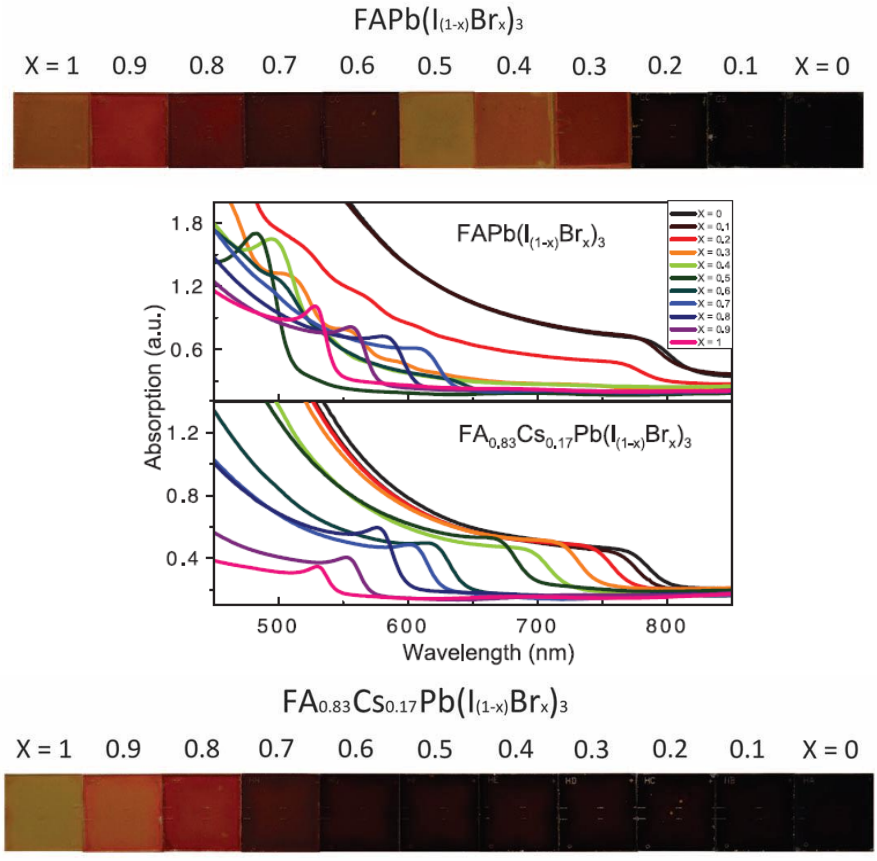

Figure 1.21: Absorption spectra of $FAPb(I_{1-x}Br_x)_3$and $(FA_{0.83}Cs_{0.17}Pb(I_{(1-x)}Br_x)_3$.

During the optimization of the p-SCs the researchers turned their attention on some weak points characterizing this devices as for example the poor stability the to the

moisture (oxygen and humidity), the lead toxicity and the degradation by light (photo-segregation).

One of the most urgent problem appeared in the mixed $MAPb(I_{1-x}Br_x)_3$ used for the tandem Silicon/p-SC is the photo-induced segregation: it consists in the formation of domains rich in one of the two halides. This phenomenon is particularly pronounced in $AB(I_{1-x}Br_x)_3$ systems with $0.5 \leq X \leq 1$ but the use of mixed cation for the A-site proved to limit the photo-instability. Trying to solve this problem, Snaith et al. deposited a layer of $[HC(NH_2)_2]_{0.83}Cs_{0.17}Pb(I_{0.6}Br_{0.4})_3$ which showed improved thermal and photo-stability with a band gap of 1.74 eV suitable for Silicon/p-SC.[31]

As for the halide part and the A-site, it was demonstrated the possibility to substitute the metal ion (Pb^{2+}) with other elements. For instance tin is used to fabricate lead-free devices, limiting the environmental concern due to the lead toxicity. Unfortunately the tin-based solar cell shows poor efficiencies in the range of 2% and 6% and low stability: the rapid degradation of the photoactive layer is attributed to the oxidation of Sn^{2+} in Sn^{4+}.[28,32]

1.5.4. Ion Transport

The first hypothesis of the existence ionic transport raised when an anomalous current-voltage behavior of the perovskite-based solar cell, namely hysteresis, was noticed. Spectroscopic impedance studies proved that the halide perovskite shows both electronic conduction as well as ionic transport. The latter phenomenon is caused by the presence of interstitial defects in the bulk material as vacancies, leading to a vacancy-assisted process or the ionic migration. This effect is particularly evident under short-circuit conditions, and consists in the migration of ionic charges across the photoactive material and their accumulation at the interfaces with the transporting materials. The ionic charges at the interfaces decrease the internal field making the photo-generated charge carrier extraction less efficient. Moreover the ion migration seems to lead to degradation pathways due to their possible leakage across the interfaces.[33]

The mitigation of the ion transport in this material is deeply studied: the ion migration occurs mostly at the grain boundaries and only partially in the bulk of the material. It has been demonstrated that fullerene passivates the charge traps at the

interface with the halide perovskite, thereby determining the suppression of the hysteresis. Yongbo Yuan and Jinsong Huang[34] suggests that fullerene interacts with the grain boundaries and blocks the preferential channel for the ion migration, thus decreasing its effect. Finally it has been suggested that another approach to reduce ion migration is to improve of the crystallinity of the layer in order to decrease the density of the grain boundaries.

1.6. Solar Cell Device

This section describes the so called "Golden Triangle", a concept summarizing the properties that should characterize the final device and the PV technology in general. Moreover several possible architectures are available for a p-SC and they are briefly described in order to give a more complete overview on the existing structures.

1.6.1. The "Golden Triangle"

Beside the excellent photo-physical properties, the p-SC became very attracting due to some more practical characteristic. To be commercialized, a PV device needs to fill the three requirements forming the so called "Golden Triangle": high efficiency, low cost and

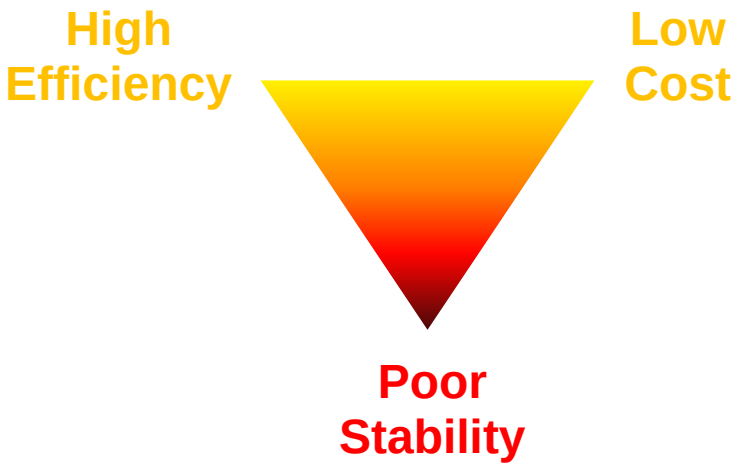

Figure 1.22: The "Golden Triangle" for the p-SC technology

good stability.

In the previous chapter the main physical-chemical properties are described in order to show the perovskite features leading to the high efficient solar cells (22.1%).

Although high efficiency is a must for a SC, it is important that the PV technology reaches a competitive price in terms of electricity cost and in payback terms. One of the limiting factor of the high efficient mono-Si SC is the high production cost: in particular this technology exploits expensive first materials and demanding steps from the manufacturing point of view. At the contrary, the strength points of the p-SC are the low cost of the chemicals and the easiness required for the fabrication of the device.

Unfortunately the researchers found some weak points as the low stability in air due to the moisture (water and oxygen) and the photo-segregation phenomena of the mixed halide perovskite (affecting the tandem technology).

1.6.2. Architectures of a p-SC

Several stacked thin layers form a p-SC and each of them has a precise role inside the overall structure. In general this kind of technology is based on a p-i-n junction where the intrinsic (i-type) material is sandwiched between the p- and n-type semiconductors. In the outermost and opposite regions of the stack there are the electrodes necessary for the collection of the carriers (**Figure 1.23**).

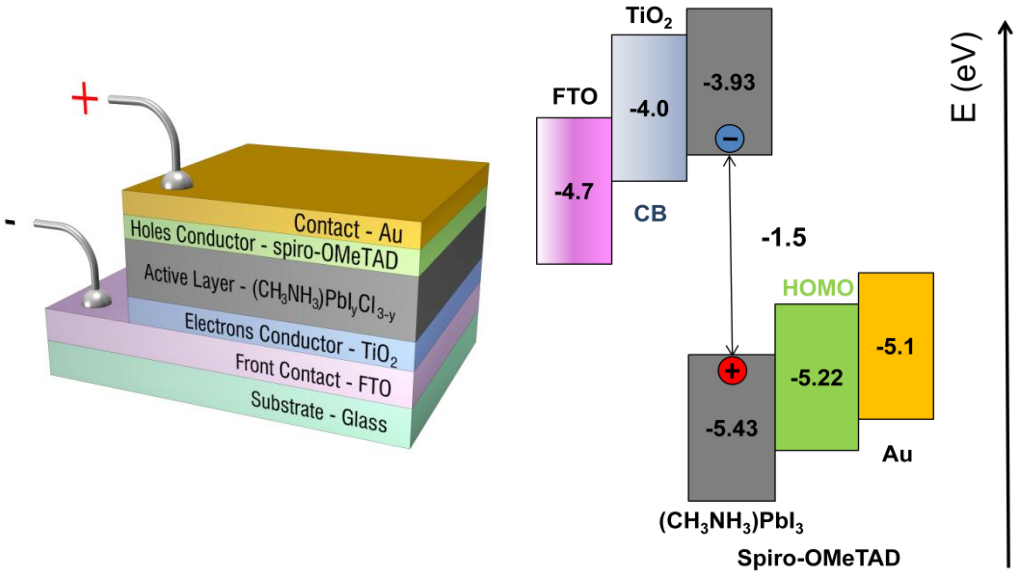

Figure 1.23: On the left scheme of p-SC (Rhyno 4.0) and on the right the energy levels and band gap (eV) of the semiconducting materials.

The n-type semiconductor (usually TiO_2) acts both as electron transporting material (ETM) and hole blocking layer (HBL), while with opposite tasks the organic p-type

$N^2,N^2,N^{2'},N^{2'},N^7,N^7,N^{7'},N^{7'}$-octakis(4-methoxyphenyl)-9,9'-spirobi[9H-fluorene]-2,2',7,7'-tetramine (Spiro-OMeTAD) is present as hole transporting material (HTM) and electron blocking layer (EBL): he role of the materials depends on the band alignment between the perovskite layer and the ETM or the HTM. The photoactive material, as for example $CH_3NH_3PbI_3$, is an intrinsic semiconductor since besides the excellent absorption properties it showed good transport capability for both the electrons and the holes. Once photon is absorbed the electron in the CB it is allowed to hop into the CB of the TiO_2 layer; in the same way the hole generated from the electron excitation exploits the suitable band alignment with the highest occupied molecular orbital (HOMO) of the Spiro-OMeTAD to pass through the layer and reach the gold electrode.

To give an overview as complete as possible it is important to report the possibility to fabricate p-SC based on different architectures as reported in the following scheme (**Figure 1.24**). The possible configurations may be divided in two groups: the meso-structured p-SC (**Figure 1.24a-d**) and the planar p-SC (**Figure 1.24b-c**).

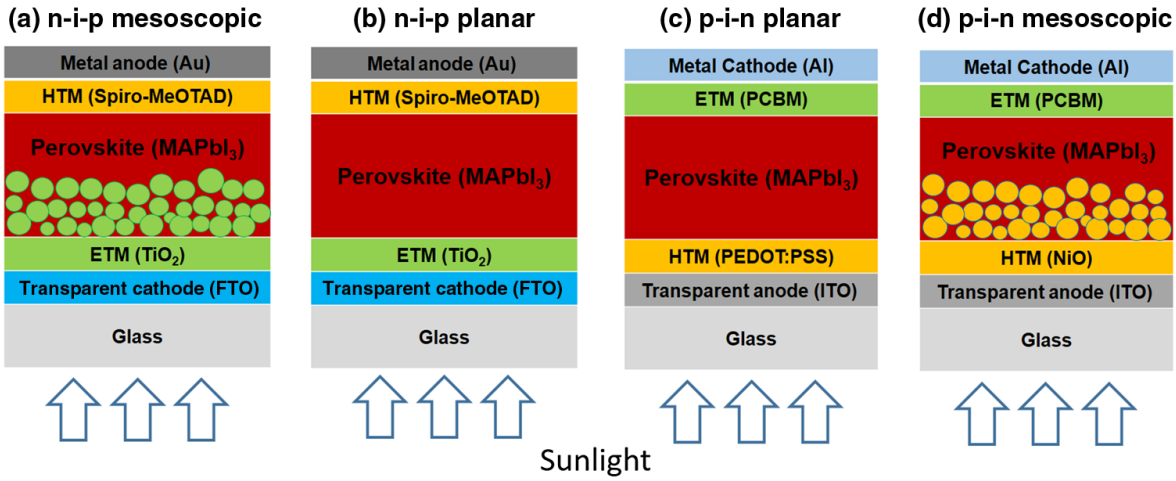

Figure 1.24: Diagram of the structure of (a-d) the meso-structured p-SC and (b-c) the planar p-SC.[35]

The main difference between these two kind of SCs is the use of a meso-porous scaffold of the same type of the HTM or ETM layer. The first fabricated cells exploited the porous substrate since they were evolving from the DSSC but after the discovery of the excellent carrier features of the organo-lead halide perovskite, also the planar devices resulted interesting, especially for the simplicity of the fabrication.

The devices may be also classified depending on the "junction directionality": in the common n-i-p devices the ETM (compact TiO_2, c-TiO_2) is in contact with the

transparent electrode while in the p-i-n structure the HTM is stacked onto the transparent electrode and the ETM is on the other side of the halide perovskite film.

It is important to keep in mind that the light has to reach the photoactive semiconductor: to do this it has to pass through all the layers (glass, electrode and HTM or ETM) between the source and the halide perovskite. To minimize the energy losses these materials need to be transparent: the electrode deposited onto the glass substrate is usually ITO (Indium tin oxide) or FTO (Fluorine doped tin oxide) and the same no absorption property in the visible range has to characterize both the HTM either ETM. In the n-i-p configuration the most used transparent n-type materials are TiO_2 or ZnO while in the p-i-n structure the transparent p-type HTM usually are PEDOT:PSS or NiO.

The devices fabricated during this project have a n-i-p architecture and the main materials are FTO (transparent electrode), c-TiO_2 (ETM), $CH_3NH_3PbI_3$, Spiro-OMeTAD (HTM) and gold as counter electrode. The graph below reported (**Figure 1.25**) summarizes some of the most used materials for the fabrication of the SC with their band alignment: it is possible to notice the huge amount of the possible combinations.

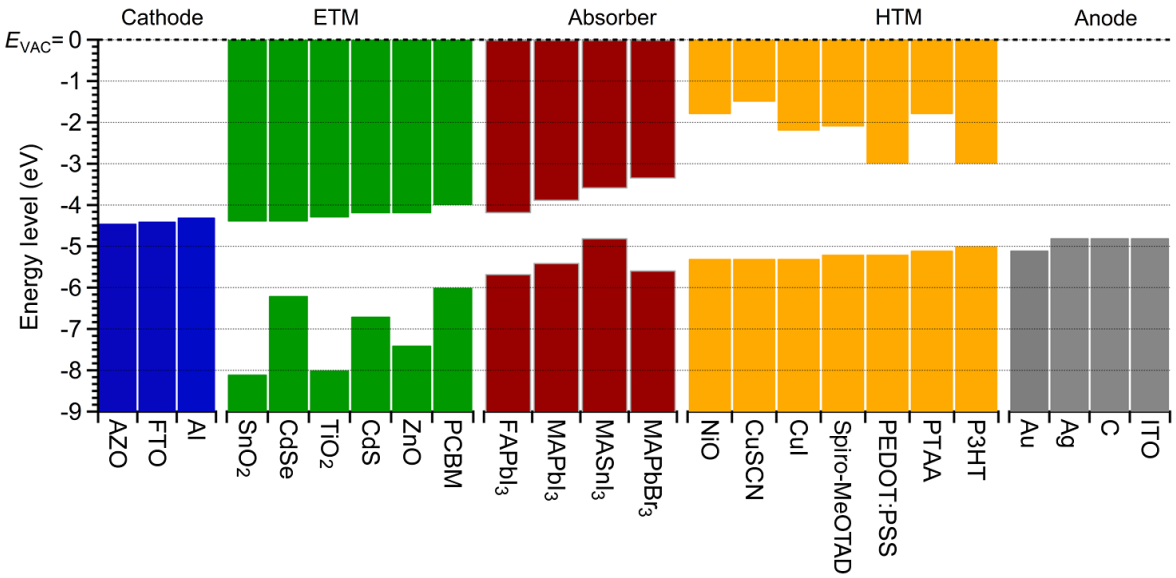

Figure 1.25:Diagram showing the energy levels, from left to right, for representative cathode, n-type (ETM), absorber, p-type (HTM), and anode materials.[35]

1.7. Deposition Techniques

In this section of the chapter are described the main methods used to deposit/grow/synthesize the organo-lead halide perovskite semiconductor.

1.7.1. Perovskite Synthesis and Deposition

This sub-section summarize some methods used to deposit the photoactive material. Before starting with the description of the different approaches it is important to highlight what raised up in the last years: the morphology and the properties of final material are highly dependent on the chemicals, the deposition techniques and the eventual treatments. It is also interesting to point out the fact that the same layers obtained in different laboratories don't show always the same characteristics: this is a proof of the critical issue of the deposition step and brings in some cases the a problem of reproducibility.

High-quality perovskite films with appropriate morphology, uniformity, phase purity, and crystallinity are essential for high-performance PV devices: in particular the researches attention is focused on the crystallization step responsible for high quality thin films. The preparation processes can be divided in four categories as listed: *single-step solution deposition*, *two-step solution deposition*, *two-step vapor-assisted deposition*, and *thermal vapor deposition*. In **Figure 1.26** the scheme reports the cited methods and some slightly different variations.

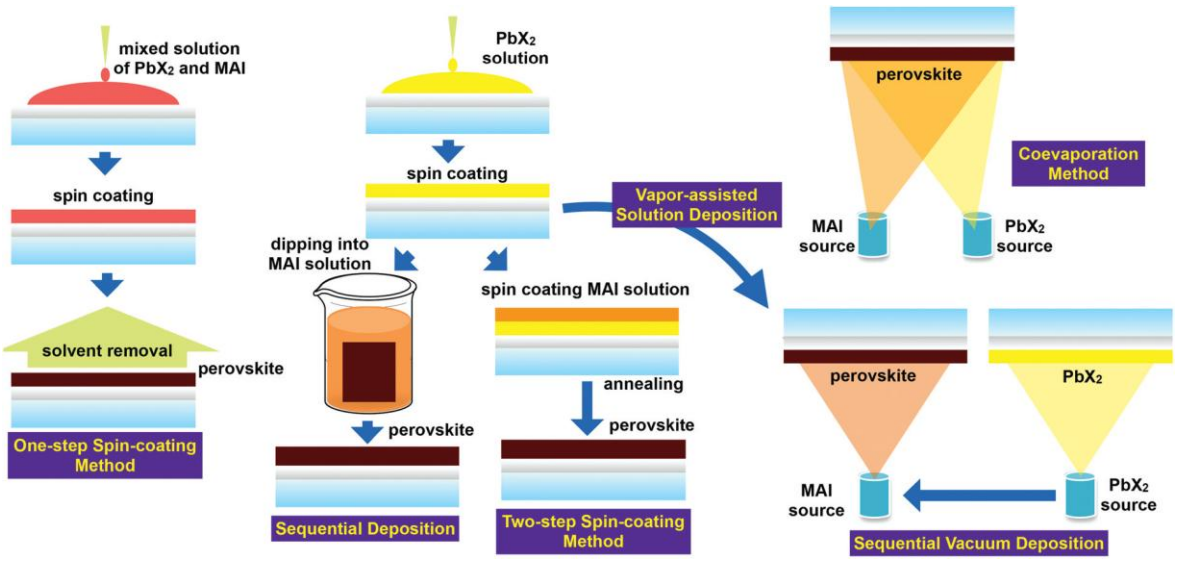

Figure 1.26: Schematic illustration of the diverse methods to obtain perovskite solar cells.[21]

1.7.2. Single-step Solution Deposition

The first photoactive layers were obtained through the spin coating of a halide perovskite solution followed by an annealing step necessary to remove the solvent and to convert the material in a polycrystalline perovskite film. The solution consists in the dissolution of a lead halide salt (PbX_2) and an organic methylammonium halide compound (MAX) in a polar aprotic solvent (DMF, DMSO and/or γ-butirrolactone). The final layer is dependent on a huge amount of parameters as for example the solution concentration, the PbX_2/MAX ratio, the chemical-physical properties of the solvent (boiling point), the possibility to use mixed components and so on. Also the subsequent annealing step is important and many parameters might be varied (temperature, time, use of heating ramps, annealing in solvent atmosphere,..). The best efficiency ever reported for a SC obtained with this method is 19.7%.[36]

1.7.3. Two-step Solution Deposition

Instead of spin coat a solution containing all the compounds, it is possible first to spin coat a precursor solution containing only PbX_2 then convert the so obtained layer into the perovskite material in two different ways: the first consists in the dipping of the substrate into MAX/IPA solution (*sequential deposition*) while the second is the spin coating of the MAX/IPA solution onto the PbX_2 layer (*two-step spin-coating method*). The conversion step is possible because the PbX_2 film is insoluble in IPA solvent.

The sequential deposition was mainly used to obtain perovskite layer in meso-structured SC since the thickness required is lower. This method is also used for planar layers but at the beginning a conversion issues was affecting the step: in particular when the PbI_2 layer is dipped into the solution, a first halide perovskite capping layer forms immediately at the solid-liquid interface. This dense film slows down the MAI diffusion to the underlying layer, leading to incomplete halide perovskite conversion. Optimizing the dipping step this method allows to reach high quality layers characterized by good uniformity and grain size control. With this technique the best devices reports an efficiency of 20.2%.[37]

1.7.4. Two-step Vapor-assisted Deposition

This method exploit the spin coating of the PbI_2 precursor solution as in the case of the two step solution deposition followed by the conversion step with MAI in gas phase. As in the dipping step the MAI diffuse into the PbI_2 layer at the gas-solid interface. The methods allows to obtain uniform films and avoid the delamination issue affecting the liquid-solid interface in the sequential deposition. The first cells showed efficiencies between 10% and 12%,[38,39] while an optimized version of this approach called *Low Pressure Vapor Assisted Solution Process* (LP-VASP) allows to obtain high efficient SC with best device showing 19% PCE.[40] The LP-VASP technique will be further described in Chapter 2.

1.7.5. Thermal Vapor Deposition

In this deposition technique both of the chemicals (PbI_2 and MAI) are transformed from the solid phase to the vapor or gas phase. First trials were done with the thermal evaporation of the $PbI_2$and the MAI, with the two steps performed one following the other or at the same time with a dual-source setup (PCE 15%).[41] It is also possible to obtain the layer via chemical vapor deposition or growing the film layer-by-layer due with the chemicals sublimated in vacuum.

Despite the good morphologies obtained, the vacuum setup increases the fabrication costs and the process control is still critical due to the low thermal stability of the products.

1.8. Efficiency Characterization

Although this Ph.D. project was not particularly focused on the improvement of the record efficiency of the devices, the fabrication of the SCs resulted as an important part of the work due to the possibility to understand the critical features of the material and also to have a more complete view on the perovskite topic.

Besides the classical techniques used to characterize each layer as for example XRD, Uv-vis spectroscopy, SEM, XPS, UPS, AFM and so on, it is possible to evaluate the efficiency of the device. The SC efficiency (η) also called photon-to-current conversion

efficiency (*PCE*) defines the device capability to convert the sun energy into electrical energy.

In general the efficiency is defined as the ratio of the power output from the SC to the power input from the sun, as described with the following equation (**2.1**):

$$\eta = \frac{P_{out}}{P_{in}} \qquad (\mathbf{2.1})$$

The P_{in} (or sun power, P_{sun}) is maintained constant during the measurement and the value is standardized in order to have defined and universal conditions:

- Air mass 1.5 spectrum (AM1.5) for terrestrial cells;
- Intensity of 100 mW/cm^2 (1 kW/m^2, one-sun of illumination);
- Cell temperature of 25 °C (not 300 K).

The power output (P_{out}) is defined as the product of the voltage (V) output and current (I) output (expressed also as current density J to eliminate the variation of the active area of the device), so no power is generated under short or open circuit conditions:

$$P_{out} = V_{out} \times J_{out} \qquad (\mathbf{2.2})$$

In general the maximum power (P_{max}) is generated when the product of the aforementioned parameters (voltage and current density) is maximum, as describe in the equation (**2.3)** and represented in the **Figure 1.27**.

$$P_{max} = V_{max} \times J_{max} \qquad (\mathbf{2.3})$$

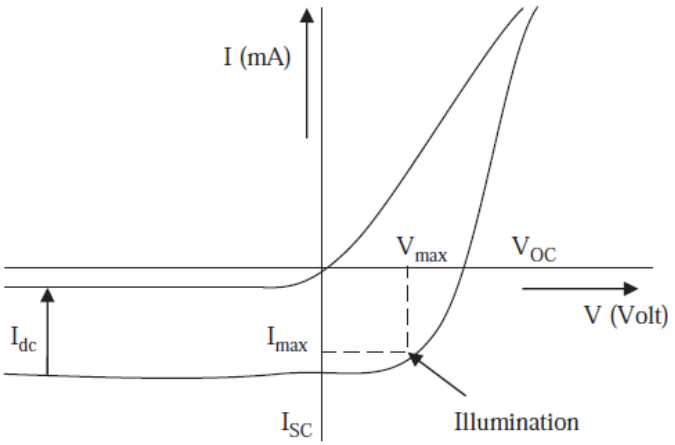

Figure 1.27: Characteristic curve IV to determine the parameters to calculate η.

The maximum power is also defined as the product of the current generated in short circuit condition (J_{SC}), the voltage in open circuit conditions (V_{oc}) and the fill factor (*FF*):

$$P_{max} = V_{oc} \times J_{sc} \times FF \quad \textbf{(2.4)}$$

The fill factor is defined as the ration between the maximum output power to the product of the J_{SC} times the V_{OC} and is represents the ratio of the small rectangle to the big one (**Figure 1.28**):

$$FF = \frac{V_{max} \times J_{max}}{V_{oc} \times J_{sc}} \quad \textbf{(2.5)}$$

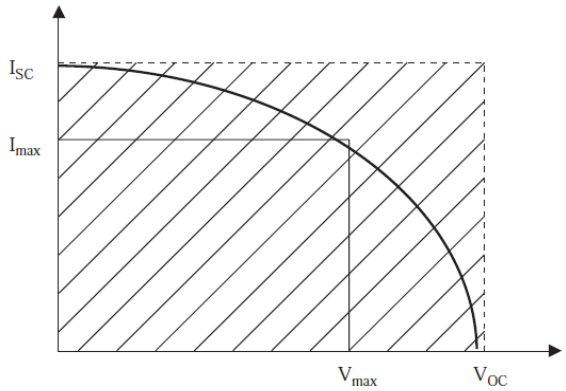

Figure 1.28: Characteristic curve for determining the fill factor.

It indicates the quality of the junction in the cell and gives an indication on the parasitic resistances: for high parasitic resistance the FF tends to be low and vice versa. In general when the open circuit voltage is high also the fill factor assumes high values. Even if the fill factor maximum is 1, the higher theoretical value is always lower than 1 and is dependent on the band gap of the semiconductor as described in the following graph (**Figure 1.29**):

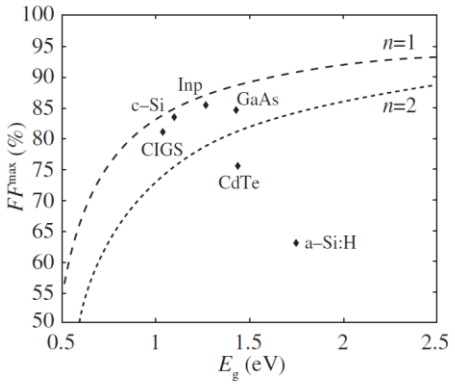

Figure 1.29: Theoretical limit values and experimentally obtained values as function of the bandgap energy E_g for FF.

To calculate the efficiency it is possible to rewrite the equation (**2.1)** using the equation (**2.4)** and obtaining the following formula (**2.5**):

$$\eta = \frac{V_{oc} \times I_{sc} \times FF}{P_{in}} \qquad (2.5)$$

All the parameters at the numerator (V_{OC}, I_{SC} and FF) are extracted from the *JV* curve while the P_{in} is equal to 1 sun (100 mW/cm^2) as required by the standard conditions: the current setups give all the data already processed.

In general a SC is described as an electric circuit by the following equation (**2.6**) and represented in **Figure 1.30**:

$$J = J_{light} - J_0 \left[exp\left(\frac{q(V+JR_s)}{nkT}\right)\right] - \frac{V+JR_S}{R_{SH}} \qquad (2.6)$$

where J_{light} is the photo-generated current density while the second and third terms describe the diode behavior in dark conditions and taking in account the parasitic resistances.

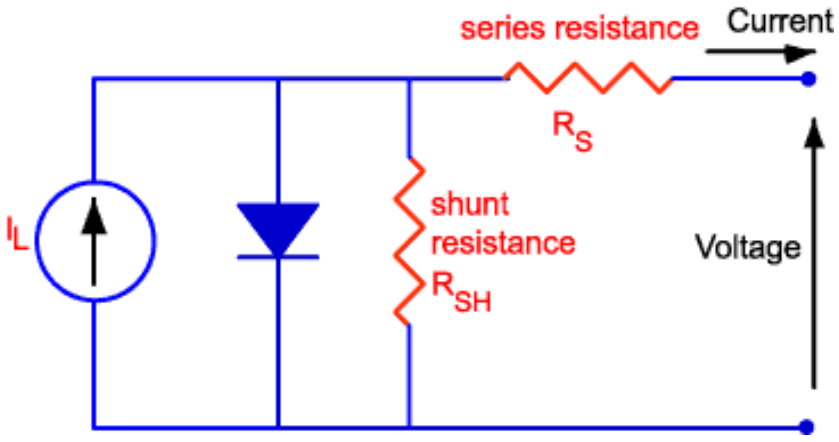

Figure 1.30: Electric circuit of a SC

In **Figure 1.30** all the elements affecting the electric circuit are reported: the current generated under light exposure (I_L or J_{light}), the diode (p-i-n junction) and two types of the parasitic resistances. For an optimal device it is supposed to have a high shunt resistance (R_{SH}) and a low series resistance (R_S) to have the electron flow through the circuit connected to the external load.

The shunt resistance is usually low due to manufacturing defects (defected regions), rather than poor solar cell design. Low shunt resistance causes power losses in

the solar cells since part of the flowing current does not pass through the external load. It is caused by increased recombination due to the presence of some alternate paths for the photo-generated current. Low R_{SH} reduces the overall voltage and partially the fill factor.

The series resistance on the other hand are usually high in the devices with bad metallic contacts and if the quality at the layer interfaces is poor. The R_S has no effect on the open-circuit voltage, but reduces the short-circuit current and again may affect the FF.

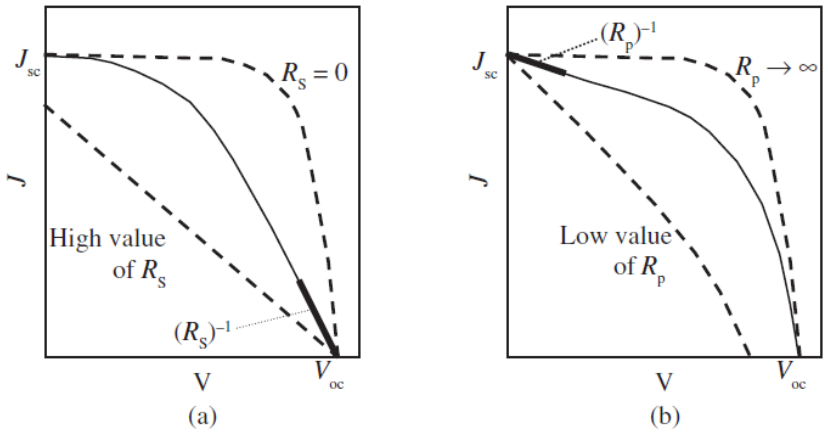

Figure 1.31: Effects of series and shunt resistances on J(V)

As reported in **Figure 1.31**,it is possible to appreciate the repercussions of the two resistances on the shape of the J(V) curve. When a SC is measured it is possible to extract data that quantify the contribution of both the resistances.

1.8.1. J-V Hysteresis

The hysteresis is the phenomenon affecting the current-voltage characteristic of a solar cell: in particular several parameters, such as the scan direction (forward or reverse), the scan rate, the bias treatment before the PCE measurement and the device configuration the device performance, affect the device performance. The anomalous J-V behavior is then a problem for determining the accurate efficiency of the device.

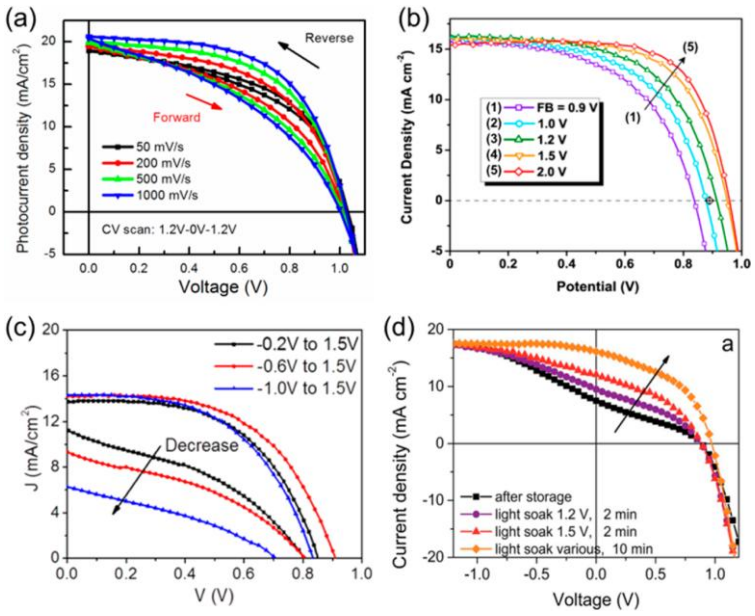

1.32: Dependence of the J–V hysteresis behavior on (a) scan rate, (b) positive starting bias under reverse scan, (c) negative starting bias under forward scan, and (d) light-soaking preconditions.[42]

Despite the high interest and the importance of the topic, there is still no a clear explanation about the origin of the hysteresis. Many possible mechanisms and events are under investigation but none of them alone justifies the presence of this anomalous behavior. Amongst them the most probable root causes are listed below:

- ion transport: responsible of the induced adjustment of electric field distribution due to the band banding that can influence the separation and collection of photo-generated charges;
- charge traps: mostly present at the interfaces and at the grain boundaries, when reduced (after the passivation of the halide perovskite layer) the charge extraction is higher and the hysteresis behavior is minimized.

It is reported that the hysteresis is reduced with a thin porous TiO_2 layer probably because a higher surface area enhance the charge extraction filling the electronic traps at the interface and limiting the ionic accumulation. On the same strategy is based the use of the p-i-n structure, where the organic n-type fullerene passivates the trap states at the interface.[43]

1.9. References

1. BP Statistical Review of World Energy. *Workbook* 1–48 (2016).
2. Chen, G. Q. & Wu, X. F. Energy overview for globalized world economy: Source, supply chain and sink. *Renew. Sustain. Energy Rev.* **69,** 735–749 (2017).
3. Agency, I. E. Key world energy statistics 2016. (2016).
4. Needleman, D. B. *et al.* Economically Sustainable Scaling of Photovoltaics to Meet Climate Targets. *Energy Environ. Sci.* **9,** 2122–2129 (2016).
5. Branker, K. & Pearce, J. M. A Review of Solar Photovoltaic Levelized Cost of Electricity. *Renew. Sustain. Energy Rev.* **15,** 4470–4482 (2011).
6. Hegedus, S. S. & Luque, A. *Handbook of Photovoltaic Science and Engineering*. *Handbook of Photovoltaic Science and Engineering* **1,** (2003).
7. Blandford, R. & Watkins, M. This Month in Physics History: April 25, 1954: Bell Labs Demonstrates the First Practical Silicon Solar Cell. *APS News* **18,** 2 (2009).
8. Easton, R. L. & Votaw, M. J. Vanguard I IGY Satellite (1958 Beta). *Rev. Sci. Instrum.* **30,** 70–75 (1959).
9. Warmuth, W. & Philipps, S. Photovoltaics report. *Fraunhofer Institute for Solar Energy Systems, ISE* (2016).
10. Best Research-Cell Efficiencies. *National Renewable Energy Laboratory* (2017). Available at: http://www.nrel.gov/pv/assets/images/efficiency_chart.jpg.
11. Peng, J., Lu, L. & Yang, H. Review on life cycle assessment of energy payback and greenhouse gas emission of solar photovoltaic systems. *Renew. Sustain. Energy Rev.* **19,** 255–274 (2013).
12. Werner, J. H., Zapf-gottwick, R., Koch, M. & Fischer, K. Toxix Substances in photovoltaic Modules. in *The 21st International Photovoltaic Science and Engineering Conference* 4–5 (2011).
13. Tolcin, A. C. Mineral Commodity Summaries 2016: Indium. *United States Geological Survey* 80–81 (2016). Available at: https://minerals.usgs.gov/minerals/pubs/commodity/indium/mcs-2016-indiu.pdf.
14. Ye, M. *et al.* Recent advances in dye-sensitized solar cells: From photoanodes, sensitizers and electrolytes to counter electrodes. *Mater. Today* **18,** 155–162

(2015).

15. Snaith, H. J. Perovskites: The Emergence of a New Era for Low-Cost, High-Efficiency Solar Cells. *J. Phys. Chem. Lett.* **4,** 2623–2630 (2013).
16. Kojima, A., Teshima, K., Shirai, Y. & Miyasaka, T. Organometal halide perovskites as visible-light sensitizers for photovoltaic cells. *J. Am. Chem. Soc.* **131,** 6050–1 (2009).
17. Im, J.-H., Lee, C.-R., Lee, J.-W., Park, S.-W. & Park, N.-G. 6.5% Efficient Perovskite Quantum-Dot-Sensitized Solar Cell. *Nanoscale* **3,** 4088–93 (2011).
18. Kim, H.-S. *et al.* Lead iodide perovskite sensitized all-solid-state submicron thin film mesoscopic solar cell with efficiency exceeding 9%. *Sci. Rep.* **2,** 591 (2012).
19. Lee, M. M., Teuscher, J., Miyasaka, T., Murakami, T. N. & Snaith, H. J. Efficient hybrid solar cells based on meso-superstructured organometal halide perovskites. *Science* **338,** 643–7 (2012).
20. Burschka, J. *et al.* Tris(2-(1H-pyrazol-1-yl)pyridine)cobalt(III) as p-type dopant for organic semiconductors and its application in highly efficient solid-state dye-sensitized solar cells. *J. Am. Chem. Soc.* **133,** 18042–5 (2011).
21. Zheng, L. *et al.* Morphology control of the perovskite films for efficient solar cells. *Dalt. Trans.* **44,** 10582–10593 (2015).
22. Tan, Z.-K. *et al.* Bright light-emitting diodes based on organometal halide perovskite. *Nat. Nanotechnol.* **9,** 1–6 (2014).
23. Fan, J., Jia, B. & Gu, M. Perovskite-based low-cost and high-efficiency hybrid halide solar cells. *Photonics Res.* **2,** 111 (2014).
24. Onoda-Yamamuro, N., Yamamuro, O., Matsuo, T. & Suga, H. p-T phase relations of CH3NH3PbX3 (X = Cl, Br, I) crystals. *J. Phys. Chem. Solids* **53,** 277–281 (1992).
25. Sun, S. *et al.* The origin of high efficiency in low-temperature solution-processable bilayer organometal halide hybrid solar cells. *Energy Environ. Sci.* **7,** 399 (2014).
26. Manser, J. S., Christians, J. A. & Kamat, P. V. Intriguing Optoelectronic Properties of Metal Halide Perovskites. (2016). doi:10.1021/acs.chemrev.6b00136
27. Umebayashi, T., Asai, K., Kondo, T. & Nakao, A. Electronic structures of lead iodide based low-dimensional crystals. *Phys. Rev. B* **67,** 155405 (2003).
28. Park, N.-G., Grätzel, M. & Miyasaka, T. *Organic-Inorganic Halide Perovskite Photovoltaics*. *Organic-Inorganic Halide Perovskite Photovoltaics* (2016). doi:10.1007/978-3-319-35114-8_4

29. Sutter-Fella, C. M. *et al.* High Photoluminescence Quantum Yield in Band Gap Tunable Bromide Containing Mixed Halide Perovskites. *Nano Lett.* **16,** 800–806 (2016).
30. Peters, I. M., Sofia, S., Mailoa, J. & Buonassisi, T. Techno-economic analysis of tandem photovoltaic systems. *RSC Adv.* **6,** 66911–66923 (2016).
31. McMeekin, D. P. *et al.* A mixed-cation lead mixed-halide perovskite absorber for tandem solar cells. *Science (80-.).* **351,** 151–155 (2016).
32. Lee, S. J. *et al.* Fabrication of Efficient Formamidinium Tin Iodide Perovskite Solar Cells through SnF2-Pyrazine Complex. *J. Am. Chem. Soc.* **138,** 3974–3977 (2016).
33. Eames, C. *et al.* Ionic transport in hybrid lead iodide perovskite solar cells. *Nat Commun* **6,** 1–8 (2015).
34. Yuan, Y. & Huang, J. Ion Migration in Organometal Trihalide Perovskite and Its Impact on Photovoltaic Efficiency and Stability. *Acc. Chem. Res.* **49,** 286–293 (2016).
35. Song, Z., Watthage, S. C., Phillips, A. B. & Heben, M. J. Pathways toward high-performance perovskite solar cells: review of recent advances in organo-metal halide perovskites for photovoltaic applications. *J. Photonics Energy* **6,** 22001 (2016).
36. Ahn, N. *et al.* Highly Reproducible Perovskite Solar Cells with Average Efficiency of 18.3% and Best Efficiency of 19.7% Fabricated via Lewis Base Adduct of Lead(II) Iodide. *J. Am. Chem. Soc.* **137,** 8696–8699 (2015).
37. Yang, W. S. *et al.* High-performance photovoltaic perovskite layers fabricated through intramolecular exchange. *Science (80-.).* **348,** 1234–1237 (2015).
38. Chen, Q. *et al.* Planar heterojunction perovskite solar cells via vapor-assisted solution process. *J. Am. Chem. Soc.* **136,** 622–625 (2014).
39. Hao, F., Stoumpos, C. C., Liu, Z., Chang, R. P. H. & Kanatzidis, M. G. Controllable Perovskite Crystallization at a Gas–Solid Interface for Hole Conductor-Free Solar Cells with Steady Power Conversion Efficiency over 10%. *J. Am. Chem. Soc.* **136,** 16411–16419 (2014).
40. Li, Y. *et al.* Defective TiO2 with high photoconductive gain for efficient and stable planar heterojunction perovskite solar cells. *Nat. Commun.* **2,** 1–18 (2016).
41. Liu, M., Johnston, M. B. & Snaith, H. J. Efficient planar heterojunction perovskite

solar cells by vapour deposition. *Nature* **501,** 395–8 (2013).

42. Chen, B., Yang, M., Priya, S. & Zhu, K. Origin of J-V Hysteresis in Perovskite Solar Cells. *J. Phys. Chem. Lett.* **7,** 905–917 (2016).

43. Zhang, W., Eperon, G. E. & Snaith, H. J. Metal halide perovskites for energy applications. *Nat. Energy* 16048 (2016). doi:10.1038/nenergy.2016.48

2. Synthesis of $MAPbI_3Br_{3-x}$ Cubic Crystals

This chapter describes the synthesis and characterization of polycrystalline films with well shaped cubic crystals of methylammonium lead iodide $MAPbI_3Br_{3-x}$ perovskite.

2.1. Motivation

The need of controlling the morphology of halide perovskite crystals in active thin films arises from the already demonstrated and widely reported correlation that grain orientation has with the performances of hybrid perovskite photovoltaic cells. In particular, Leblebici et al.[1]report that films with cubic-shaped crystals have electronic transport properties such as photocurrent and photovoltage that depend on the different facets of the same halide perovskite crystal. They show that the aforementioned properties have different values on the different facets of the same grain, suggesting that there is a preferential orientation of the crystal planes and defect concentration for the optimal electronic transport properties.

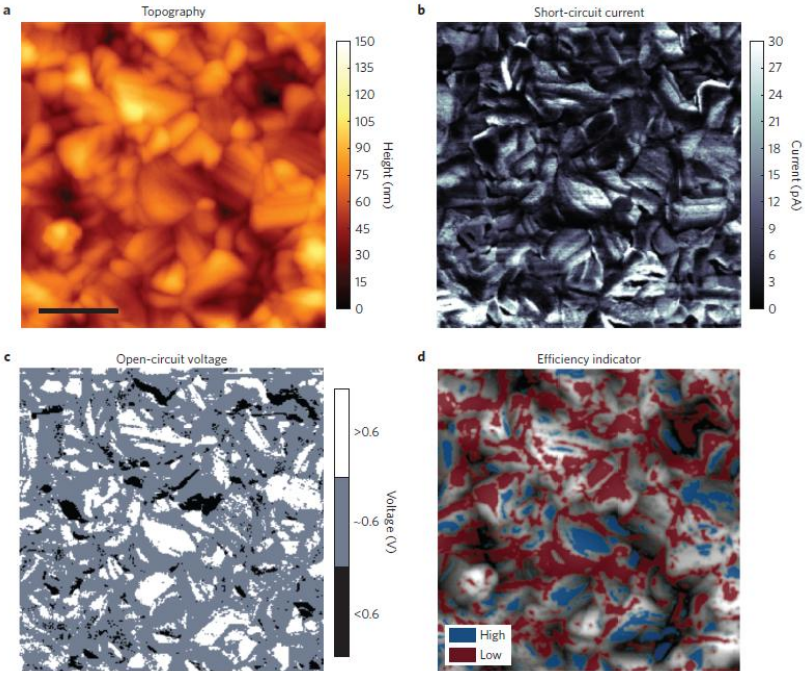

Figure 2.1: a) Topography image of $MAPbI_3Cl_{3-x}$ layer: individual crystal grains and their facets are clearly visible. The scale bar is 500 nm; b) I_{SC} map measured at 0V bias under illumination; c) Segmented V_{OC} map measured under illumination relative to a forward reference bias of 0.6V. Grey areas have V_{OC} close to the reference bias, white areas above and black areas below; d) To compare heterogeneity of I_{SC} and V_{OC} to facets, areas in blue (high V_{OC} and I_{SC}) and areas in red (low V_{OC} and I_{SC}) are overlaid on the local topography, indicating that many grains have a specific crystal facet that provides higher performance.[1]

Thus, the orientation of the crystals is a critical factor that must be considered during the deposition of the photoactive layer in order to obtain high efficiency perovksite based solar cells. By means of photoconductive AFM characterization (**Figure 2.1**), the authors show the heterogeneity of both the photocurrent and the photovoltage on the same grain (**Figure 2.1b** and **2.1c**). In addition, they also image a map (**Figure 2.1d**) with areas contributing with high efficiency (high I_{SC} and high V_{OC}) and with low efficiency (low I_{SC} and low V_{OC}) to transport. The material used by Leblebici and co-workers for the photoconductive AFM characterization is a compact and homogeneous film synthesized by low pressure vapor assisted solution process (LP-VASP), a technique developed at the Lawrence Berkeley National Laboratories (LBNL) by Li at al.[2] This method allows for the fabrication of highly reproducible, efficient planar solar cell devices (16.8% power conversion efficiency). However, *determine the role of local inhomogeneity on electronic properties correlated with specific crystallographic orientations remains an outstanding question in the field*. Specifically, the discovery of intergrain and intragrain heterogeneity in halide perovskite thin films represent a major advance in understanding factors contributing to efficiency loss in perovskite photovoltaics. Finding ways to synthesize organo-lead halide perovskite grains with defined orientation and facets to more precisely correlate local property variations with macroscopic characteristics of devices is an alluring opportunity to further improve the efficiency of this material. In addition, directing crystalline and morphology growth will allow to better understand roles of grain boundaries, local compositional disorder, and fundamental charge separation and transport mechanisms in this materials system.

Thus, with the idea of controlling the morphology of halide perovskite crystals and establishing morphology-optoelectronic relationships, I explored different deposition methods of the perovskite layer. This work would allow for understanding of how varying growth parameters can direct crystalline orientation and crystal shape, and ultimately affect efficiency.

2.2. Morphology Control of Halide Perovskite

In order to achieve the goal mentioned above, I have developed a synthetic process to obtain $MAPbBr_{3-x}I_x$cubic crystals, as shown in the SEM image (**Figure 2.2**). Here the individual grains can be clearly identified and each crystal has both defined and sharp edges with recognizable and flat facets. Then, through a collaboration with Dr. Francesca M. Toma, I have visited Lawrence Berkeley National Laboratory (LBNL), where I have learned the LP-VASP process and combined it with my synthesis technique in order to achieve fine tuning of methylammonium lead halide perovskite compositions and morphological control.

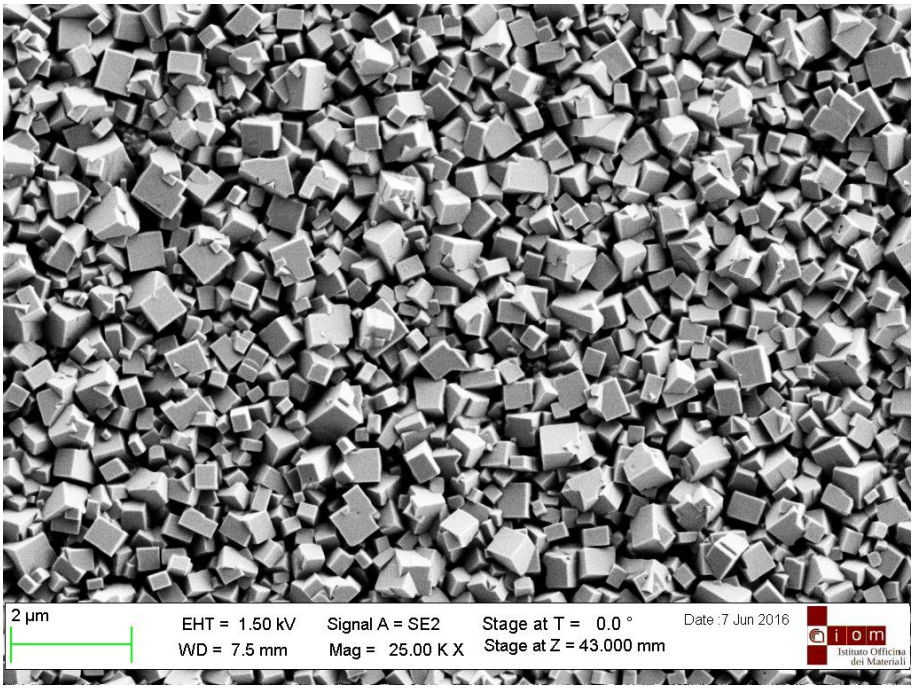

Figure 2.2: $MAPbBr_{3-x}I_x$ cubic crystals deposited at the IOM-CNR in Trieste

In the next paragraphs, I will describe the fabrication process of$MAPbBr_{3-x}I_x$ cubic crystals, LP-VASP, and of the combination of the two processes. Since the halide perovskite material is highly influenced by deposition method and synthetic conditions, as well as the deposition substrate, we have prepared our active layer on a TiO_2 coated fluorine-doped tin oxide (FTO), as this configuration is the same that I have used to fabricate solar cells. Thus, the material was fully characterized by X-Ray Diffraction (XRD), Scanning Electron Microscopy (SEM), UV-Vis spectroscopy, and photoconductive atomic force microscopy (pc-AFM) on these TiO_2/FTO substrates. Only for the photoluminescence (PL) characterizations the sample was bare glass since the FTO film is

responsible for the quenching of the PL signal. Photoconductive AFM and PL measurements will be reported in Chapter 3.

2.2.1. Low Pressure Vapor Assisted Solution Process (LP-VASP)[2–4]

The standardized protocol for LP-VASP has been recently submitted as a manuscript: "Low Pressure Vapor-Assisted Solution Process for Tunable Band Gap Pinhole-free Methylammonium Lead Halide Perovskite Films" YanboLi,* Carolin M. Sutter-Fella,* **Nicola Cefarin**, Aya K. Buckley, Quyhn P. Ngo, Ali Javey, Ian D. Sharp, Francesca M. Toma

Here, I present a protocol for the synthesis of CH_3NH_3I and CH_3NH_3Br precursors and the subsequent formation of pinhole-free, continuous $CH_3NH_3PbI_{3-x}Br_x$ thin films for the application in high efficiency solar cells and other optoelectronic devices.

$CH_3NH_3PbX_3$ films can be fabricated by a variety of synthetic methods,[5] which aim at improving the efficiency of this semiconducting material for energy applications.[6] However, optimization of photovoltaic devices relies on the quality of the halide perovskite active layer, as well as its interfaces with charge selective contacts (i.e. electron and hole transport layers), which facilitate photocarrier collection in these devices. Specifically, continuous, pinhole-free active layers are necessary to minimize shunt resistance, thereby improving device performance.

First, I report the synthesis of methylammonium iodide (CH_3NH_3I) and methylammonium bromide (CH_3NH_3Br) from methylamine and the corresponding halide acid (HI or HBr). Then, it is described the fabrication of pinhole-free, continuous methylammonium-lead iodide perovskite film with the LP-VASP. This process is based on two steps:

i. spin-coating of a homogenous layer of lead halide mixed precursor (PbI_2/$PbBr_2$) onto a substrate, and
ii. conversion of this layer to$CH_3NH_3PbI_{3-x}Br_x$ by exposing the substrate to vapors of CH_3NH_3I at reduced pressure and 120 °C.

Through slow diffusion of the methyl ammonium halide vapor into the lead halide precursor, it is possible to achieve slow and controlled growth of a continuous, pinhole-free perovskite film. Moreover the LP-VASP allows synthetic access to the full halide

composition space in $CH_3NH_3PbI_{3-x}Br_x$ with $0 \leq x \leq 3$ (here not reported). Depending on the composition of the vapor phase ,the band gap can be tuned between 1.6 eV $\leq E_g \leq$ 2.3 eV. In addition, by varying the composition of the halide precursor and of the vapor phase, we can also obtain $CH_3NH_3PbI_{3-x}Cl_x$. Films obtained from the LP-VASP are reproducible, phase pure as confirmed by X-ray diffraction measurements, and show high photoluminescence quantum yield. The process does not require the use of a glovebox.

This process yields a two-fold volume expansion from the starting lead halide precursor layer to the completed organic-inorganic lead halide perovskite. The standard thickness of the perovskite film is about 400 nm. It is possible to vary this thickness between 100-500 nm by changing the speed of the second spin coating step. The presented technique results in films of high optoelectronic quality, which translates to photovoltaic devices with power conversion efficiencies of up to 19% using aAu/spiro-OMeTAD /$CH_3NH_3PbI_{3-x}Br_x$/compact TiO_2/ FTO/glass solar cell architecture.[4]

2.2.1.1. MAI and MABr Synhtesis

The methylammonium halide synthesis consist of the reaction between the methyl amine and the halide acid in alcohol solution (EtOH): in particular to obtain MAI it is necessary to use hydroiodic acid (HI) while for MABr the required acid is the hydrobromic one (HBr). After 2h the reaction is completed,: the solvent is removed and the obtained powder recrystallized from ethanol and diethyl ether. The product is dried in an oven under vacuum, transferred in dark brown vials and stored in nitrogen filled desiccators due to its hygroscopic property.

2.2.1.2. Substrate Preparation

Before the spin coating step is it important that the substrates used during the process are clean. For this reason the samples are treated as following:

- The substrate is immersed in detergent/deionized water solution in ultrasonic bath for 10’ then rinsed with milliQ water;
- Immersed in acetone in ultrasonic bath for 10’;
- Immersed in isopropyl alcohol (IPA) in ultrasonic bath for 10’;
- Dried with N_2 flow.

2.2.1.3. First Step: Precursor Spin-coating

The precursor solution is prepared dissolving PbI_2 and $PbBr_2$ (0.8M and 0.2M) in DMF. The filtered solution is heated at 110°C on a hot plate then spin coated on the sample. After the spin coating the substrate is dried onto the hot plate at 110°C for 15' under N_2 flow (**Figure 2.3**).

Figure 2.3: Spin Coater and Hot Plate for the annealing.

2.2.1.4. Second Step: Vapor-Assisted Conversion

The second step consists in the conversion of the PbX_2 layer into the desired perovskite semiconductor. The setup (**Figure 2.4**) used for this process requires a Schlenk line (**Figure 2.4a**) equipped with a vacuum pump and with Schlenk tubes (**Figure 2.4b**).

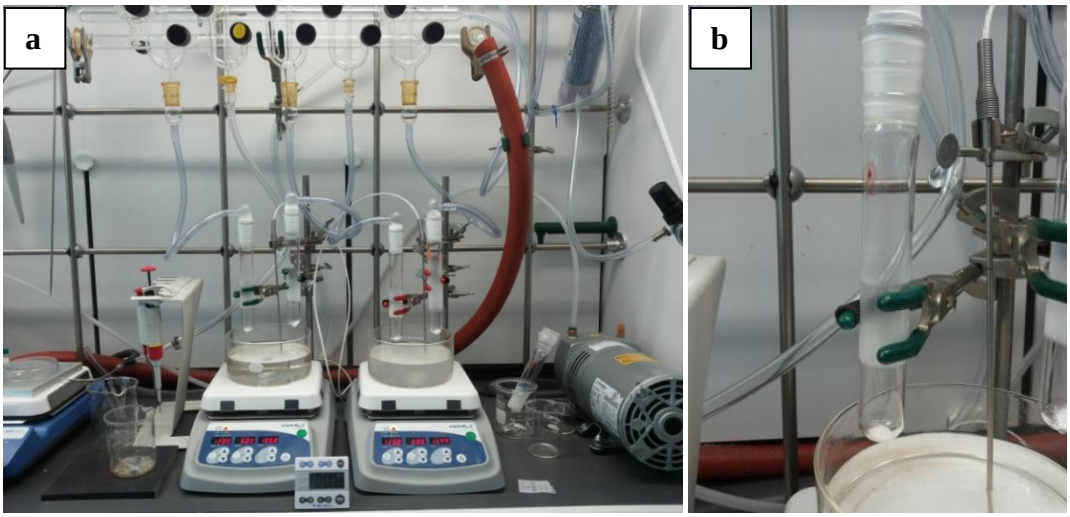

Figure 2.4: (a) Schlenk line setup for the LP-VASP. (b) Schlenk tube with MAX powder on the bottom.

In these tubes (**Figure 2.4b**) the MAX powder is placed on the bottom and the substrate (with the PbX_2 layer faced up) slightly above the MAX precursor powder. The indirect exposure of the PbX_2 layer to the MAX vapor leads to a high film quality due to a lower conversion rate. The tube (**Figure 2.5**) is connected to the vacuum system and in order to reach a reduced pressure (0.185 Torr) then immersed in an oil bath at 120°C and for 2 hours. The lead halide precursor thin film starts converting into the organo-lead halide perovskite material due to the MAX incorporation: at this temperature and pressure the MAX powder sublimates and saturates the atmosphere inside the tube and slowly diffuses in the lead halide film.

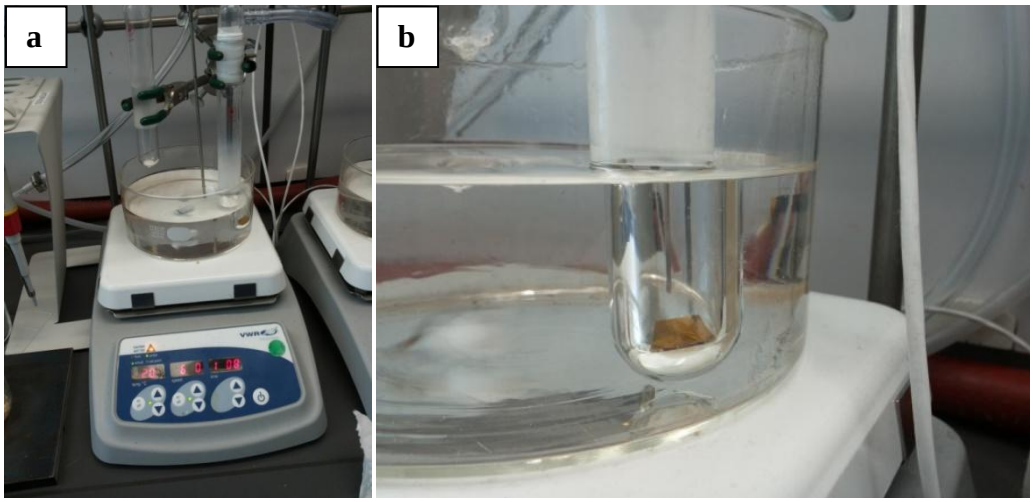

Figure 2.5: (a) shows the Schlenk tube loaded with MAI (powder) and the sample while immersed into the oil bath. (b) magnification of the Schlenk tube during the conversion (yellow-brownish sample).

During the initial part of the process it is clearly possible to notice the color change of the sample. In particular the spin coated precursor before the process is yellow due to $PbI_2/PbBr_2$ layer (**Figure 2.6a**) while during the conversion with MAI its color turns to black($CH_3NH_3PbI_3$) passing through pale brown and dark brown tonalities (**Figure 2.6b**). The same happens for $CH_3NH_3PbBr_3$ (**Figure 2.6c**) when the color changes from yellow to orange touching pale reddish shades.

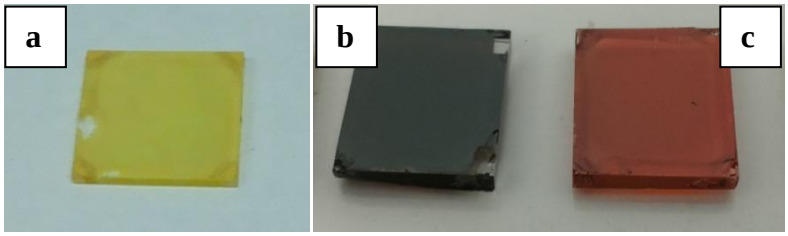

Figure 2.6: a) Spin coaterd PbI_2 on glass, b) $CH_3NH_3PbI_3$ after LP-VASP conversion and c) $CH_3NH_3PbBr_3$ after LP-VASP conversion.

After 2h the sample is carefully removed from the tube, rinsed in isopropyl alcohol (IPA) to wash away the non-reacted MAX forms on the surface and finally dried with the N_2 flow. By using different precursorsPbX_2 (PbI_2/$PbBr_2$/$PbCl_2$) and MAX (CH_3NH_3I and/or CH_3NH_3Br) for the conversion, it is possible to tune the final composition of the perovskite from pure $CH_3NH_3PbI_3$ (through several $CH_3NH_3PbI_{3-X}Br_X$ mixed perovskites) to pure $CH_3NH_3PbBr_3$.

2.2.1.5. Characterization of the LP-VASP Organo-lead Halide Perovskite Layer

Several techniques are used to characterized the final layer. With the Scanning Electron Microscope (SEM) it is possible to image the morphology of the layers before (**Figure 2.7**) and after (**Figure 2.8**) the LP-VASP for a direct comparison.

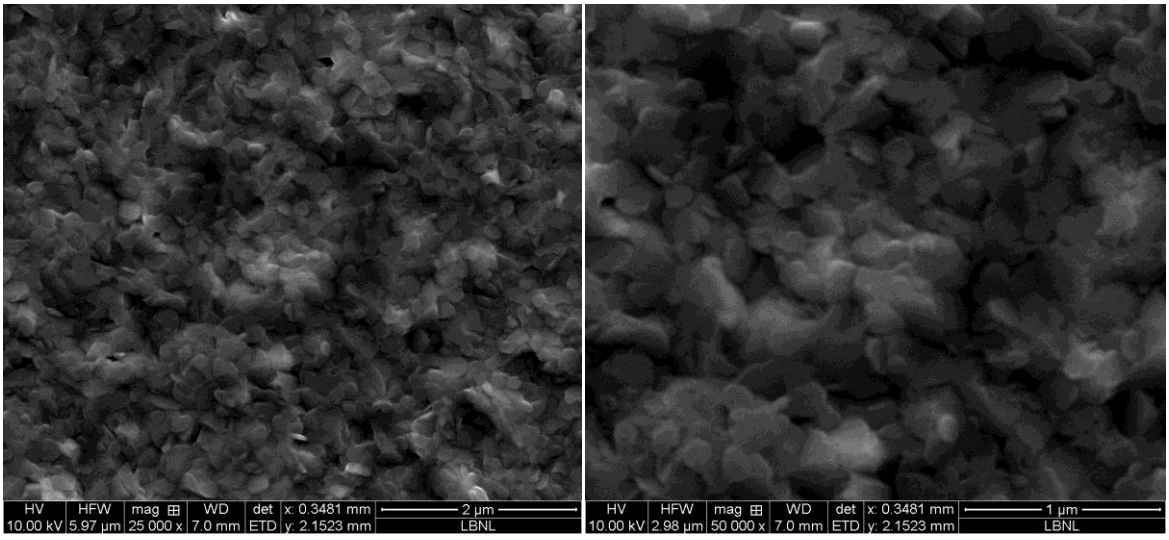

Figure 2.7: Spin coated PbI_2/$PbBr_2$ layer before the LP-VASP

In **Figure 2.8** it is possible to appreciate the good quality of the $MAPbI_3$ layer due to pinhole-free and homogeneous film. The morphology of the lead precursor layer is completely different compared to the perovskite layer after the conversion with the LP-VASP.

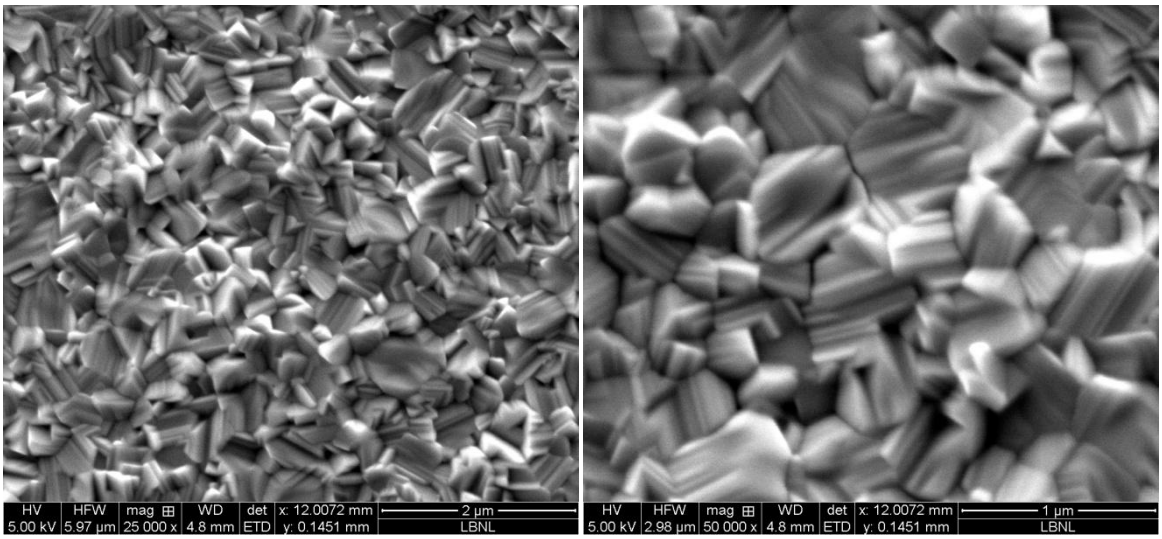

Figure 2.8: Top view of the $MAPbI_3$film

To have a confirmation of the chemical composition of the layer it is possible to record the X-ray diffraction (XRD) patter of the thin film using the grazing incidence geometry (parallel beam- parallel slit analyzer, PB-PSA). To completeness the XRD of both the perovskite and the lead halide films are reported (**Figure 2.9**).

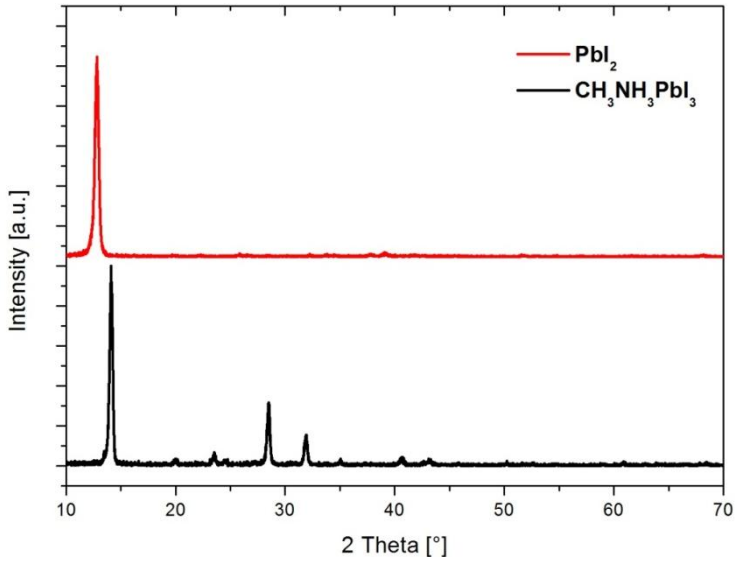

Figure 2.9: XRD spectra of PbI_2/$PbBr_2$layer and of $MAPbI_3$ obtained with LP-VASP.

From the XRD analysis in general it is possible to extract many information as for example the crystal phase, the lattice parameters of the crystals, the crystal grain orientation, the amount of the unconverted PbI_2 and it is possible to roughly evaluate the halide ratio in the mixed halide perovskite due to visible shift of some peaks. In our case the main indication is about the presence or not of unconverted PbI_2 precursor: the complete conversion into the organo-lead halide perovskite material is a must for high

efficient solar cell. Thanks to the LP-VASP in the final layer no PbI_2 is detected how it is possible to notice from the comparison between the XRD patterns of the initial and the converted films (**Figure 2.9**). The main signal measured at 12.6° from the $PbI_2/PbBr_2$ precursor layer is attributed to the lead iodide specie with (001) orientation. The same peak is not present in the XRD pattern of the perovskite layer indicating a full conversion of the precursor film into the desired perovskite material. Unlike the previous spectra, the $MAPbI_3$ spectra (**Figure 2.10**) is characterized by the presence of several peaks attributed to the different tetragonal perovskite lattice orientations, as below reported:

- 14.2° (002)/(110)
- 28.7° (004)/(220)
- 32.3° (114)/(222)/(310)
- 40.6° (224)
- 42.9° (411)
- 43.2° (314)

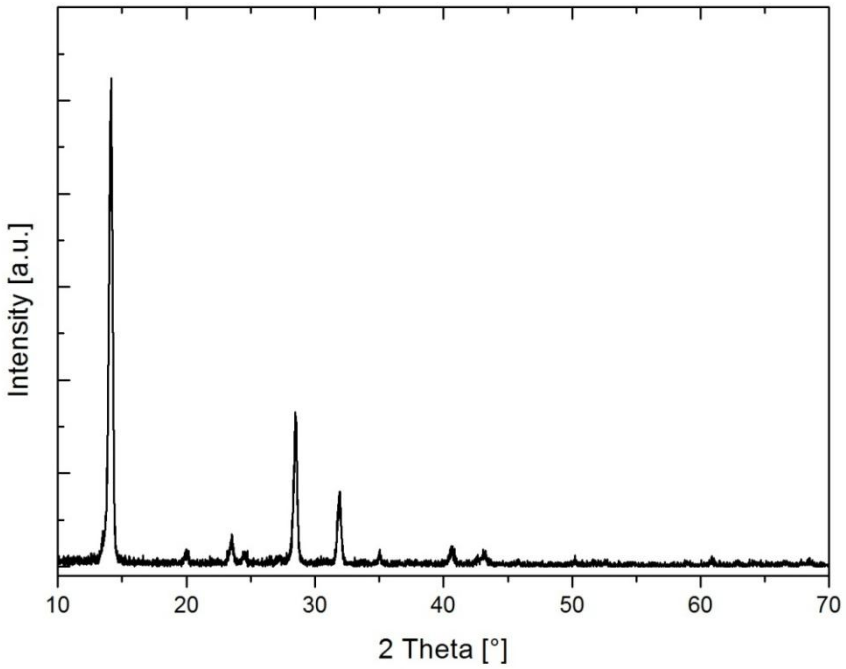

Figure 2.10: XRD spectra of $CH_3NH_3PbI_3$ (LP-VASP)

The characterization with UV-Vis spectroscopy allows to measure the absorption spectra (**Figure 2.11**) of the material. From this it is possible to calculate the absorption coefficient in function of the wavelength and also to determine the energy band gap with the Tauc plot analysis.

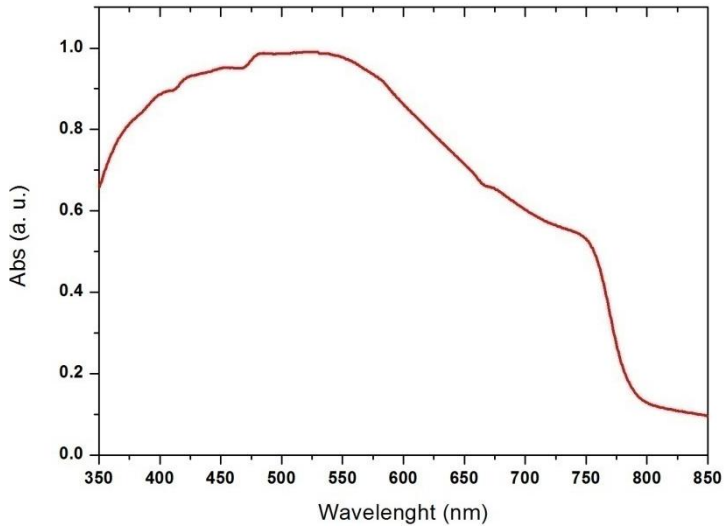

Figure 2.11: UV-vis spectra of $CH_3NH_3PbI_3$

The transmittance *T* is the fraction of the light transmitted through the layer and measured with the UV-vis spectrophotometer; from *T* is possible to obtain the absorbance (*A*) of the material due to the relation (**2.1**):

$$A = -log_{10}T \qquad (\mathbf{2.1})$$

For the thin film the absorption coefficient (α) might be approximately expresses as following:

$$\alpha \approx A/d \qquad (\mathbf{2.2})$$

where *d* is the thickness of the layer expressed in cm. To extract the band gap of the material it is necessary to convert the UV-vis data to obtain the so called Tauc Plot (**Figure 2.12**) described by the following relation (**2.3**):

$$(\alpha h\nu)^{1/r} = h\nu \qquad (\mathbf{2.3})$$

where r assumes different value depending on the nature of the transition:

- *r* = 1/2 direct allowed transitions
- *r* = 3/2 direct forbidden transition
- *r* = 2 indirect allowed transition
- *r* = 3 indirect forbidden transition

In this case *r*is equal to ½ since theperovskite semiconductor is a direct band gap material. In the **Figure 2.13** the curve shows a distinct linear region: the fitting of that region gives a straight line that cross the x axis. The value at the intersection between the abscissa and the straight line represents the band gap.

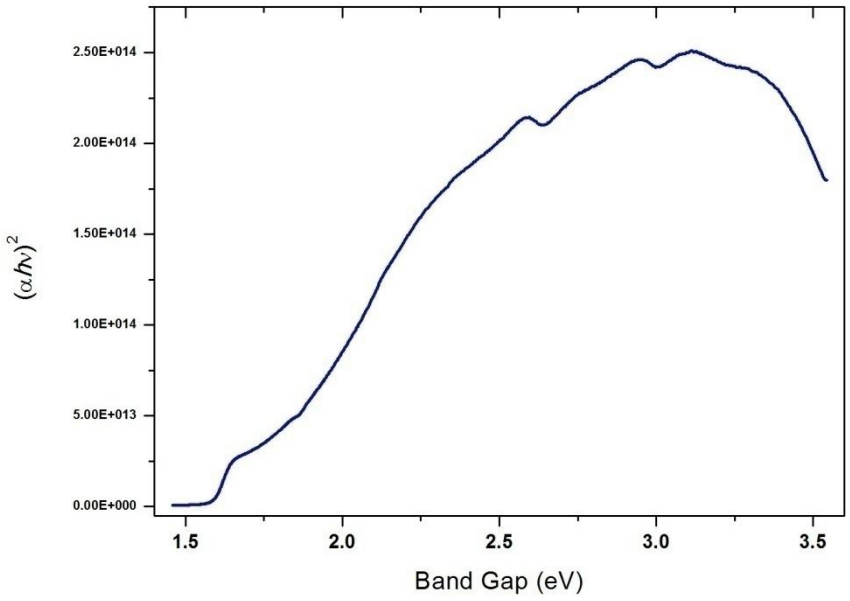

Figure 2.12: Tauc Plot of the $CH_3NH_3PbI_3$ (LP-VASP)

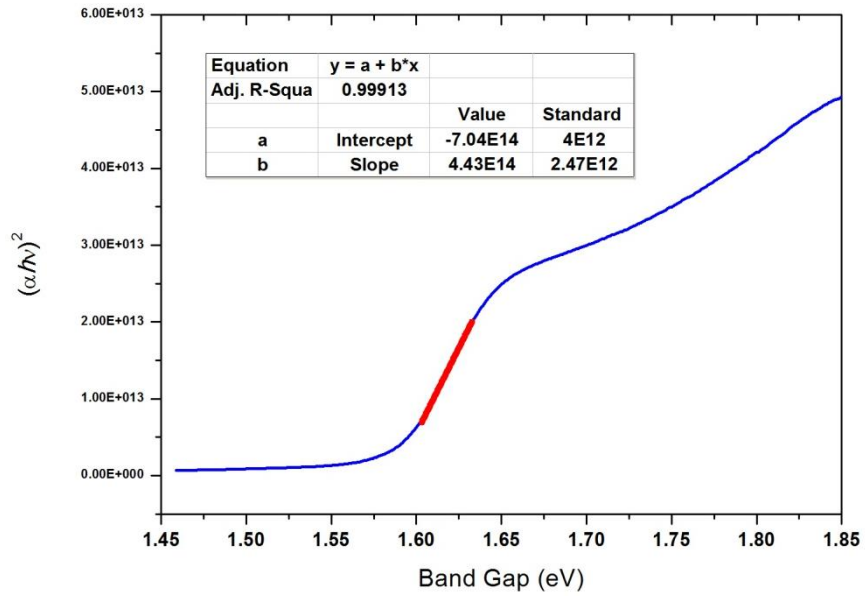

Figure 2.13: Magnification of the linear region used to extract the E_g of the $CH_3NH_3PbI_3$ (LP-VASP).

From the reported Tauc plot the extracted band gap is 1.59 eV which is in good agreement with the E_g reported in literature, while the R squared equal to 0.99913 proves the good fitting (red line) of the linear region.

2.2.2. Sequential Dipping for $CH_3NH_3PbI_{3-x}Br_3$ Cubic Perovskite

The fabrication of the $CH_3NH_3PbI_{3-x}Br_3$ perovskite cubes is a two step-process which involves: 1) the spin coating of the lead halide precursor, and the conversion of this precursor in the perovskite material *via* 2) a dipping step.

2.2.2.1. Step 1: Lead Halide Precursor Deposition

The total concentration of the lead halide precursor solution was usually 1 M in DMF, with 0.8 M of PbI_2 and 0.2 M of $PbBr_2$.The halide precursor solution is prepared by dissolving the lead powders in the DMF solvent then filtered with a PTFE syringe filter (0.45 µm). The solution is heated at 110°C for 10 minutes then 90 µL of standard precursor is dropped on the sample during the first 5 seconds of the spin coating process. The spin coating process is divided in 2 parts: during the first 5" the substrate is slowly accelerated at 500 rpm, the solution is deposited on the substrate, and then the speed is ramped to 1500 rpm and kept steady for 3'. At the end of the spin coating the sample is dried on the hot plate at 110°C for 15'.

The SEM images (**Figure 2.14**) show how the morphology of lead halide layer before the conversion into organo-lead halide perovskite: it is possible to appreciate the uniform, continuous coverage of the surface.

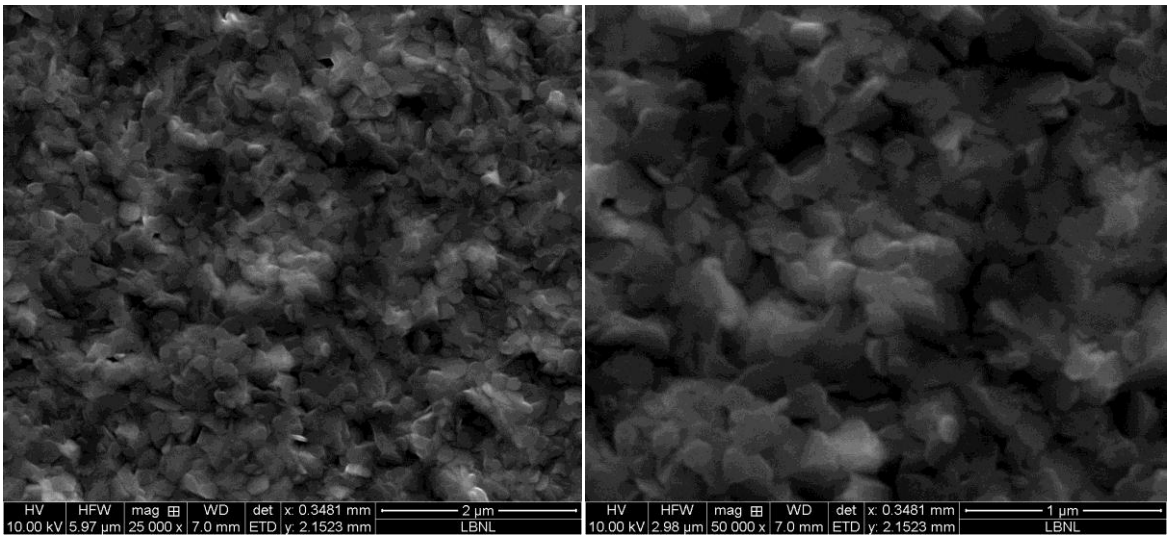

Figure 2.14: Spin coated $PbI_2/PbBr_2$ layer before the LP-VASP

2.2.2.2. Step 2: Solution Dipping for Halide Perovskite Cubes

The dipping step is necessary to convert the mixed $PbI_2/PbBr_2$ layer in the halide perovskite photoactive material. This dipping step is performed by using methylammonium halide (MAX, X = I or Br) dissolved in IPA as the solvent. Since the precursor is a mix of two different lead halide species (PbI_2 and $PbBr_2$) the composition of the resulting organo-lead halide perovskite will depend on the nature of the halide part (I or Br), thereby being either almost iodine pure ($MAPbI_{3-x}Br_x$) or almost bromine pure ($MAPbBr_{3-x}I_x$). From the XRD patterns it is possible to have an indication of the ratio between the two halide atoms in the perovskite phase, the preferential orientation of the perovskite lattice ,as well as the presence of the unconverted PbI_2.

Several dipping conditions have been investigated in order to optimize the process. The first trials were carried out at the IOM-CNR labs in an anaerobic chamber with stable oxygen and humidity levels (H_2O 100 ppm and O_2 500 ppm), and higher compared to a tightly controlled glove boxes (H_20 < 0.5 ppm and O_2 < 0.1 ppm). Then, I have studied the details of the process while at LBNL. Indeed, the first task at LBNL was to reproduce the morphology obtained in Trieste, and this process has allowed us to clarify significant parameters involved in the control of the growth and morphology of the final material.

While the first step of the deposition of the lead halide precursor is highly reproducible as it does not require specific conditions, the critical point in the synthesis is the second step, i.e. the dipping. Since an anaerobic system similar to the one used in Trieste was not available at the LBNL, the first experiments were carried out in a glove box, leading to different morphologies than expected: in particular no cubic crystals were present on the surface. The different morphology might depend on the different amount of residual water in the glove box with respect to the anaerobic box. Similar results are obtained if the experiments are performed in the fume hood without any particular control on the level of humidity and oxygen. In this case the amount of water is too high. In addition, it is important to keep in mind that the hybrid organic-inorganic halide perovskite material is not stable under high amounts of water and oxygen due to its hygroscopic nature. For this reason intermediate conditions were explored: a glove bag (plastic bag filled with a N_2) was used to control the moisture, but again no improvement was obtained. Trying to reproduce as much as possible the anaerobic system used in the

experiments in Trieste anhydrous IPA was used in glove bag and samples with the good morphology were finally obtained. To explore all the conditions the experiment was carried out also in the fume hood using anhydrous IPA. Since the samples obtained were not different from those using the glove bag with the anhydrous solvent it is decided to perform all the experiments in the chemical hood using fresh spilled anhydrous IPA every time. In this way, the practical aspects of the experiments could be simplified (the hot plate and all other necessary equipment were already present under the fume hood).

Before each dipping the samples are rinsed for 10" in anhydrous IPA to pre-wet the layer; this step has a strong impact on the conversion process.[7] After the dipping into the MAX/IPA solution, the sample is dried with flow of N_2 then annealed at 110°C for 10', to remove the solvent and to complete the conversion of the film into halide perovskite.

The first dipping process was tried in anhydrous IPA with dissolved MAI. As previously mentioned two are the main factors affecting the dipping step: i) the concentration of the solution and ii) the dipping time. To grow the desired cubic like crystals the concentration required ranges between 5 and 10 mg/mL while the dipping time must be short (within a couple of minutes). The concentration we used was 50.3 x 10^{-3} M (8 mg/mL)[8] and is in agreement with the concentrations used for the sequential deposition[9,10] of 10 mg/mL (the cubic crystals were synthesized trying to reproduce the sequential deposition method). For this reason during the optimization of the process we decided to keep constant the concentration and vary only the dipping time. After the dipping in MAI/IPA solution for different time (30", 60" and 90") homogeneous coverage of **poly-faceted** $MAPbI_{3-x}Br_x$ perovskite crystals corresponding to the tetragonal phase were obtained.

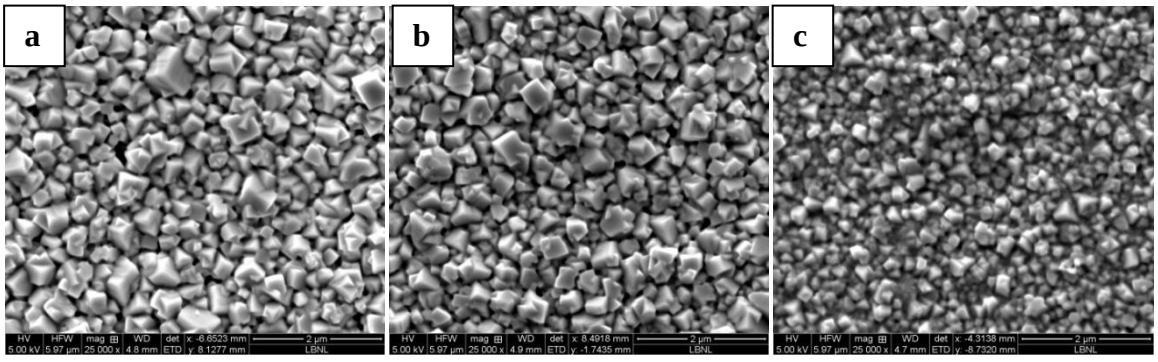

Figure 2.15: Halide perovskite layers obtained with dipping of the PbI_2 precursor into the MAI/IPA

The SEM images (**Figure 2.15**) of the layer reveal that the grains are not well separated and more likely they are merged into each other. With a dipping time of 30" and 60"the obtained films are very similar from the morphological point of view; on the other side with 90"the grains edges are not so defined and the cubic-like shape is partially lost. Also the grain size is slightly affected by the dipping time: again with 30" and 60" the size of the crystal domains ranges between 300-500 nm ,though bigger crystals can be also detected.

By XRD measurements it is possible to evaluate the degree of conversion of the lead halide precursor in the organo-lead halide perovskite material. The XRD spectra (**Figure 2.16**) for the layers with different dipping time is reported and compared to that of the untreated PbI_2. The first information extracted from the graph is that the dipping step of duration up to 90"is not enough to convert entirely the PbI_2 in the photoactive material, as it is clearly demonstrated by the presence of a large peak at 12.8° ((001) crystal plane of the PbI_2 precursor).

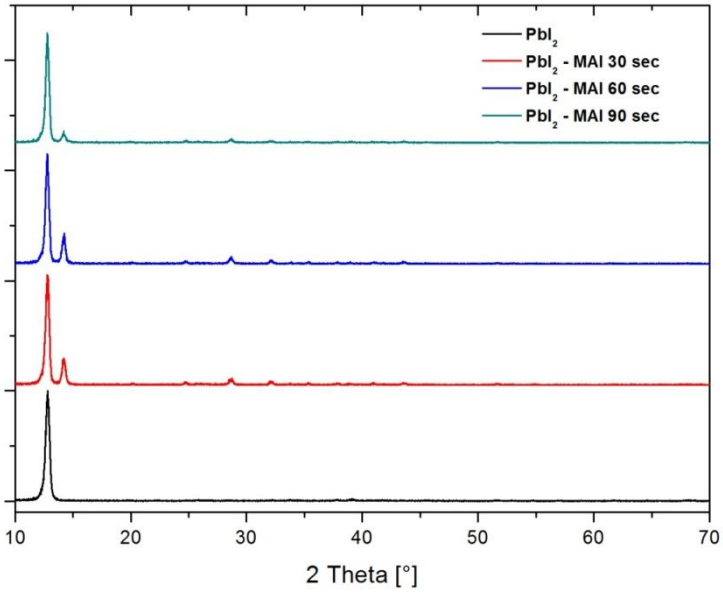

Figure 2.16: XRD spectra of the $MAPbI_{3-x}Br_x$ layers obtained after the dipping step into the MAI/IPA solution with different dipping times: 90" (light blue), 60" (blue), 30" (red) and PbI2 (black - reference)

At 14.3° (002)/(110) it is possible to find a smaller peak related to the tetragonal phase $MAPbI_{3-x}Br_x$ (14.2° is reported for the pure $MAPbI_3$). The signal intensities give an indication of the lead content present as bare precursor and as converted in halide perovskite. At 28.7° (004)/(220) and 32.3° (114)/(222)/(310) two more peaks with low intensity are assigned to the halide perovskite phase.

The second dipping process was tried in a different solution where MABr instead of MAI was dissolved in anhydrous IPA. The solution in this case is slightly less concentrate 44,7 x 10^{-3} M (5 mg/mL) due to the lower solubility of the MABr powder in anhydrous IPA.

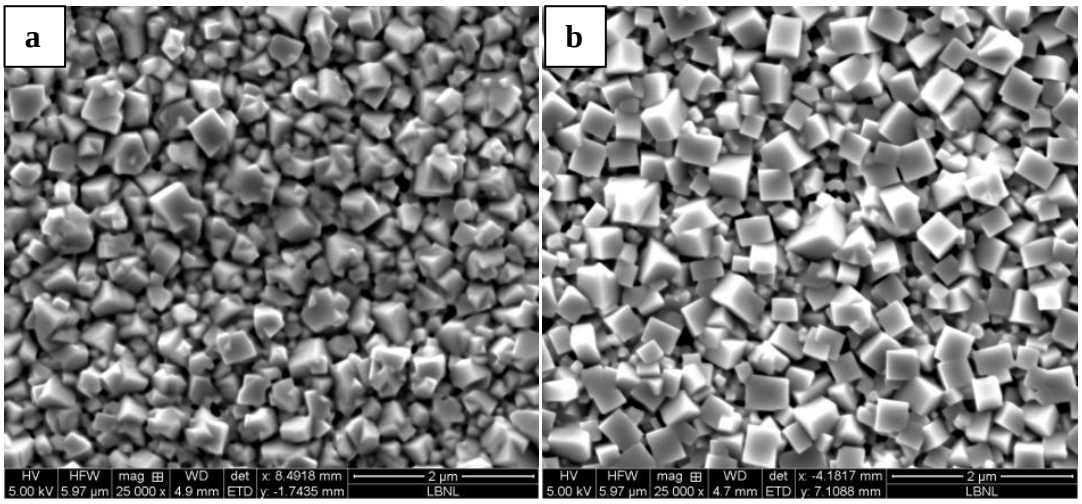

Figure 2.17: Perovskite layers obtained with the dipping step in: a) MAI/IPA ($MAPbI_{3-x}Br_x$) and b) MABr/IPA ($MAPbBr_{3-x}I_x$)

From the SEM images (**Figure 2.17**) here reported, it is possible to notice how the obtained morphology differs by changing the methylammonium halide solution used for the dipping (conversion) process. On the left (**Figure 2.17a**) it is again reported the film obtained dipping the lead halide layer into the MAI/IPA solution for 60", while on the right (**Figure 2.17b**) it is possible to appreciate the morphology obtained with the MABr/IPA solution at the same dipping time. With the bromide anion it is possible to obtain cubic grains with well-defined facets and sharp crystal edges. Due to the grain quality of the halide perovskite crystals, this morphology is more suitable for the c-AFM measurements used to study the relation between the photoelectrical properties and the crystal lattice orientation.

By comparing the XRD spectra (**Figure 2.18**) of the two layers it is possible to notice several differences and some analogies. First of all, also in this case the dipping in the MABr/IPA solution is not sufficient to convert entirely the precursor into the desired organo-lead halide perovskite semiconductor. At the same time, comparing the signal of the PbI_2 to that of the halide perovskite in both cases of conversion (with MAI/IPA and MABr/IPA) it is possible to observe that the relative intensity of the perovskite film is obtained by conversion in the MABr/IPA. Moreover the perovskite signal with the MABr

dipping is shifted to higher 2 theta angles (14.8°) because the solution enrich the halide perovskite phase with the Br^- anion instead of the I^- anion. Also the $MAPbBr_{3-x}I_x$ signals present at higher angels (29.9° and 33.5°) are both shifted and more intense compared to those obtained with MAI/IPA dipping, confirming a higher degree of conversion and the compositional differences. Additionally, for your information the $MAPbBr_{3-x}I_x$, is stable in the cubic phase.

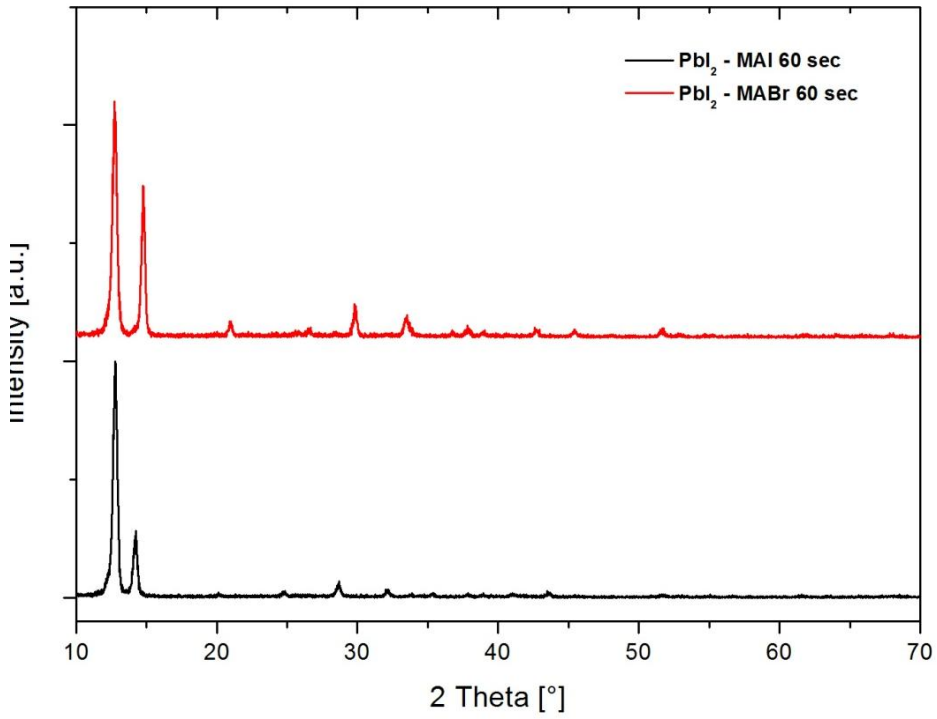

Figure 2.18: XRD patterns of the perovskite layers obtained with the dipping step in MAI/IPA ($MAPbI_{3-x}Br_x$ - black curve) and in MABr/IPA ($MAPbBr_{3-x}I_x$ - red curve).

A full coverage of the substrate by the halide perovskite layer is necessary to obtain high efficiency solar cells; the presence of a high amount of unconverted lead halide precursor is not optimal for a good device.

For these reasons it is important to obtain a cubic-like morphology with both good coverage and full conversion of the lead into the perovskite phase.

To characterize properly the cubic-like crystals it is important to have them as much as possible as pure halide perovskite in order to minimize the PbI_2 contribution to the measurements. The conversion issue is the first taken into account so the attention is now focused on the optimization of the conversion process, without modifying the other steps and the structure of the layer.

2.2.2.3. Optimization of the CH_3NH_3Br/IPA Dipping Step

The first approach investigated in order to reduce the presence of unconverted $PbI_2$was to vary the dipping time. The previous section reported on the sample obtained after 60” of dipping; starting from this point it was decided to study how the dipping time influences the morphology and the composition of the final layer.

Keeping in mind that for cubic-like crystals short dipping steps are mandatory, 4 samples with different dipping time: 30”, 60”, 180” and 300” were prepared. The SEM images (**Figure 2.19**) below allow to appreciate how different morphologies result from varying the dipping time. Increasing the latter produces cubic crystal domains of smaller size: while the samples obtained at 30”, 60” and 180” are similar to each other, at 300” dipping time the grains are smaller and less defined. With the 60” dipping time it is possible to notice the grain size is around 1 µm and the crystals are separated. At 30” the grains are close to each other while at 180” they have different sizes indicating a possible transition from big grains to smaller ones.

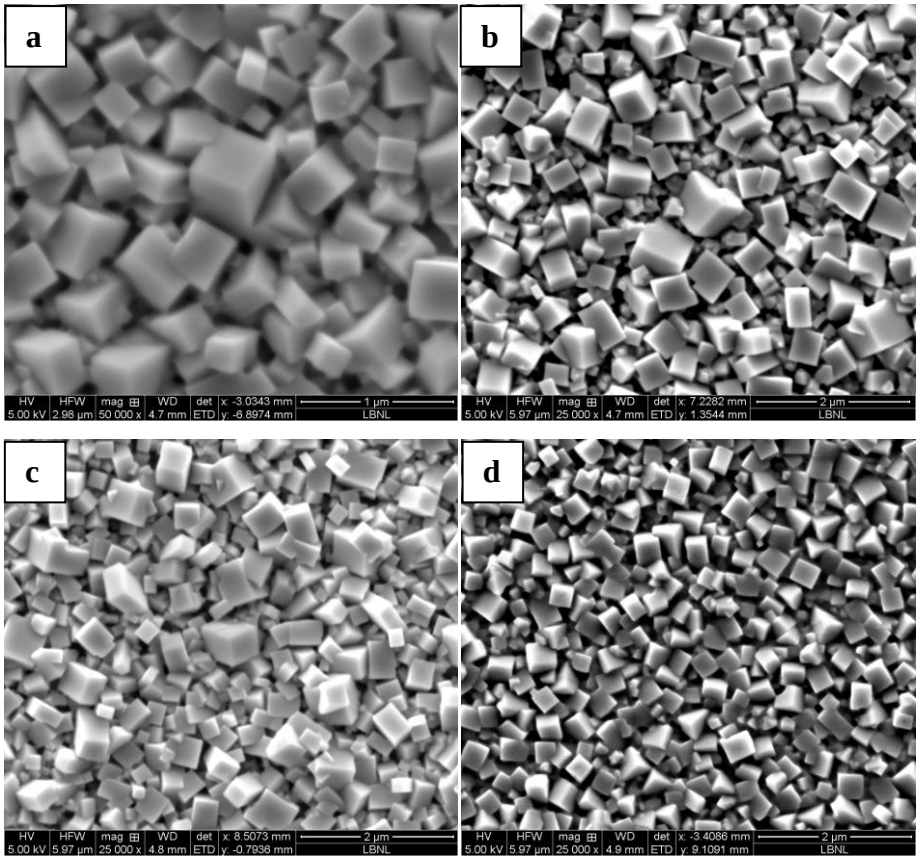

Figure 2.19: SEM images of cubic $MAPbBr_{3-x}I_x$ crystals obtained with different dipping times in MABr/IPA: a) 30”, b) 60”, c) 180” and d) 300”.

Even if the crystal shape is mainly retained with small differences depending on the duration of the dipping step, the main interest is focused on the PbI_2 conversion. To evaluate the reaction XRD spectra (**Figure 2.20**) were collected for all samples.

From the XRD patterns, it is clear that the PbI_2 signal (12.8°) is still present confirming the difficulty of converting entirely the precursor in halide perovskite (14.8°) with short dipping. Furthermore comparing the signal intensities it is possible to notice that there is a direct relation between the conversion rate and the dipping time: the longer is the dipping step the higher is the amount of PbI_2 converted in methylammonium lead halide perovskite. The intensity of the organo-lead halide perovskite signals are much higher compared to those obtained with the MAI/IPA (**Figure 2.16**), suggesting a higher conversion rate for the Br^- anion. An hypothesis to rationalize this fact is that the small Br^- anion can diffuse/migrate faster in the PbI_6 and/or in the already formed perovskite lattices as compared to the I^- anion. Nevertheless, the amount of the PbI_2 also in the case of conversion with MABr/IPA is still high after 5 minutes of dipping.

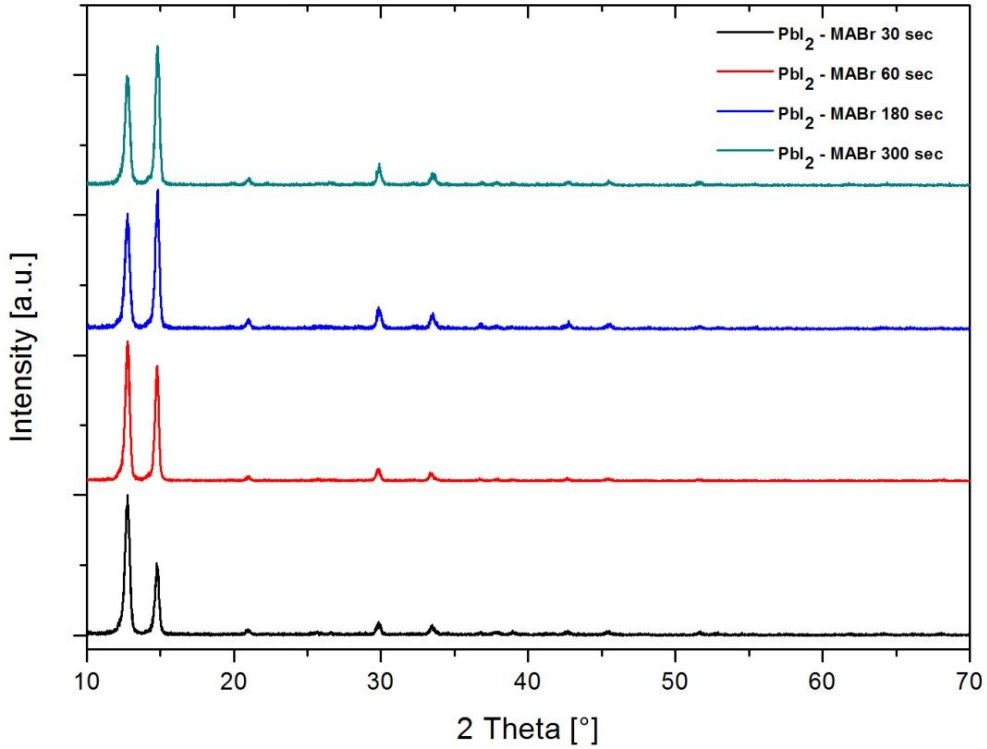

Figure 2.20: XRD spectra of cubic $MAPbBr_{3-x}I_x$ crystals obtained with different dipping times in MABr/IPA: 30" (black), 60" (red), 180" (blue) and 300" (light-blue).

Although the overall morphology consists of well-shaped cubic micro-crystals, the composition of the halide perovskite layer still presents a high amount of unconverted PbI_2 precursor.

2.2.2.4. Multi-dipping Approach

The second approach attempted in order pushing up the rate of PbI_2 conversion into perovskites while retaining the crystal shape was to repeat the dipping process several times. What was noticed from the previous experiment is that with long dips (5 minutes) the crystal shape changes, as well as the grain size. This phenomenon is probably due to the equilibrium between the crystal growth and the dissolution of the grains back into the solution. Since after each dipping the sample is annealed on the hot plate, we made the hypothesis that after drying and stabilizing the halide perovskite layer, if immersed again into the MAX/IPA solution the crystals would start grow again at the expenses of the PbI_2as if immersed for the first time into the solution. Basically we would like to test whether the fact that there is a certain period of time before the crystal growth/grain dissolution equilibrium is reached could be exploited to push up the degree of the conversion retaining the crystal shape.

Three samples were prepared increasing linearly the number of dipping: the first was dipped one time, the second twice and the last one three times. Below the SEM images (**Figure 2.21**) are reported to show the resulting morphologies: the pictures are referred to the layers obtained with one (**Figure 2.21a**), two (**Figure 2.21b**) and three (**Figure 2.21c**) dipping steps. Each immersion of the sample into the solution was lasting 60”, since in the previous experiments the best samples were obtained with this value. After each dip the samples were annealed at 110°C for 10 minutes. It is possible to notice that after the second dip the crystal shape is still retained but the homogeneity of the layer is lower compared to the one-dip sample. After the third dip, the grain edges are not so sharp and defined; it is also possible to notice the smaller crystal dimensions.

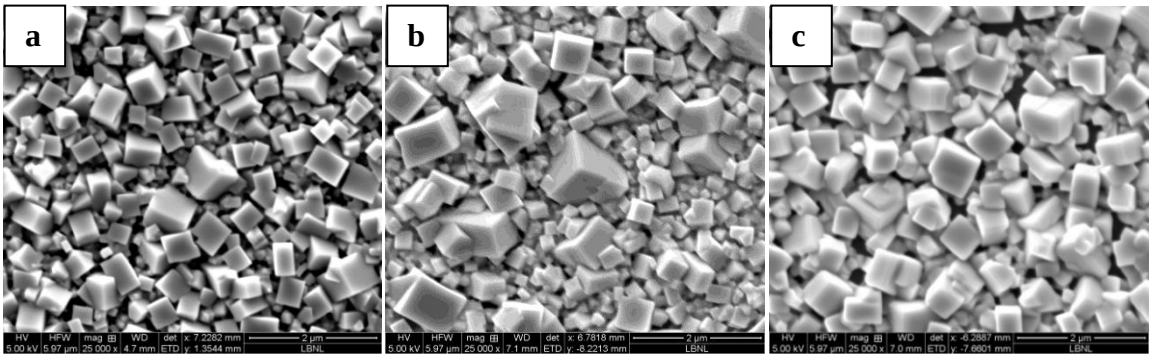

Figure 2.21: $MAPbBr_{3-x}I_x$ crystals obtained with multi-dipping approach: a) one dipping, b) two dippings and c) three dippings.

To evaluate the conversion rate obtained with the multi-dip approach, again the XRD patterns (**Figure 2.22**) are collected for all samples and the $PbI_2$and $MAPbBr_{3-x}I_x$ peaks are compared: the spectra report the signals in the region between 10° and 16°. In this case the intensities of the lead halide (12.8°) peaks are again present, while the intensity of the halide perovskite signal (14.8°) decreases after the second dipping. Both the SEM and the XRD characterization suggest that dissolution or detachment of the organic-inorganic halide perovskite material from the substrate has occurred.

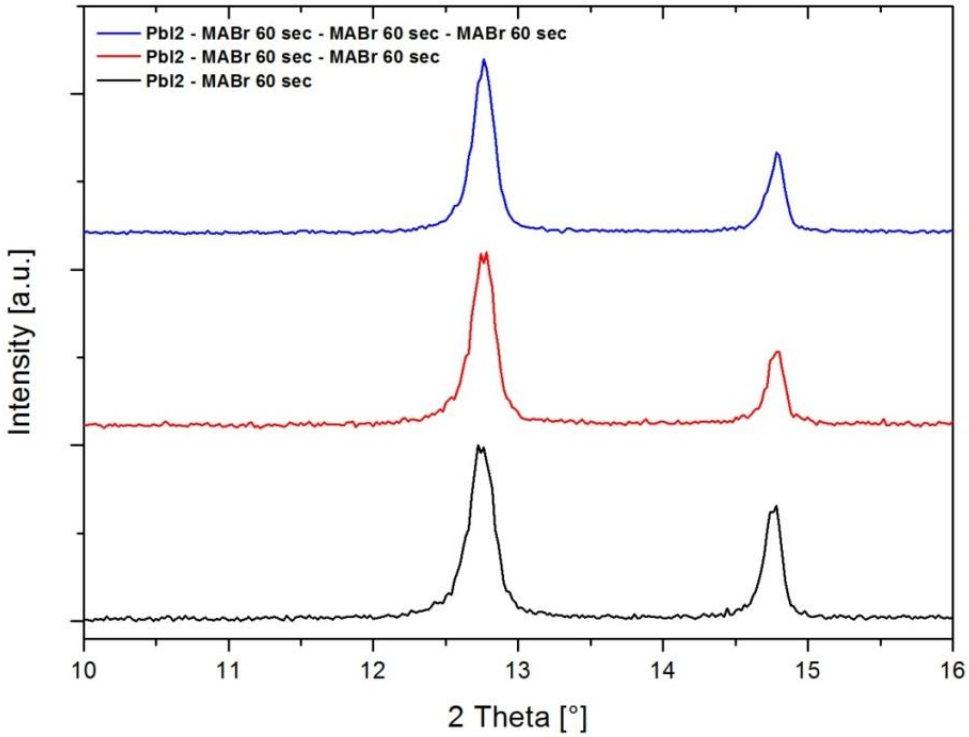

Figure 2.22:XRD spectra of $MAPbBr_{3-x}I_x$ crystals obtained with multi-dipping approach: one dipping (black), two dippings (red) and three dippings (blue).

2.2.3. Sequential Dipping and LP-VASP

To solve the conversion issue a third approach is taken in account. The idea of using as the last step LP-VASP to complete the conversion raises from the possibility to use the same method developed at the Lawrence Berkeley National Laboratories to fabricate solar cells with high efficiency.

To prepare the sample, as usual the sample is rinsed for 10” in anhydrous IPA, immersed into the MABr/IPA solution for 60”, dried with N_2 flow and finally annealed on the hotplate for 10’ at 110°C. At this point the sample is loaded in the glass tube with

MAX powder and connected to the Schlenk line to start the LP-VASP (2h at 120°C) as explained in Chapter 3.

The initial concern was about increasing the conversion into halide perovskite while retaining the desired crystal shape. Surprisingly the overall morphology, even if different, still consists of cubic-like perovskite crystals. The SEM image below show the layer after the dipping step (**Figure 2.23a**) and after the LP-VASP (**Figure 2.23b**) obtained with MAI charged tube.

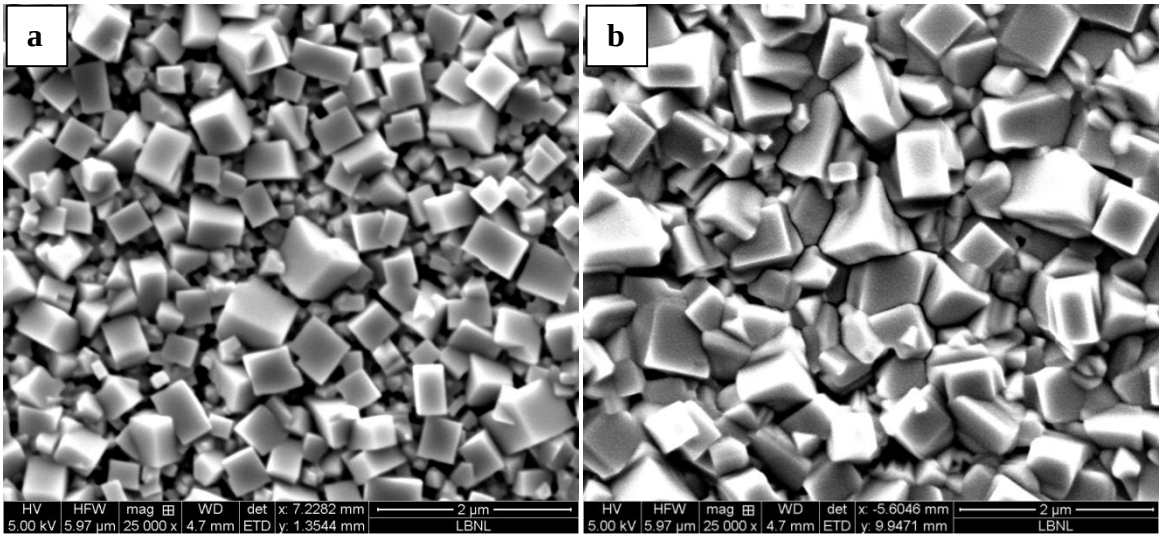

Figure 2.23: a) $MAPbBr_{3-x}I_x$ crystals after MABr/IPA dipping step and b) $MAPbI_{3-x}Br_x$ crystals after MABr/IPA dipping and LP-VASP (with MAI).

The uniformity of the layer appears higher compared to the sample after the dipping. Since during the LP-VASP the layer grows by embedding MAI into the PbI_6 lattice, less void spaces are present at the surface and also the crystals are not anymore so well separated. Even if from a morphological point of view the thin film is not the same as before the LP-VASP, still the crystals are well visible and it is possible to recognize the facets on the same grain.

From the compositional point of view the XRD spectra (**Figure 2.24**) show that the conversion is now complete: the PbI_2 peak is not present anymore while the $MAPbI_{3-x}Br_x$ signal (14.2°) has high intensity. This proves the photoactive material, as tetragonal phase, has a preferential crystal lattice orientation (002)/(110).

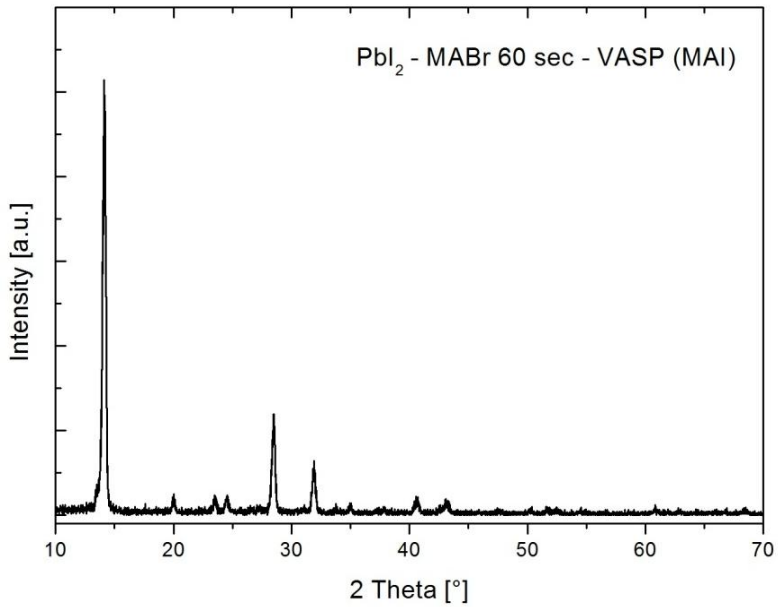

Figure 2.24: XRD spectrum of $MAPbI_{3-x}Br_x$ layer obtained after dipping step and LP-VASP with MAI.

From the XRD spectra reported below, it is possible to notice that pattern of the halide perovskite layer obtained with the LP-VASP with and without the intermediate dipping step are the same.

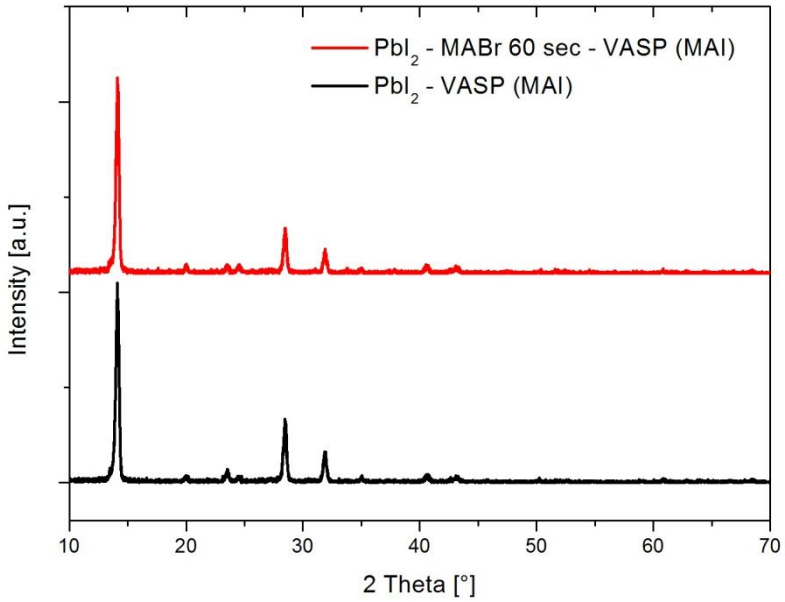

Figure 2.25: XRD spectra for the $MAPbI_{3-x}Br_x$ layer obtained with MABr/IPA dipping and LP-VASP (red) and LP-VASP (black)

The absorption spectra in the UV-vis range was collected to better characterize the obtained cubic-like halide perovskite layer: the intensity of the signal increases around 775 nm as expected for the $MAPbI_{3-x}Br_x$.

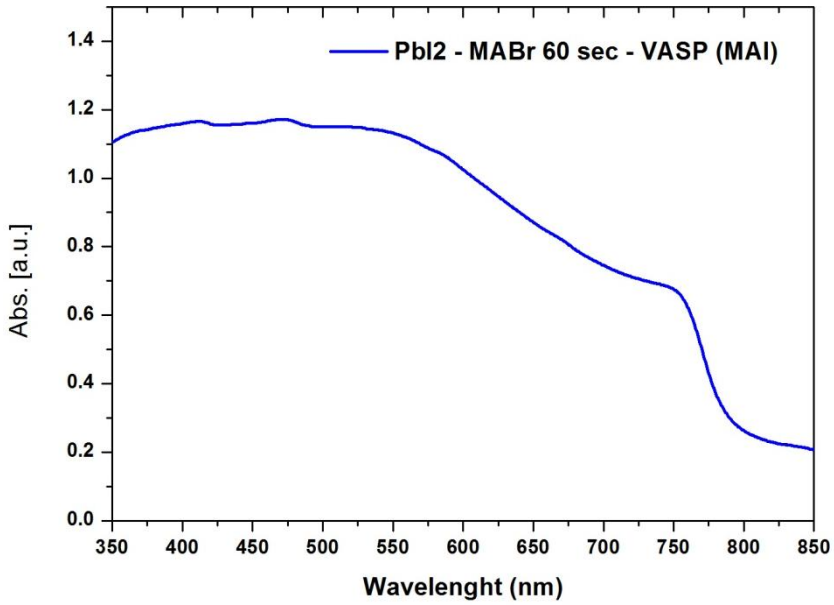

Figure 2.26: UV-vis spectra of $CH_3NH_3PbI_{3-x}Br_x$

As previously reported it is possible to extract the band gap of the material with the Tauc plot analysis: in this case the E_g is equal to 1.58 eV confirming the low bromine content in the $CH_3NH_3PbI_{3-x}Br_x$ layer, obtained after the LP-VASP conversion step

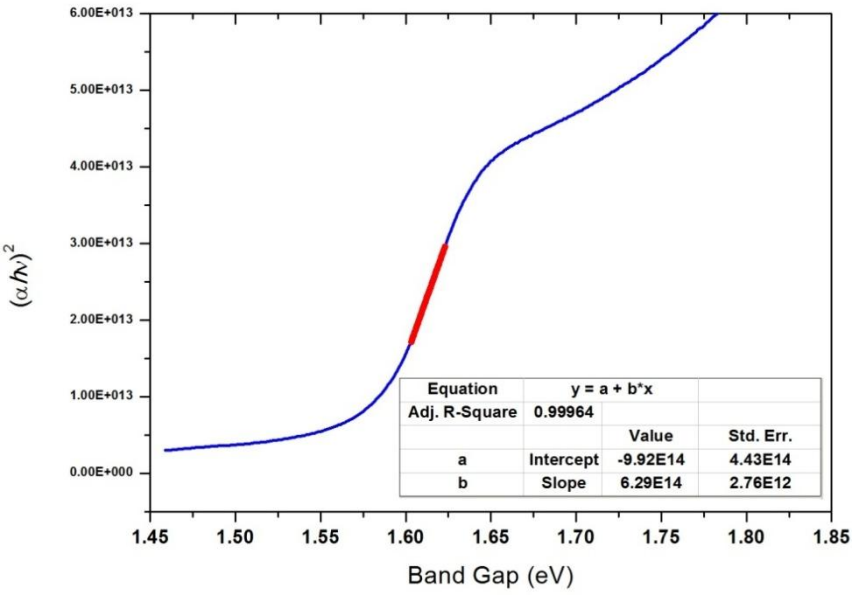

Figure 2.27: Magnification of the linear region used to extract the E_g of the $CH_3NH_3PbI_{3-x}Br_x$ obtained with dipping and LP-VASP.

Even if the main interest is focused on the pure $MAPbI_3$ (or $MAPbI_{3-x}Br_x$ most likely) perovskite film, due to the band gap and the possibility to compare the data with the optimized layer usually used for the solar cell, it was decided to carry out the same kind of experiments replacing MAI with the MABr for the LP-VASP process. As reported in

chapter 3, with this chemical it is possible to obtain the pure $MAPbBr_3$ (or $MAPbBr_{3-x}I_x$ most likely) perovskite layer.

The SEM images for the sample after 60"dipping in MABr/IPA (**Figure 2.28a**) and of the same sample after the LP-VASP (**Figure 2.28b**), using the MABr powder for the conversion, are shown below.

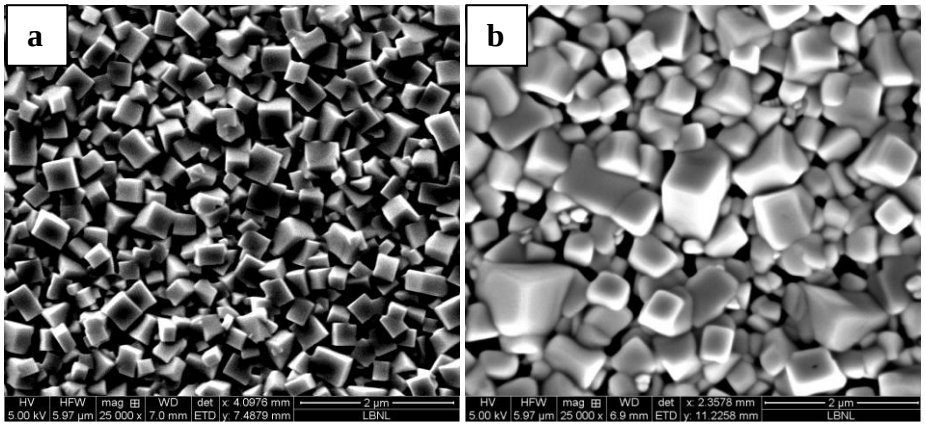

Figure 2.28: $MAPbBr_{3-x}I_x$ layer after a) MABr/IPA dipping and b) after MABr/IPA dipping and LP-VASP with MABr compound

The crystals after the dipping process had a cubic shape and defined grain edges (**Figure 2.28a**). On the contrary, by the LP-VASP with MABr powder the morphology was deeply influenced: the grain edges are not anymore well defined, even if the cubic-like shape is partially retained. Below are reported the XRD spectra (**Figure 2.29**) for the sample after the dipping step and after both the dipping and the LP-VASP steps with MABr in the region between 10° and 16°.

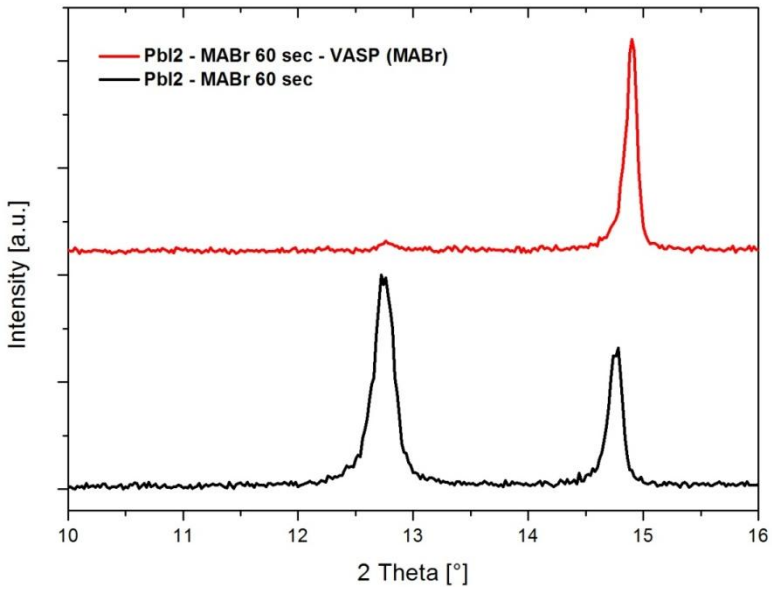

Figure 2.29: XRD spectra of the $MAPbBr_{3-x}I_x$ layer after the dipping step in MABr/IPA (black) and after the dipping step and the LP-VASP with MABr powder (red).

The XRD analysis shows that again the LP-VASP is a powerful tool to convert the PbI_2 layer into the desired halide perovskite phase. In this case comparing the patterns it is possible to observe that after the LP-VASP the $MAPbBr_{3-x}I_x$ signal (100) is slightly shifted to higher angles (14.90°) suggesting an almost pure bromine perovskite in the cubic phase.

Even if the conversion is basically completed also with the MABr powder used for the LP-VASP, the morphology is less suited to the electronic transport characterizations by c-AFM. Therefore, from now only MAI compound was used for the LP-VASP process.

2.2.3.1. Dipping Time Variation and LP-VASP

Other experiments were carried out trying to optimize the morphology of the cubic-like perovskite layer. For this reason the same experiments were performed also on samples obtained after the dipping process for different time. To have a comparison with the samples obtained with the previous trials, it was decided to dip the PbI_2 layer into the MABr/IPA solution for 30”, 60”, 180” and 300” before the conversion step with LP-VASP (as explained MAI powder was used for LP-VASP).

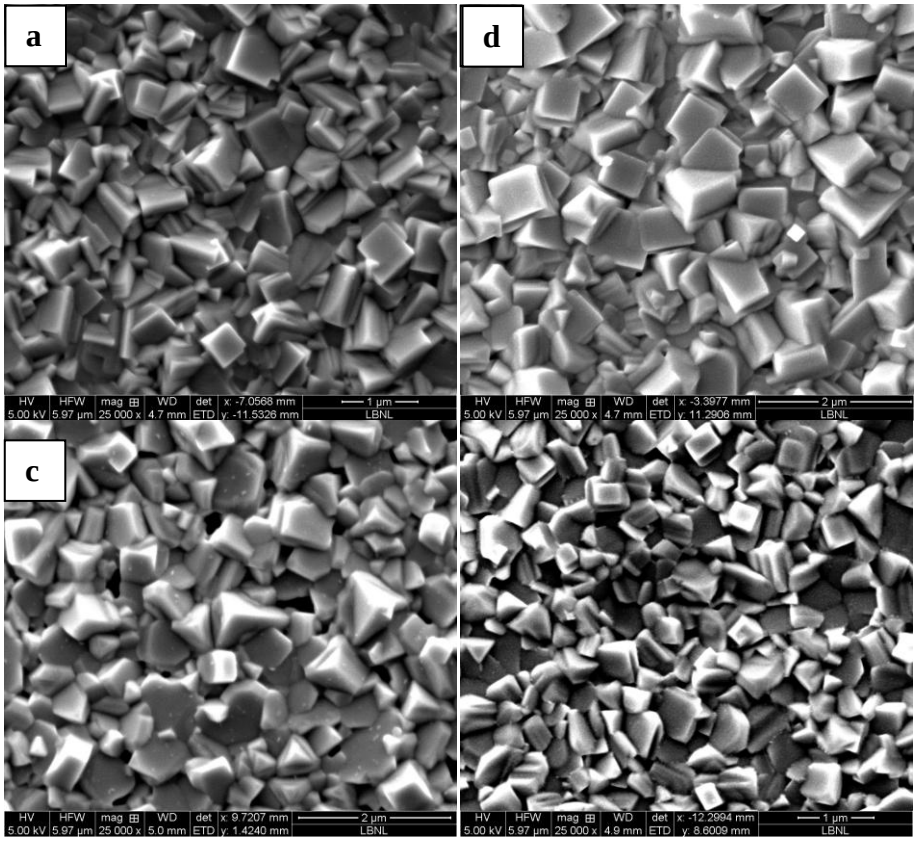

Figure 2.30: SEM images of the samples after 30” (a), 60” (b), 180” (c) and 300” (d) of dipping time followed by the LP-VASP process with MAI.

From the SEM images here reported (**Figure 2.30**) it is possible to notice the morphology after 30" is characterized by cubic-like crystals but the grains are merged into the halide perovskite layer and just few and small facets are exposed for the c-AFM characterization. On the other side, increasing the dipping time to 180" and to 300" the grains partially lose the characteristic shape and the morphology looks similar to the layer obtained with the usual LP-VASP without the dipping step.

Looking at the morphologies obtained after the processes the optimal Perovskite layer appears again to be the one obtained after the 60" dipping in MABr/IPA and the LP-VASP step.

2.2.3.2. Multi dipping and LP-VASP

Also the multi dipping approach (same procedure explained in section 3.2.2.2) is exploited again and optimized with the LP-VASP technique. The lead iodide layer is converted with one to three dipping steps into the MABr/IPA solution then converted with LP-VASP (with MAI powder).

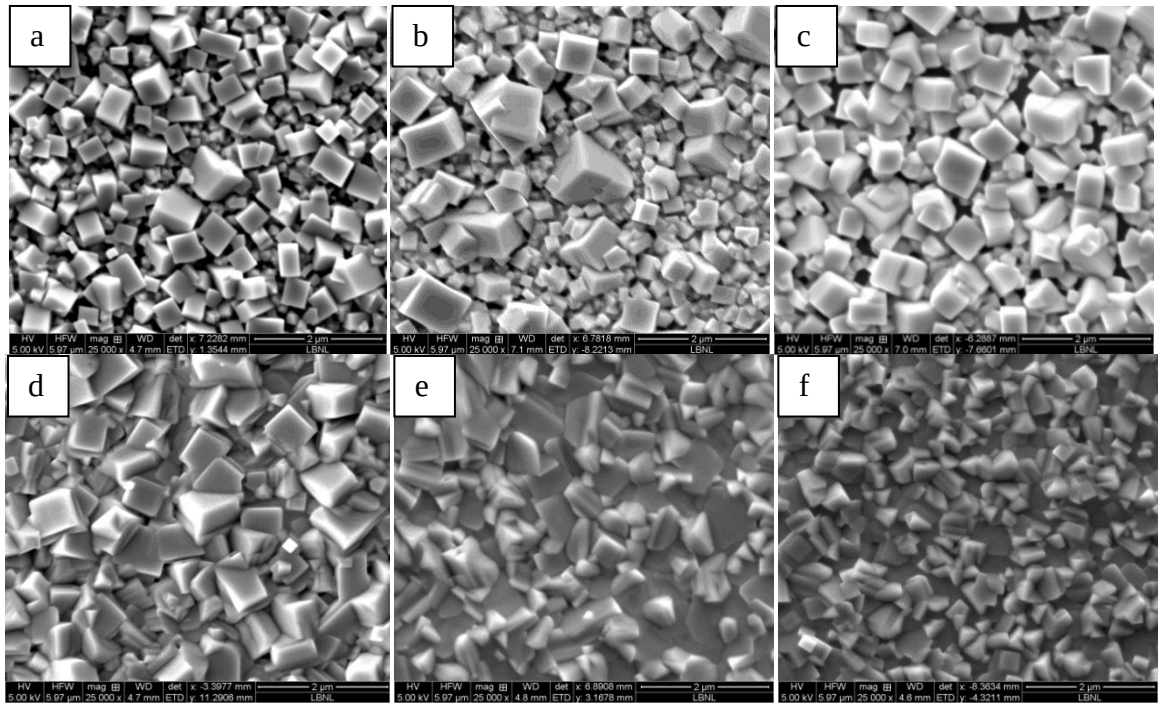

Figure 2.31: $MAPbBr_{3-x}I_x$ crystals obtained with multi-dipping approach a) one dipping, b) two dippings and c) three dippings. Below the corresponding samples with one dipping (d), two dippings (e) and three dippings (f), followed by the LP-VASP conversion.

The SEM images show that increasing the number of the dippings the morphology changes (**Figure 2.31a**: one dipping, **2.31b**: two dippings and **2.31c**: three dippings): taking

the “one dipping” sample as reference, after the second dipping the crystals lose the characteristic shape while after three dippings the grains are smaller and again without the characteristic cubic shape. In general with two and three dippings the layer surface is homogeneous and not interesting.Although the LP-VASP process modifies the morphology, the presence of the cubic crystals is regulated by the dipping step: if the layer after the dipping step is qualitatively poor this will be so and even more clearly after the LP-VASP.

Also in this case the multi dipping approach followed by the LP-VASP method for the complete conversion does not bring any improvement suitable cubic perovskite layer.

2.3. Synthesis of Big Crystals

To have a more complete picture on how the crystal properties may change, we decided to characterize grains with different sizes: here the main goal is to understand if there is some variation in the electronic transport properties of the semiconducting material with the dimension of the crystals. Since from the previous experiments it was noticed the shape of the crystals is basically controlled by the dipping step, it was decided to change some parameters kept constant for the procedures so far reported. The crystallization process may be divided in two main steps, both regulated by the thermodynamic and the chemical properties of the halide perovsktie material: the nucleation and the crystal growth.

The nucleation process is the first step, when a new crystal domain is formed and becomes the “seed” necessary for the second step, the crystal growth: the growth of the crystal cluster happens only on the aforementioned seeds. The two processes occur at the same time and they are directly affected by the thermodynamic conditions. For this reasons it is important to find the suitable conditions necessary to favor the crystal growth instead of the nucleation step. From a kinetic-thermodynamic point of view the nucleation process is slower than the crystal growth. To increase the probability to form new seeds, which will bring higher number of crystals with small dimensions, it is usually useful to increase the precursor concentration in the solution. On the other side if the opposite phenomena is desired (less crystals with large dimensions), it is necessary to decrease the concentration of the solution: in this way the atoms and the molecules should grow onto the existing crystals (thermodynamically favorable conditions).

The same approach is here used to grow larger grains with respect to those so far obtained. The concentration of the dipping solution is decreased from 5 mg/mL to 3 mg/mL. Below the SEM images (**Figure 2.32**) are reported and it is possible to notice the layer obtained with the 3 mg/mL concentrations after 3 and 5 minutes of dipping time:

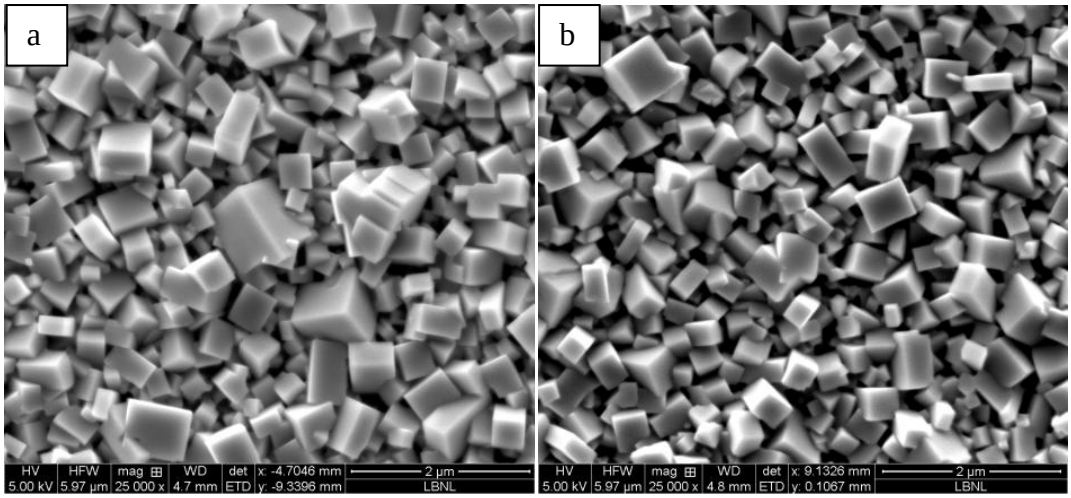

Figure 2.32: $MAPbBr_{3-x}I_x$ layers dipping the PbI_2 precursor in MABr/IPA (3 mg/mL) for 3' (a) and 5' (b).

It is possible to appreciate that the crystals obtained after 3 minutes are not so different from those obtained with the 5 mg/mL solution immersed 60". Some larger grains are present but the difference in the dimensions compared with the previous samples is too small to provide a clear indication if there is a variation related with the crystal dimensions. With 5 minutes dipping time it is possible to see that the crystals partially lose the sharp edges. Moreover with this dipping time the grain dimensions are smaller and crystal size more homogeneous, indicating that probably after 5 minutes the process may have approached an equilibrium between crystal growth and dissolution.

At that point it was decided to proceed decreasing again the solution concentration from 3 mg/mL to 1 mg/mL. Since the concentration is 5 times less than that one used usually it was decided to increase the dipping time to 5 minutes as starting point. From the SEM images (**Figure 2.33**) here reported it is possible to notice how the dimensions of the grains are now significantly bigger (2-3 µm):

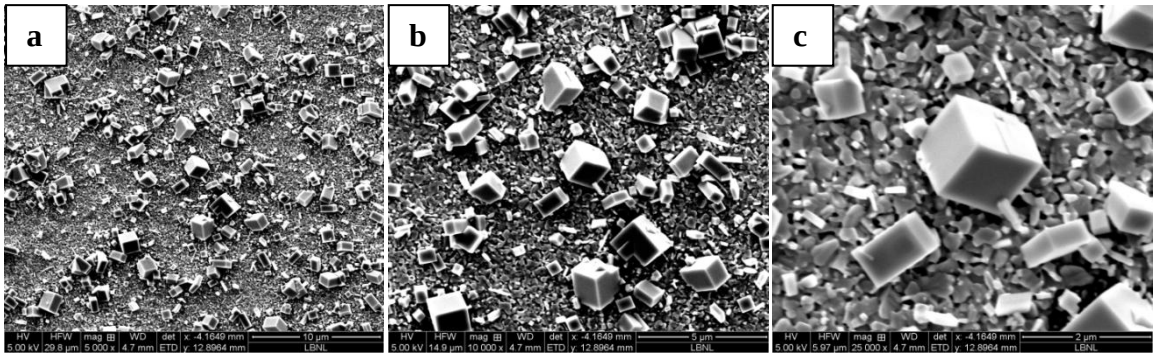

Figure 2.33: Three different magnifications of the same sample obtained with the dipping of the PbI_2 substrate for 5 minutes in MABr/IPA solution (concentration 1 mg/mL).

As expected the crystals are bigger but the layer is not anymore uniform, although a uniform layer of small size (50-200 nm) domain is covering the surface of the substrate. The facets of the crystals are well exposed and it is possible to appreciate the sharpness of the edges. Trying to grow even bigger crystals we decided to increase the dipping time to 15 and 30 minute.

From the SEM images (**Figure 2.34**) it is possible to notice that the dimensions of the grains are slightly bigger but still in the range of the crystals obtained with 5 minutes of dipping.

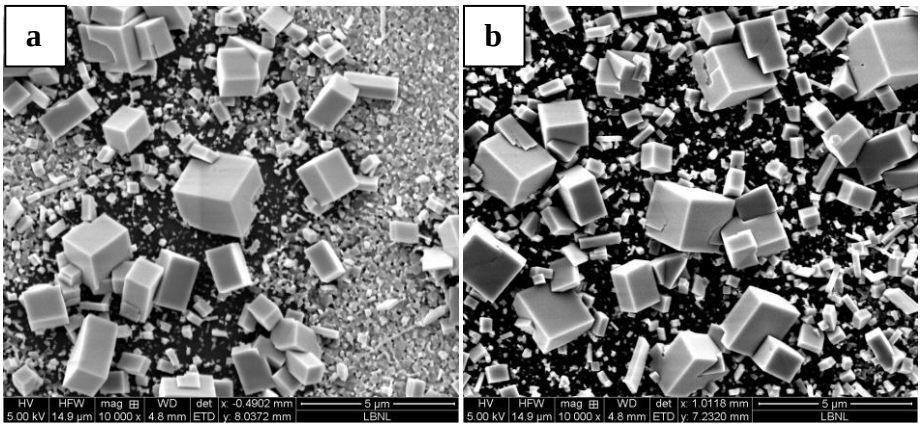

Figure 2.34:$MAPbBr_{3-x}I_x$ crystals after the dipping of the PbI_2 film in MABr/IPA (1 mg/mL) for 15' (a) and 30' (b)

Moreover the SEM images (**Figure 2.34**) show that the PbI_2 layer is not present around the crystals: this is probably due to the dissolution or detachment of the material in the dipping solution and to the fact that to obtain so big crystals it is necessary to have enough lead precursor to convert in halide perovskite material: this "excess" of PbI_2 maybe comes from the closest crystal area.

The LP-VASP is then exploited to have a full conversion of the layer. The grains keep the dimensions and the cubic shape (**Figure 2.35**), confirming the good quality of the

process, which allows changing the composition and the phase of the halide perovskite material, without altering substantially the morphology. On the left it is possible to appreciate the crystal shape after the dipping (**Figure 2.35a**) and after both the dipping and the LP-VASP (**Figure 2.35b**).

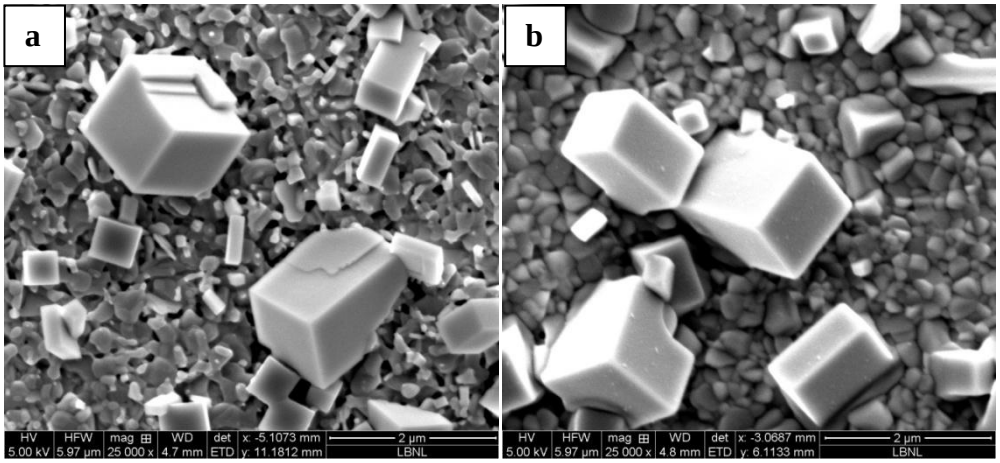

Figure 2.35: Cubic Perovskite crystals obtained a) after 5' dipping in MABr/IPA (1 mg/mL) and b) then converted in with LP-VASP.

From the XRD spectra comes the confirmation of the conversion due to the LP-VASP process (**Figure 2.36**).

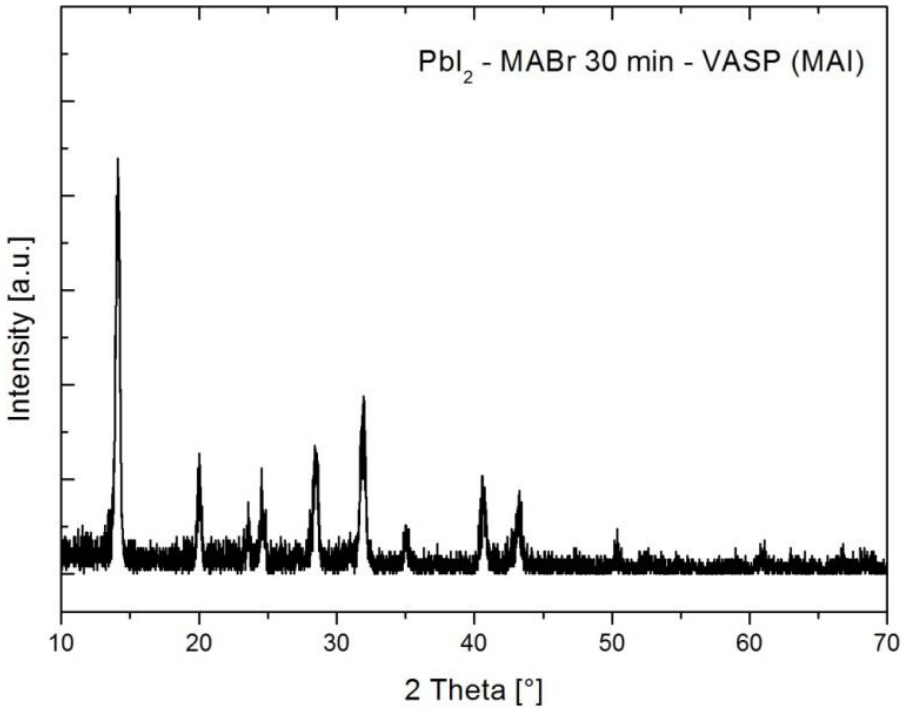

Figure 2.36: XRD of $MAPbI_{3-x}Br_x$ big crystals after 30' of dipping.

2.4. Conclusions

The described method allows to deposit a layer of cubic-like $CH_3NH_3PbI_{3-x}Br_x$ perovskite crystals.

The dipping step, responsible for the growth of the cubic crystals, was optimized to control the dimensions and the shape of the grains. The MABr/IPA solution resulted more suitable to obtain the desired cubic-like crystals than the analogue with MAI. Several dipping times were explored as well as the multi-dipping approach to solve the issue of the partial conversion of the lead iodide precursor in the halide perovskite.

The full conversion is then achieved integrating the LP-VASP to the protocol: this last step allows to convert all the residual PbI_2 after the dipping step while halide perovskite grains retain the characteristic cubic shape.

The concentration of the MABr/IPA is successfully varied to obtain bigger crystals and again the LP-VASP showed to be a powerful tool to obtain complete conversion.

In the next page it is reported a table with all the experiments carried out and a schematic evaluation of the achieved requirements/properties.

Process	Dipping time	Crystal Shape	Facets Exposure	Dimensions	Edges Quality	PbI_2 Conversion
MAI/IPA (8 mg/mL)	30”	Poly-faceted	Exposed	~ 1 µm	Smooth	NO
	60”	Poly-faceted	Exposed	~ 1 µm	Smooth	NO
	90”	No shape	Exposed	< 1 µm	No facets	NO
MABr/IPA (5 mg/mL)	30”	Cubic-like	Not exposed	~ 1 µm	Sharp	NO
	60”	Cubic-like	Exposed	~ 1 µm	Sharp	NO
	180”	Cubic-like	Half-exposed	0.5 ÷ 3 µm	Sharp	NO
	300”	Cubic-like	Exposed	< 1 µm	Smooth	NO
	2 x 60”	Cubic-like	Half-exposed	0.5 ÷ 3 µm	Sharp	NO
	3 x 60”	Cubic-like	Exposed	< 1 µm	Smooth	NO
MABr/IPA (5 mg/mL) LP-VASP (MAI)	60”	Cubic-like	Exposed	~ 1 µm	Sharp	YES
MABr/IPA (5 mg/mL) LP-VASP (MABr)	60”	Cubic-like	Half-exposed	0.5 ÷ 3 µm	Smooth	YES
MABr/IPA (5 mg/mL) LP-VASP (MAI)	30”	Cubic-like	Not exposed	~ 1 µm	Sharp	YES
	60”	Cubic-like	Exposed	~ 1 µm	Sharp	YES
	180”	Cubic-like	Not exposed	0.5 ÷ 3 µm	Sharp	YES
	300”	Cubic-like	Exposed	< 1 µm	Smooth	YES
	2 x 60”	Cubic-like	Exposed	0.5 ÷ 3 µm	No facets	YES
	3 x 60”	Cubic-like	Exposed	0.5 ÷ 3 µm	No facets	YES
MABr/IPA (3 mg/mL)	180”	Cubic-like	Half-exposed	~ 1 µm	Sharp	NO
	300”	Cubic-like	Exposed	< 1 µm	Sharp	NO
MABr/IPA (1 mg/mL) LP-VASP (MAI)	5’	Cubic-like	Isolated grains	~ 1.5 µm	Sharp	YES
	15’	Cubic-like	Isolated grains	~ 2 µm	Sharp	YES
	30’	Cubic-like	Isolated grains	~ 3 µm	Sharp	YES

- Meet the expected requirements
- Slightly different from the expected requirements
- Do not meet the expected requirements

2.5. Reference

1. Leblebici, S. Y. *et al.* Facet-dependent photovoltaic efficiency variations in single grains of hybrid halide perovskite. *Nat. Energy* **1,** 16093 (2016).
2. Li, Y. *et al.* Fabrication of planar heterojunction perovskite solar cells by controlled low-pressure vapor annealing. *J. Phys. Chem. Lett.* **6,** 493–499 (2015).
3. Sutter-Fella, C. M. *et al.* High Photoluminescence Quantum Yield in Band Gap Tunable Bromide Containing Mixed Halide Perovskites. *Nano Lett.* **16,** 800–806 (2016).
4. Li, Y. *et al.* Defective TiO2 with high photoconductive gain for efficient and stable planar heterojunction perovskite solar cells. *Nat. Commun.* **2,** 1–18 (2016).
5. Stranks, S. D. & Snaith, H. J. Metal-halide perovskites for photovoltaic and light-emitting devices. *Nat. Nanotechnol.* **10,** 391–402 (2015).
6. Saliba, M. *et al.* Cesium-containing triple cation perovskite solar cells: improved stability, reproducibility and high efficiency. *Energy Environ. Sci.* **9,** 1989–1997 (2016).
7. Yella, A., Heiniger, L. P., Gao, P., Nazeeruddin, M. K. & Grätzel, M. Nanocrystalline rutile electron extraction layer enables low-temperature solution processed perovskite photovoltaics with 13.7% efficiency. *Nano Lett.* **14,** 2591–2596 (2014).
8. Leong, W. L. *et al.* Identifying Fundamental Limitations in Halide Perovskite Solar Cells. *Adv. Mater.* n/a-n/a (2016). doi:10.1002/adma.201505480
9. Burschka, J. *et al.* Sequential deposition as a route to high-performance perovskite-sensitized solar cells. *Nature* **499,** 316–9 (2013).
10. Liu, D. & Kelly, T. L. Perovskite solar cells with a planar heterojunction structure prepared using room-temperature solution processing techniques. *Nat. Photonics* **8,** 133–138 (2013).

3. Solar Cell Fabrication

This chapter provides an in depth characterization of the macroscopic photovoltaics characteristics of the devices fabricated from organo-lead halide perovskite active layers following the procedures reported in chapter 2, namely low pressure vapor assisted solution process (LP-VASP), sequential dipping, and the combination of the dipping and LP-VASP steps. In addition, the photoluminescence characterization of these active layers, and PhotoConductive – Atomic Force Microscopy (PC-AFM) measurements are reported.

3.1. Design and Fabrication of a Solar Cell

As mentioned in Chapter 1 the solar cells fabricated herein has a n-i-p planar structure (**Figure 3.1**). In particular they are composed by the glass substrate, the fluorine doped tin oxide (FTO) as the cathode, compact-TiO_2 as ETM, $CH_3NH_3PbX_3$ as the photoactive material, Spiro-OMeTAD as the HTM and a gold electrode as the anode.

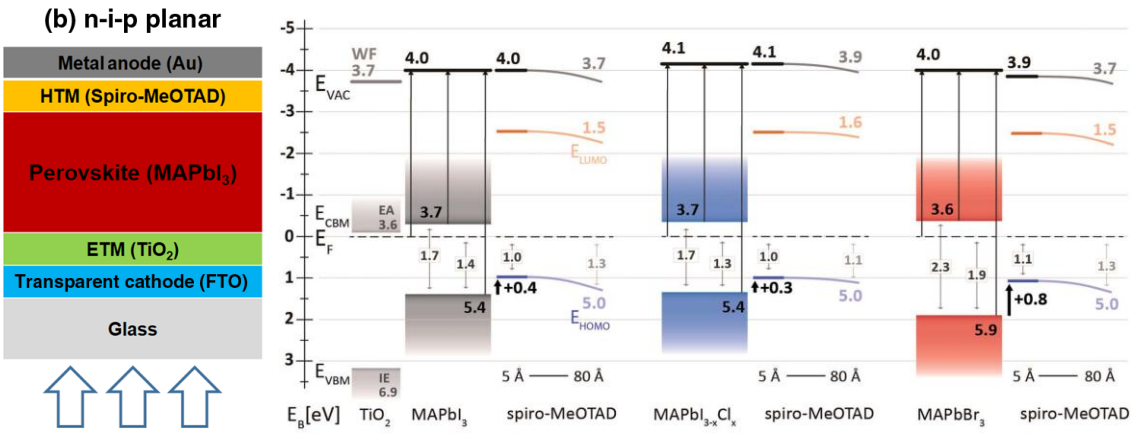

Figure 3.1: n-i-p planar configuration.[1] and experimentally determined energy level diagrams of interfaces between spiro-MeOTAD and MAPbX (X = I_3, $I_{3-x}Cl_x$, Br_3) films on TiO_2.[2]

Some theoretical and practical factors should be taken into account when the solar cell is fabricated. First of all a suitable band alignment between the materials is necessary to generate a good electron extraction from the photoactive layer to the external load. Moreover the candidate materials have to show compatible deposition techniques with the substrate and the layers already deposited. In the end an inert chemical behavior is appreciated in order to avoid side reactions between the materials leading to the degradation of the whole system and affecting the final efficiency. In the next paragraphs the depositions of the non photoactive transporting layers are reported.

3.1.1. Transparent-Conductive Substrate - FTO Electrode

The electrode in a n-i-p configuration acts as photoanode: FTO is usually deposited either by sputtering or spray-pyrolysis on the glass substrate. As this is a common material, in most of the cases the glass with transparent electrode is obtained commercially. At the LBNL the glass/FTO substrates were purchased already cut (16 x 14 mm^2) and patterned (with geometry needed for the device fabrication). At the IOM-CNR the glass/FTO substrates were purchased in large pieces so they were cut (with laser cutter) and patterned with an etching process. In particular the latter consists in the chemical etching of the FTO using Zn powder and a solution of HCl (2M).

The FTO substrate does not absorb visible light (transmittance usually around 85%) so the radiation pass through it before reaching the photoactive material. Moreover the layer is characterized by conductive properties due to a low surface resistivity (in the range of 7-15 Ω/sq).

3.1.2. TiO_2 Electron Transporting Material

Before the deposition of the compact titania layer (c-TiO_2) the substrate is cleaned with soap-water solution, acetone and isopropyl alcohol (IPA) in ultrasonic bath for 10'. To deposit the ETM it is possible to use different techniques, in particular during this project the film was deposited by two different methods: at the IOM-CNR labs by spin coating a sol-gel solution, while at the LBNL physical vapor deposition in an electron beam evaporator.

In the former case the solution contains a Ti(IV)-organic precursor and it is spin coated onto the glass/FTO substrate: changing the spin coating parameters (acceleration, speed, duration,…) it is possible to control the thickness and the uniformity of the layer. After this step (which might be repeated for thicker films), the sample is annealed at 500°C for a couple of hours to obtain TiO_2 in the anatase phase. In the latter case the clean sample is loaded into the evaporator chamber and TiO_2 pellets are used as source. The film quality depends on a few process parameters, such as the deposition rate, and substrate temperature. In the specific case low deposition rate (0.5 Å/s) and sample temperature at 350°C were maintained during the deposition process.

Moreover the c-TiO_2 deposited with this setup showed the incorporation of deep-level hole traps producing a photoconductive gain under ultraviolet exposure. As reported by Li et al[3] this phenomenon is responsible for an increase of the electron extraction from the photoactive material reducing the hysteresis of the SC and improving the overall efficiency.

Beside these techniques, in the other laboratories TiO_2 is also deposited by sputtering, thermal evaporation or spray-pyrolysis.

3.1.3. Spiro-OMeTAD Hole Transporting Material

After the halide perovskite layer the HTM is deposited: Spiro-OMeTAD is an organic small molecule with a suitable electronic structure acting as filter allowing the holes flow and blocking the electrons. This compound was successfully used in the last decades as p-type material. It is deposited immediately after the organo-lead halide perovskite film to limit the exposure of the photoactive material to the air: it was noticed that the HTM layer has the capability to somehow preserve the underlying layers from the humidity. Once the Spiro-OMeTAD is deposited onto the halide perovskite film it is usually kept in air (overnight) to dope the HTM with oxygen, resulting in increased film conductivity.

The Spiro-OMeTAD is deposited by spin coating from a solution in an organic solvent (chlorobenzene) containing as additive a doping agent (lithium bis(trifluoromethanesulfonyl)imide and 4-tert-butylpyridine).

Since Spiro-OMeTAD is quite expensive and shows issues concerning long term stability, other n-type semiconductors are under study. One of the main issues when the materials are under investigation is the compatibility of the deposition technique with the organo-lead halide perovskite material: it is important to find a semiconductor not requiring a method that can damage the photoactive material.

For this reason also the inverted architecture is studied offering the possibility of fabricating devices with the inverted architecture, i.e. depositing first the p-type layer and then the halide perovskite.

3.1.4. Gold Counter Electrode

To complete the device a metallic film, that collects the charges and convoys them to the external circuit, is finally deposited onto the HTM: in particular gold can be evaporated in a thermal or e-gun evaporator. To define the active area of the SC (all the layers composing the stack) usually gold is deposited using a metal stencil mask (**Figure 3.2**).

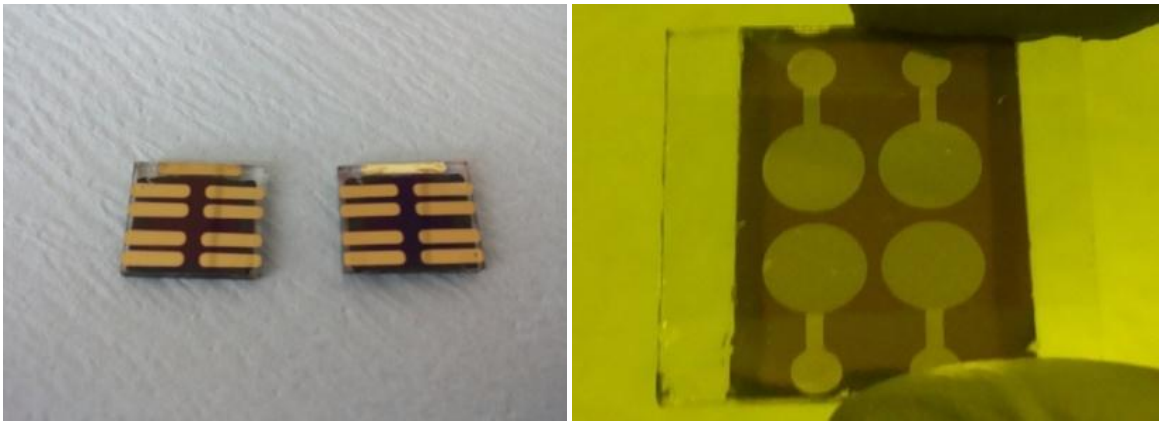

Figure 3.2: p-SC after Au evaporation using different masks: the SC fabricated at the LBNL (left) and at the IOM-CNR (right).

3.1.5. The final device

As previously mentioned the final device is composed by glass, FTO (transparent electrode), c-TiO_2 (ETM), $CH_3NH_3PbI_3$, Spiro-OMeTAD (HTM) and gold as counter electrode. These layers appear very clearly in a cross section SEM image (**Figure 3.3**):

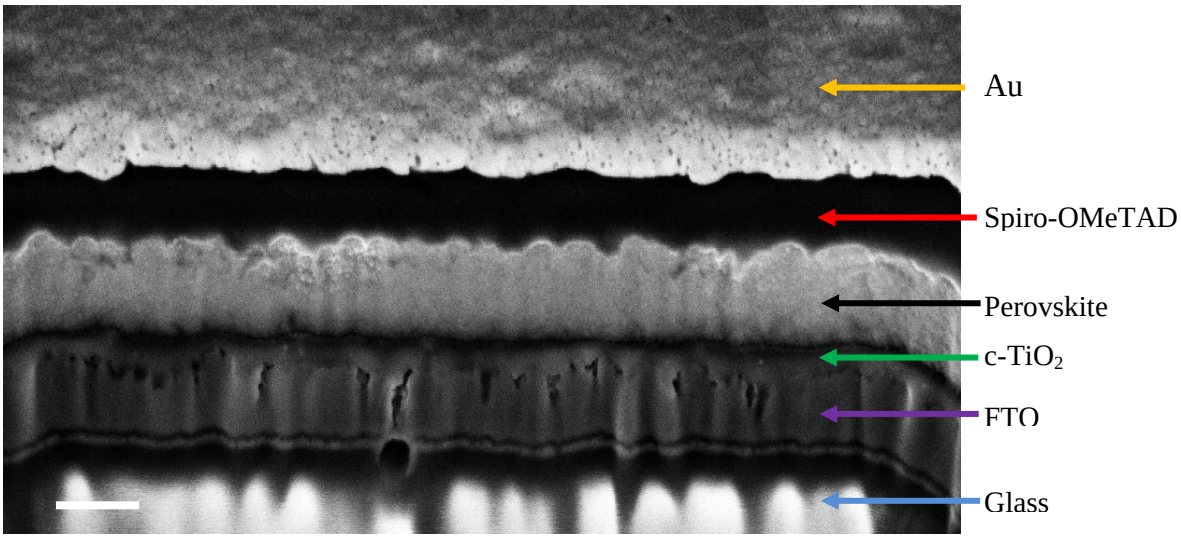

Figure 3.3: SEM image of a flat p-SC. The scale bar is 200 nm.

3.2. Efficiency of the Fabricated Devices

Besides the many techniques usually used to characterize each layer including XRD, UV-vis spectroscopy, SEM, EDX, XPS, UPS, AFM and so on, it is very important to evaluate the performances of the devices, in particular their efficiency. The SC efficiency (η) also called photon-to-current conversion efficiency (PCE) defines the device capability to convert the sun energy into electrical energy (see Chapter 1).

The solar cells are introduced under the sun simulator and the electrodes (FTO and Au) are connected to the J-V characterization system. Applying a voltage to the sample and sweeping it within a suited voltage range (from 0 V to 1.2 V typically for a p-SC) one can record the corresponding generated current density (J). If the scan is performed in dark condition then what is characterized is the n-i-p junction of the diode (J_{dark}). This kind of characterization is useful to understand the quality of the device, and in particular the contribution of the parasitic resistance. If the measurement is done under illumination what is characterized is the behavior of the solar cell under working condition.

As reported in Chapter 1 the organo-lead halide perovskite material is subjected to the anomalous behavior called hysteresis that is evidenced recording the *JV* curve. For this reason the efficiency spectra are recorded in both the bias directions (forward and reverse). Moreover the devices have an active area of 0.065 cm^2 and before the *JV* measurement are exposed under the light for 20' (light soaking).

In the next sections, the efficiency evaluations of the halide perovskite solar cells deposited *via* LP-VASP, sequential dipping (cubic crystals) and the combination of dipping and LP-VASP (see Chapter 2) are reported.

3.2.1. Efficiency of the p-SC with LP-VASP

The p-SC fabricated exploiting the LP-VASP to deposit the halide perovskite layer has shown relatively high efficiencies. To reach these results all the aspects concerning the device fabrication and characterization (sample designing, deposition techniques and the sun simulator setup) were optimized. I had the opportunity to learn how to critically evaluate the obtained data, to slightly improve some tricky steps and finally to enhance the overall PCE. Below, I show a few representative *JV* curves that highlight the progress I made in solar cell fabrication leading to relatively high efficiencies.

Here I report the *JV* curve (**Figure 3.4**) of one of the best p-SC with planar $CH_3NH_3PbI_3$. The improved fabrication skills allowed me to be as precise as possible during the several steps leading to the final device.

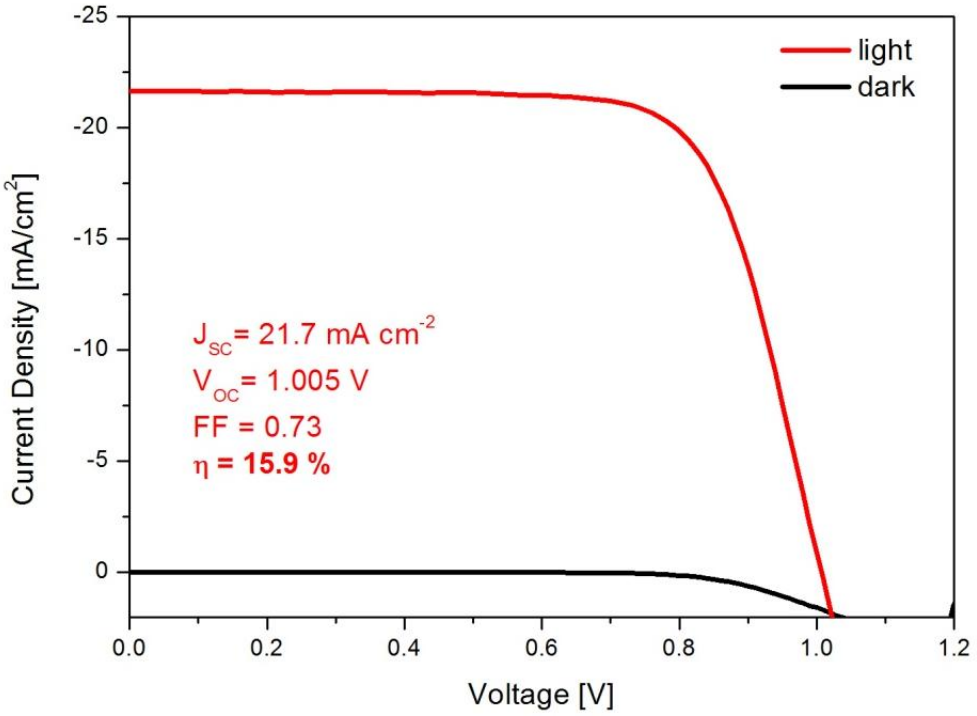

Figure 3.4: JV curve for an optimized p-SC based on $CH_3NH_3PbI_3$ deposited with LP-VASP.

Qualitatively it is possible to appreciate the high performance of the device taking in consideration the J_{SC}, the V_{OC} and the *FF*. The overall efficiency measured with the

reverse scan direction is close to the 16%. In the following *JC* graph (**Figure 3.5**) the curves obtained with forward and the reverse bias are reported: the hysteresis in this case is very low, proving the good quality of the methylammonium lead iodide perovskite layer and of the overall device.

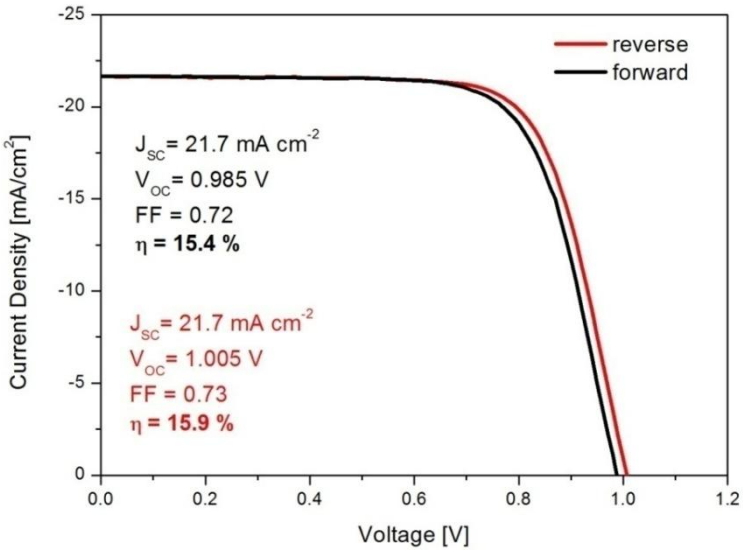

Figure 3.5: JV curve in forward and reverse bias of optimized p-SC based on $CH_3NH_3PbI_3$ LP-VASP deposited.

3.2.2. Efficiency of the p-SC with Cubic Morphology

I fabricated the complete device with the cubic crystal $CH_3NH_3PbBr_{3-x}I_x$ perovskite. The morphology reported in Chapter 2 is obtained dipping the PbI_2 layer in MABr/IPA solution. The amount of unconverted lead precursor after the dipping step is still high, moreover the morphology shows non uniform coverage.

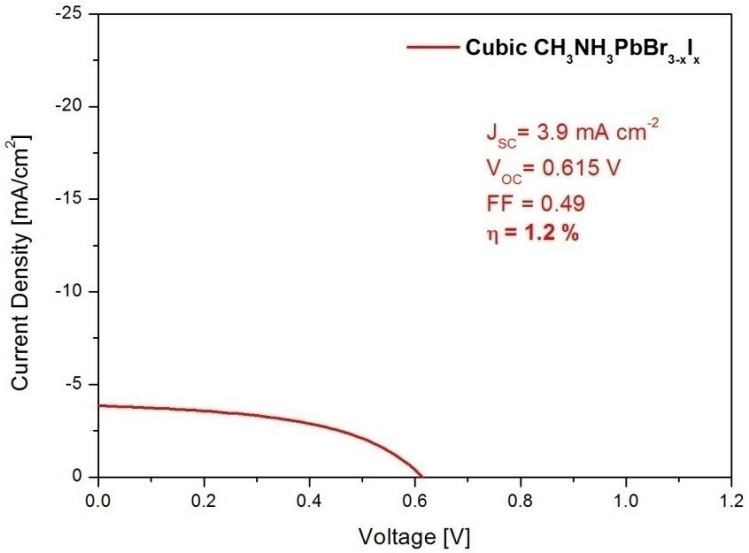

Figure 3.6: JV curve of p-SC with cubic-like crystal morphology

From the *JV* curve (**Figure 3.6**), it is possible to see a poor conversion efficiency due to low photo-generated current, low V_{OC} and bad *FF*. The device is characterized by both the high R_S and the low R_{SH}. The not homogeneous coverage of the cubic halide perovskite layer is responsible for the presence of pinholes which causes high recombination rate: this is detrimental for the solar cell since both the V_{OC} and the J_{SC} decrease.[4] Even if in this it is not the main reason, it is important to remind that the band gap in rich bromine perovksite is around 2.3 eV (most likely) so higher V_{OC} and lower J_{SC} are expected compared to the pure iodine perovskite.

3.2.3. Efficiency of the p-SC with Cubic Morphology/LP-VASP

The optimization of the $CH_3NH_3PbBr_{3-x}I_x$ cubic-like morphology consists in the combination of the dipping process and the LP-VASP. With this approach (See Chapter 2) I was able to deposit still a cubic-like halide perovskite completely converted after the low pressure vapor assisted solution process ($CH_3NH_3PbI_{3-x}Br_x$). After the synthesis and the elementary characterizations, the relative based SC was fabricated and the efficiency evaluated (**Figure 3.7**).

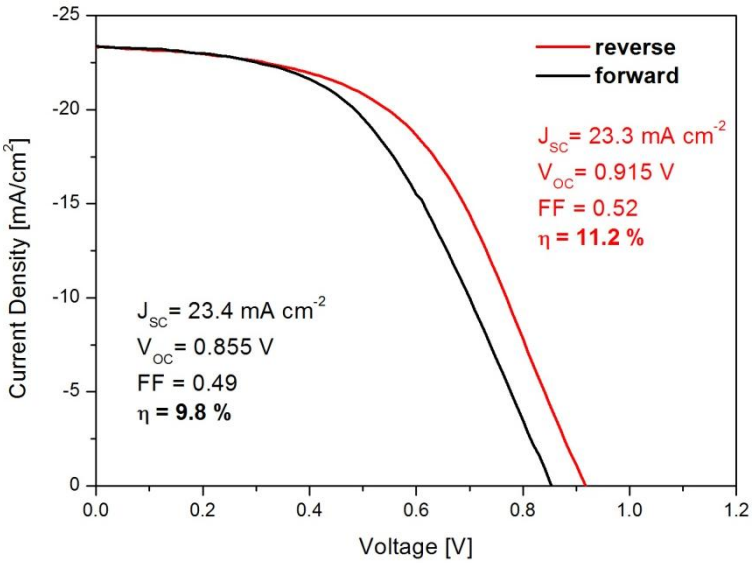

Figure 3.7: JV curve in forward and reverse bias of cubic-like p-SC implemented with LP-VASP.

The efficiencies of this class of devices are higher compared to the cubic like morphology without the LP-VASP conversion. The V_{OC} are slightly lower than the usual (~ 1 V) while the J_{SC} is slightly increased, overcoming 23 mA/cm^{-2}. The *FF* around 50 proves the presence of parasitic resistance: evaluating the curve shape it seems that the R_S gives

the main contribution to the low *FF*. The series resistance is usually high when the quality at the material interfaces is poor: in this case this is consistence with the morphology of the photoactive material. The hysteresis behavior is present as it is possible to observe in **Figure 3.7**: the efficiency of the device is higher than 11% for the reverse bias and around 10% in forward bias. The overall quality of the device might be again negatively affected by the presence of pinholes due to a non continuous photoactive layer.

Although with this method a control on the morphology is achieved, alternative fabrication processes should be considered to obtain more performant devices.

3.3. Photoluminescence (PL) Characterization

In this section the photoluminescence (PL) spectra and PL map imaging of the deposited halide perovskite layers obtained with: LP-VASP, combination of dipping and LP-VASP, and big crystals are reported. The sample architecture used for this characterization experiment is slightly different from the one used in a SC. In particular, the organo-lead halide perovskite is deposited onto the bare glass substrate to avoid the quenching of the PL signal: TiO_2 as the electron selective contact can extract electrons from the absorbing material preventing the radiative recombination process that generates the PL signal. Around 30 nm of PMMA are deposited by spin coating on top of the halide perovskite to partially seal the surface to prevent the degradation during the measurements. For the PL measurement, the perovskite sample is exposed to a laser excitation source with energy larger than the band gap of the absorber. The material absorbs the photons which results in the formation of electron-hole pairs. Depending on the properties of the material, the free electrons and holes eventually recombine, either non-radiative, or radiative (PL) under open-circuit condition. The PL characterization gives an indication on the quality of the semiconductor.

The radiative recombination (band-to-band) mechanism is the recombination of an electron and a hole with the consequent emission of a photon with energy equal (or close) to the E_g (working principle of a light emitting diode (LED)). In particular, radiative recombination is the only recombination mechanism in a defect-free, ideal direct band gap semiconductor. On the other side in non-radiative recombination (Shockley-Read-Hall (SRH) and Auger) processes the absorbed energy dissipates via phonons. SRH recombination is defect mediated while Auger recombination involves a third charge carrier and is predominant at high charge carrier concentration. Any non-radiative process reduces the PL signal, thus the only recombination mechanism should be radiative as a measure for high material quality.

3.3.1. Perovskite LP-VASP

The LP-VASP perovskite is further investigated through steady state PL characterization and PL imaging.

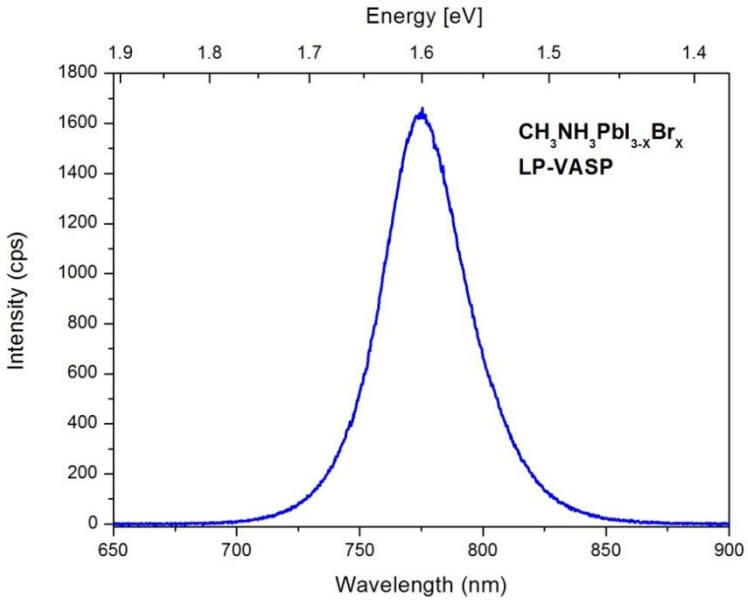

Figure 3.8: Steady state PL on a random spot of the $CH_3NH_3PbI_{3-x}Br_x$ LP-VASP layer.

From the PL spectrum shown in **Figure 3.8** it is possible to extract the band gap at the peak position centered at a wavelength λ = 774 nm corresponding to a band gap E_g = 1.60 eV. This value is the same reported in literature (1.60 eV) and in good agreement with the band gap E_g = 1.59 eV extracted with the Tauc plot analysis (see Chapter 2).

To evaluate the uniformity of the sample the PL was measured on five different spots and the spectra are reported below (**Figure 3.9**).

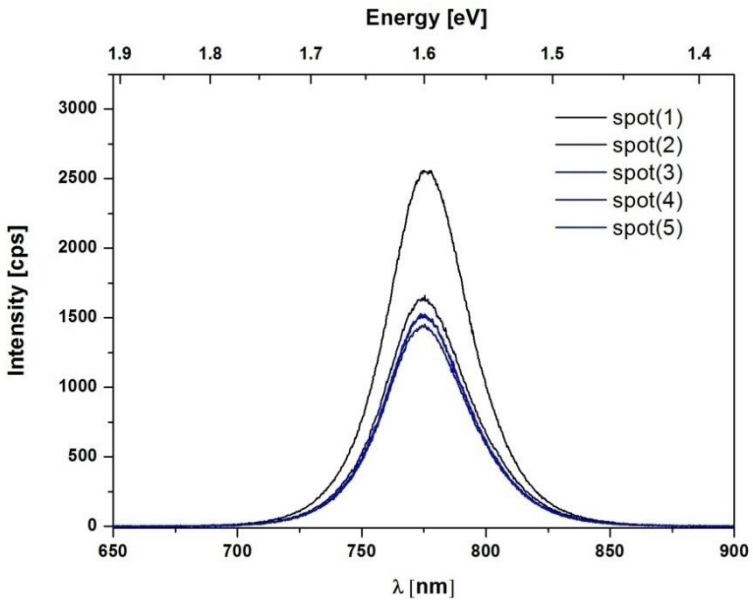

Figure 3.9: Steady state PL on 5 spots of the $CH_3NH_3PbI_{3-x}Br_x$ LP-VASP layer.

Plotting together the PL spectra of the five random spots it is possible to appreciate that the peak positions do not shift indicating high compositional uniformity.

It is also possible to observe the variation of the PL intensity as function of the time (**Figure 3.10**): for this measurement the sample was continuously exposed to the light source for prolonged time and every ten seconds the PL signal is collected.

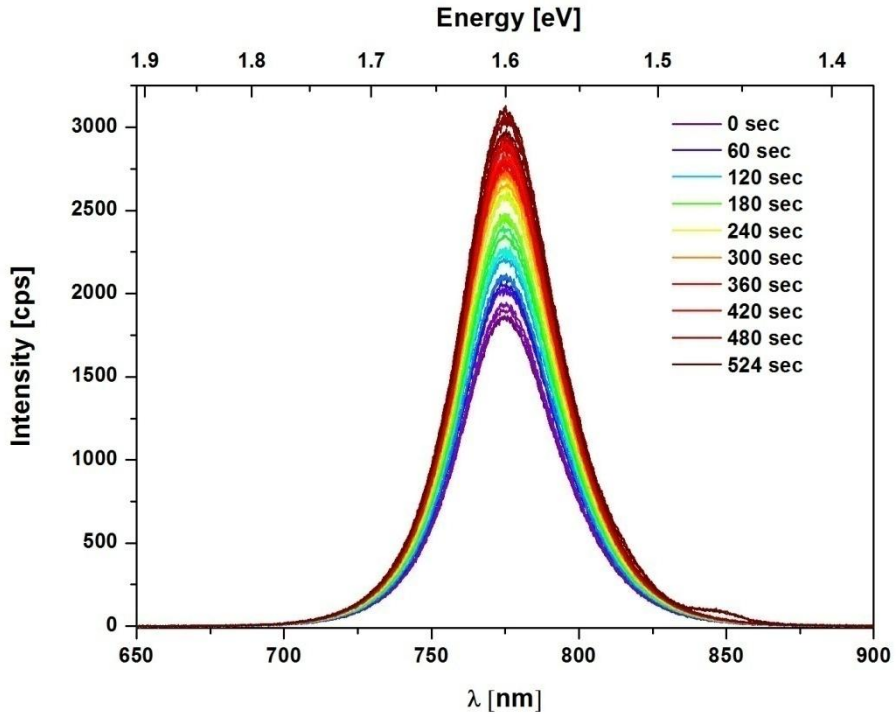

Figure 3.10: Steady state PL of the $CH_3NH_3PbI_{3-x}Br_x$ LP-VASP layer measured repeatedly on the same spot over a time window of 524 s.

Figure 3.10 illustrates a slow increase in PL intensity over time. This trend has been observed before[5] and can be correlated to improved optoelectronic properties due to higher radiative recombination. One possible explanation is the slow decomposition of the $CH_3NH_3PbI_{3-x}Br_x$film due to irradiation damage. The decomposition will lead to the formation of PbI_2 phase due to the evaporation of volatile CH_3NH_3I. It has been reported previously, that presence of small amounts of PbI2 can passivate defects in $CH_3NH_3PbI_{3-x}Br_x$. Beside the controversial hypothesis (PbI_2 should increase the degradation rate of the perovskite)[6] it seems that a small excess amount of PbI_2 mainly present at the grain boundaries reduces the non-radiative recombination rate.[7–10] A second explanation for the increase in PL over time is the slow filling of traps in the band gap, that is deactivation of traps, thus increase in radiative recombination rate.[5]

The PL imaging can provide further insights in layer homogeneity on a larger scale. In particular the average PL intensity calculated for the LP-VASP sample on an area of ~ 30 µm x 30 µm (**Figure 3.11**) is 1552 ± 177 cps corresponding to a standard deviation of **11 %**. This value indicates small PL variations over the sample that might be translated in good optoelectronic uniformity. Moreover the data is in good agreement with the value reported by Sutter-Fella et al.[11]

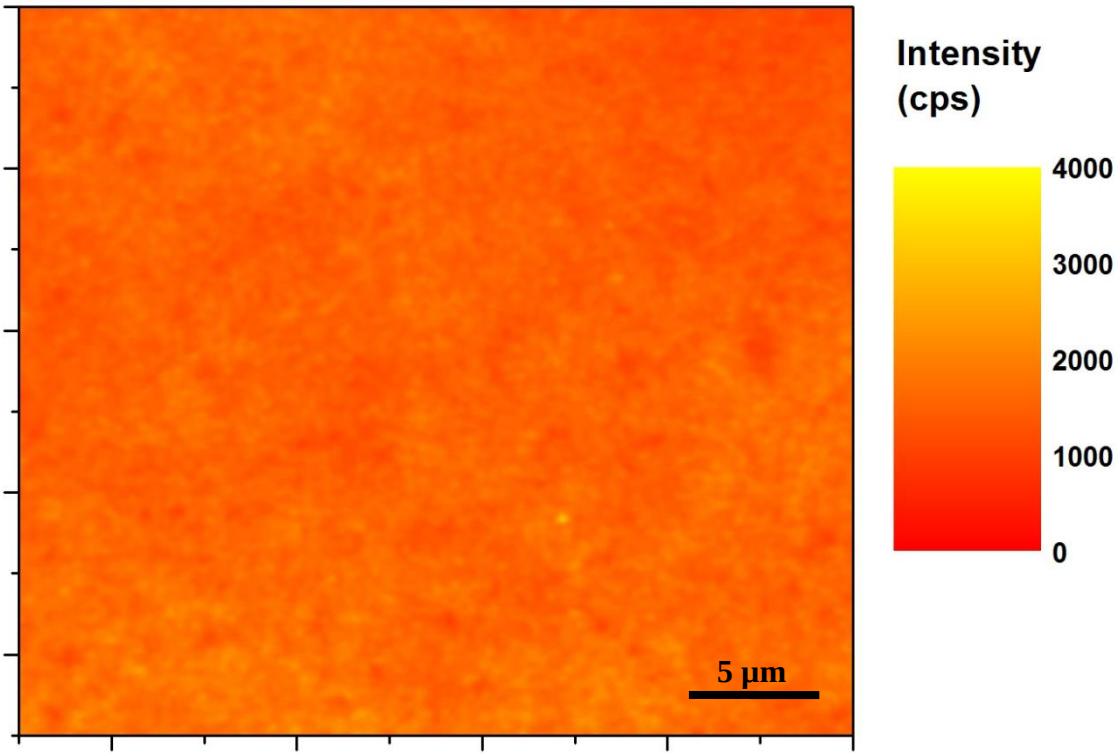

Figure 3.11: PL image of the perovskite deposited *via*LP-VASP

3.3.2. Perovskite Sequential Dipping and LP-VASP

Also for this kind of sample, obtained combining the dipping step with the LP-VASP, the PL characterization resulted interesting (**Figure 3.12**). Again the band gap extracted (1.59 eV) is in good agreement with the value obtained from the UV-vis spectroscopy (Tauc plot analysis E_g = 1.58 eV) and is equal to the band gap of the normal LP-VASP indicating the same $CH_3NH_3PbI_{3-x}Br_x$ chemical composition. This is a remarkable aspect since, before the LP-VASP conversion, the substrate is a highly bromine rich perovskite $CH_3NH_3PbBr_{3-x}I_x$, due to the dipping of the lead precursor in the MABr/IPA solution. The LP-VASP step leads to a full conversion and an almost complete halide substitution of Br^- with I^-. Moreover there is no peak shift indicating that the halide substitution is highly

homogeneous over the sample i.e. there is no bromine variation in the composition along the layer.

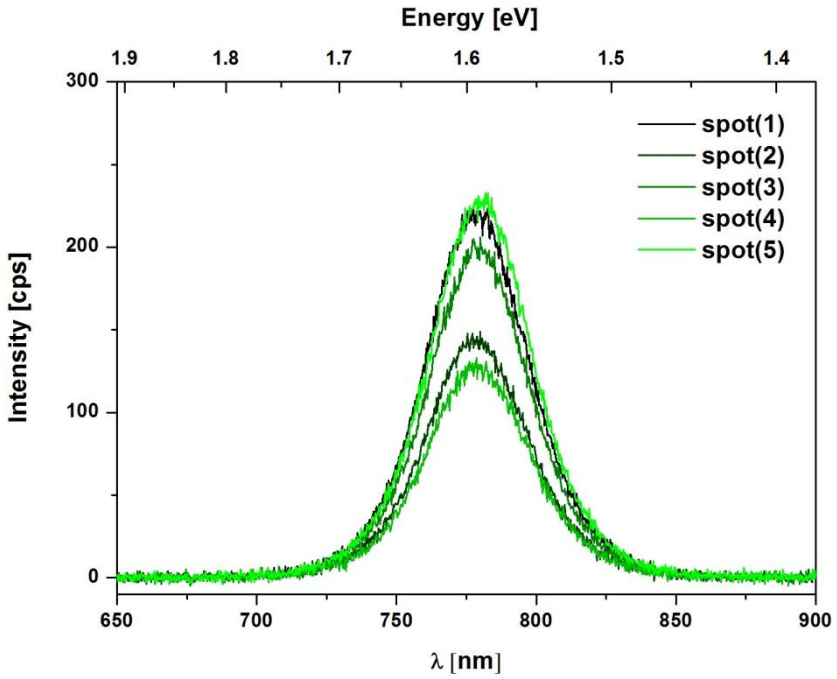

Figure 3.12: Steady state PL on 5 spots of the $CH_3NH_3PbI_{3-x}Br_x$ dipping/LP-VASP layer

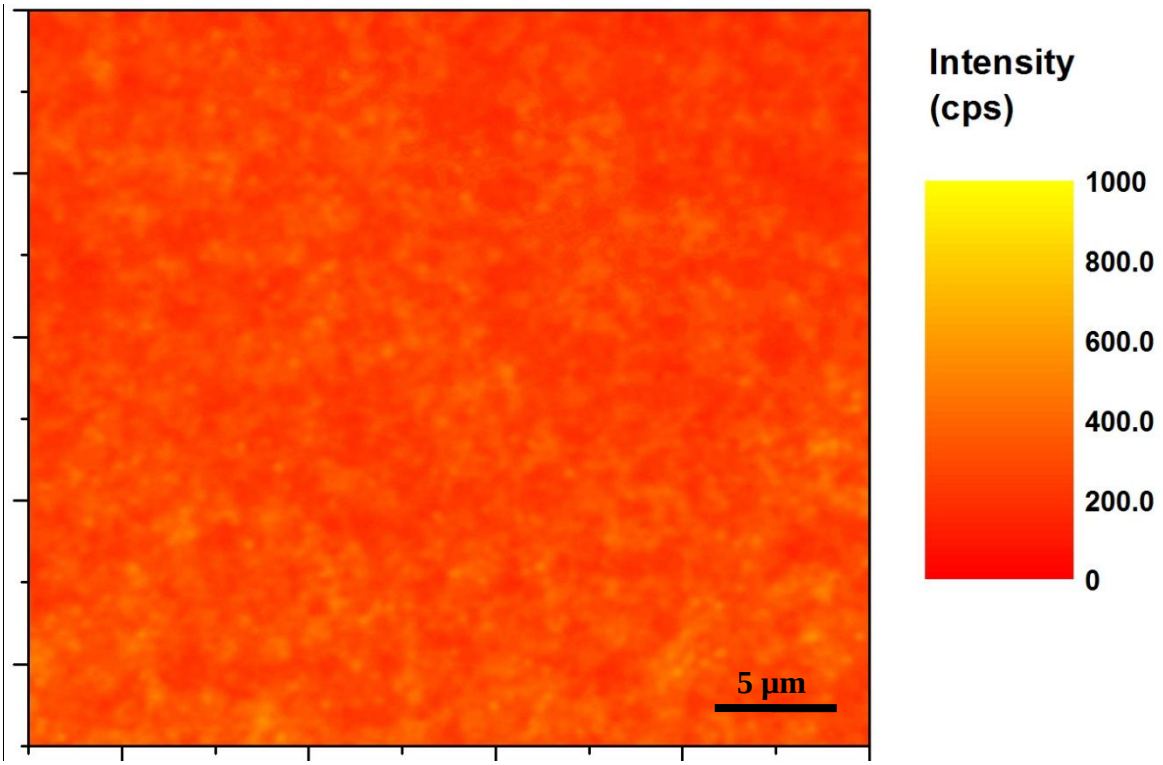

Figure 3.13: PL map image of the cubic-perovskite deposited *via*dipping/LP-VASP

Also for this sample it was possible to record the PL map and evaluate the homogeneity of the surface: again the average PL intensity calculated for the sequential

dipping/LP-VASP sample on an area of ~ 30 µm x 30 µm (**Figure 3.13**) is 274 ± 53 cps corresponding to a standard deviation of **20%**, almost double than the previous sample.

3.3.3. Big crystals

The photoluminescence characterization for this particular substrate composed by big perovskite crystals (dimensions around 2 - 3 µm) brings interesting results. The steady state measurement was carried out by pointing the laser source (diameter of the spot ~ 3µm) onto a single crystals with the help of an optical microscope (**Figure 3.14**).

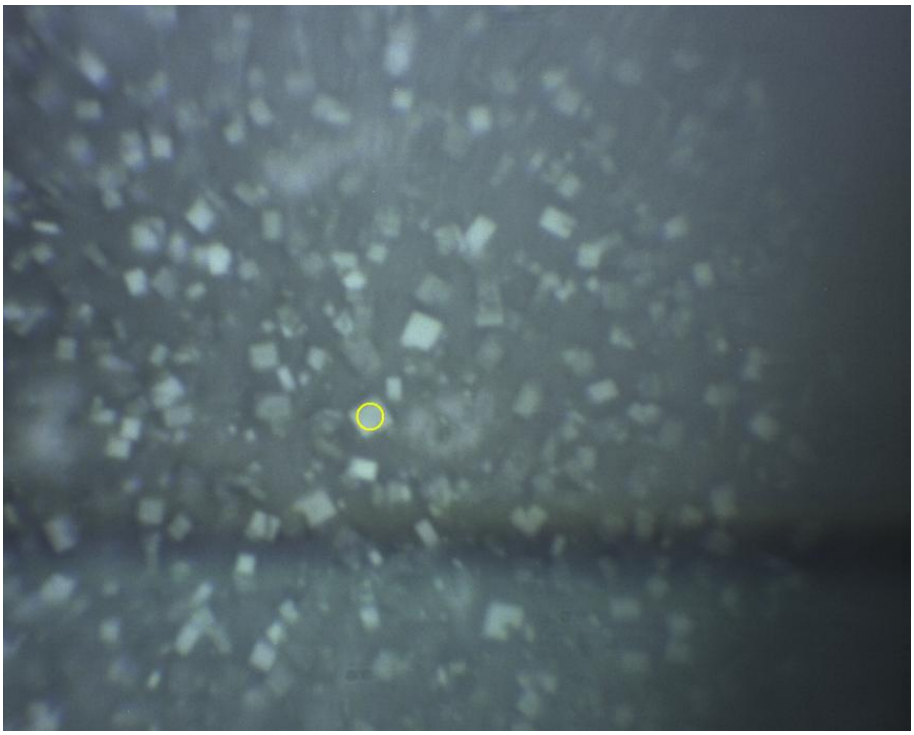

Figure 3.14: Big Crystal morphology recorded with an optical microscope with 80X objective.

Five PL spectra were recorded on different crystals present on the substrate. The collected spectra are plotted together in **Figure 3.15**. The PL spectra show a higher variation in intensity than observed before in the VASP sample. Additionally, the spectra show a shift of the peak position by ~ 15 nm. The shift of peak position indicates a variation in chemical composition with some cubes containing more Br (shift to smaller wavelength). The composition variation might be due to the fact that the time conversion (2 h) with the LP-VASP is not enough to have an homogeneous Br^- substitution with I^-.

A probable reason for the PL intensity fluctuation could be a small sample drift during the measurement which leads to less material that is probed by the excitation beam.

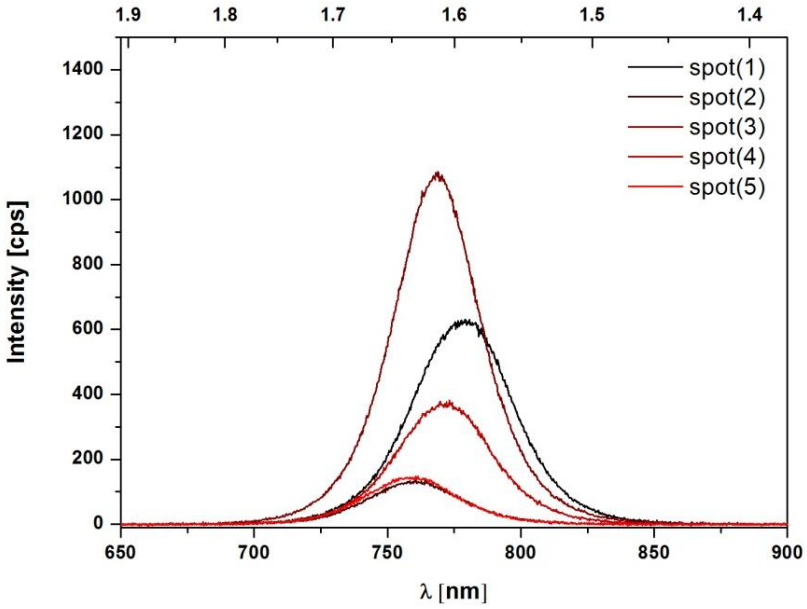

Figure 3.15:Steady state PL on 5 big crystals of the $CH_3NH_3PbI_{3-x}Br_x$ long dipping/LP-VASP layer.

The PL map provides further insights in the intensity distribution with respect to crystal morphology. The image in **Figure 3.16a** obtained with an optical microscope (objective 100x) depicts a large crystal size distribution over the sample with crystals from 200 nm to 3 µm (confirmed by the SEM images reported in Chapter 2, **Figure 2.34b**). The wide size distribution is reflected in the PL image (**Figure 3.16b**). Surprisingly, the bright spots (high PL intensity, yellow and white circles) are dominated by small crystallites and not the big square crystals. In the PL map it is possible to recognize a well defined cubic crystal (black squares) with low signal intensity. The dark blue regions in the figure are due to the bare glass where no perovskite is present at all.

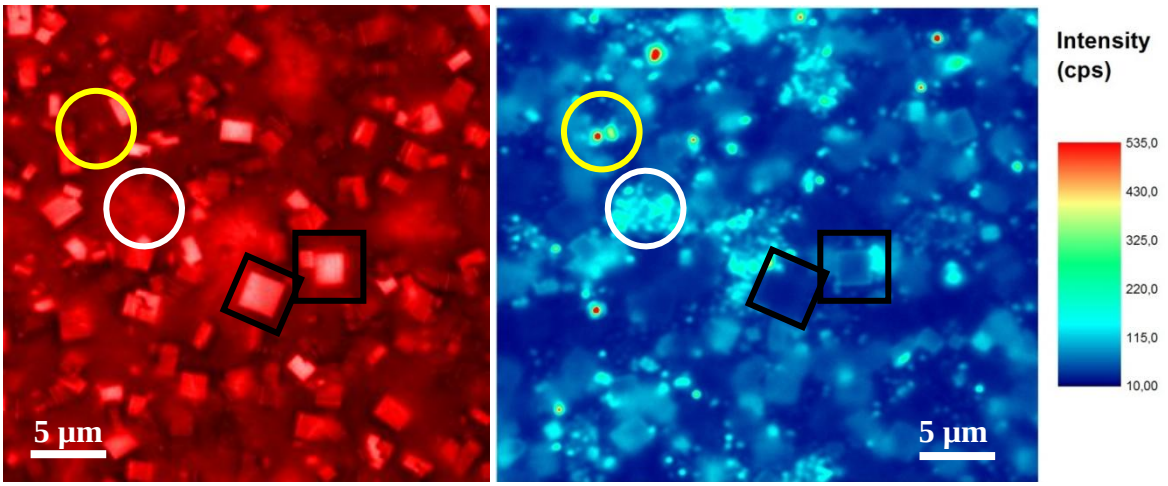

Figure 3.16: a) Optical microscope image of $CH_3NH_3PbI_{3-x}Br_x$ big crystals deposited *via* long dipping/LP-VASP method and b) PL map image.

It would be interesting to analyze the difference in PL emission with respect to crystal size. This might be investigated by synthesizing two different sets of samples with the same chemical composition: large crystals (larger than the laser beam diameter) and very small crystallites.

3.4. PhotoConductive – Atomic Force Microscopy

These measurements were done in collaboration with Dr. Ravi Chandra Chintala under the supervision of Dr. Paul Ashby

As introduced in Chapter 2 the photoconductive atomic force microscopy (pc-AFM) technique is used to study the facet-dependence of some photo-induced properties and in particular the photo-generated current. With this technique, it was possible to associate the morphology of the layer with the electrical behavior on the surface.

The setup (**Figure 3.17**) consists in an evolution of an AFM system where the cantilever is connected to a preamplifier which is necessary to measure the current generated from the device and flowing in the circuit: the sample needs to be contacted to form a closed circuit with the pc-AFM.

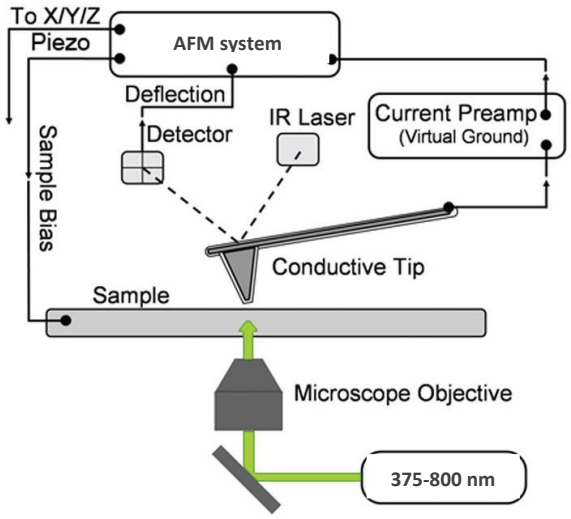

Figure 3.17: Scheme of a typical pc-AFM experimental setup.[12]

To carry out this kind of experiment the sample is a so called “half cell” where the organo-lead halide perovskite is the top material (exposed to the Pt-coated tip) avoiding the use of the HTM (Spiro-OMeTAD) and the top contact (Au). To complete the substrate the photoactive material is deposited onto the other layers usually used to fabricate a n-i-

p device: on the glass/FTO substrate the TiO_2 is evaporated and then covered with the halide perovskite of interest. The so fabricated half device is loaded into the pc-AFM which is equipped with a glove-box filled with a constant flow of N_2.

During the measurement the sample is illuminated from the bottom through the glass/FTO/TiO_2 substrate to generate the carriers into the semiconductor while on the other side the cantilever scans the surface recording both the morphology and the relative current. Instead of the conventional contact mode the scan is performed in PinPoint mode to preserve the tip, the sample and to avoid several artifacts due to the tip oscillation, the material transfer and the change of the tip-sample contact area.[13]

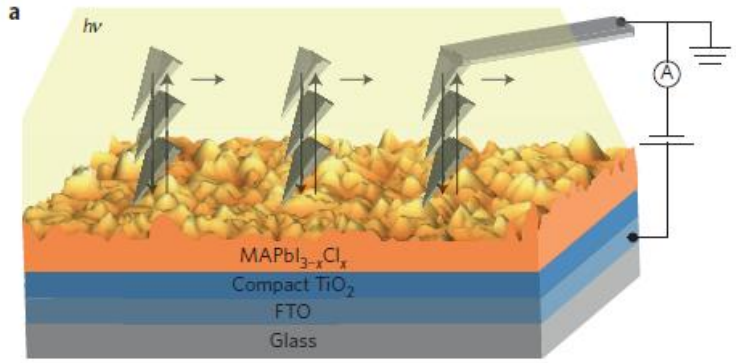

Figure 3.18: Scheme of the investigated device and of the PinPoint mode.[13]

The PinPoint mode consists in the gentle approach of the tip to the surface: the tip touches the material with a certain force, explore the current with a number of cycles at a defined frequency then retract and moves to the next pixel (**Figure 3.18**). The whole surface is so scanned and characterized.

Below there are reported two different samples one with the organo-lead halide perovskite deposited through LP-VASP and the other obtained with the sequential dipping/LP-VASP method leading to the cubic-like $CH_3NH_3PbI_{3-x}Br_x$ previously described (see chapter 2).

3.4.1. High Efficient planar $CH_3NH_3PbI_{3-x}Br_x$ *via* LP-VASP

The fresh sample is loaded into the setup to perform the measurement. The substrate is scanned under illumination and the topography of the surface (**Figure 3.19a**) as well as the short circuit current (**Figure 3.19b**) are acquired and plotter as following:

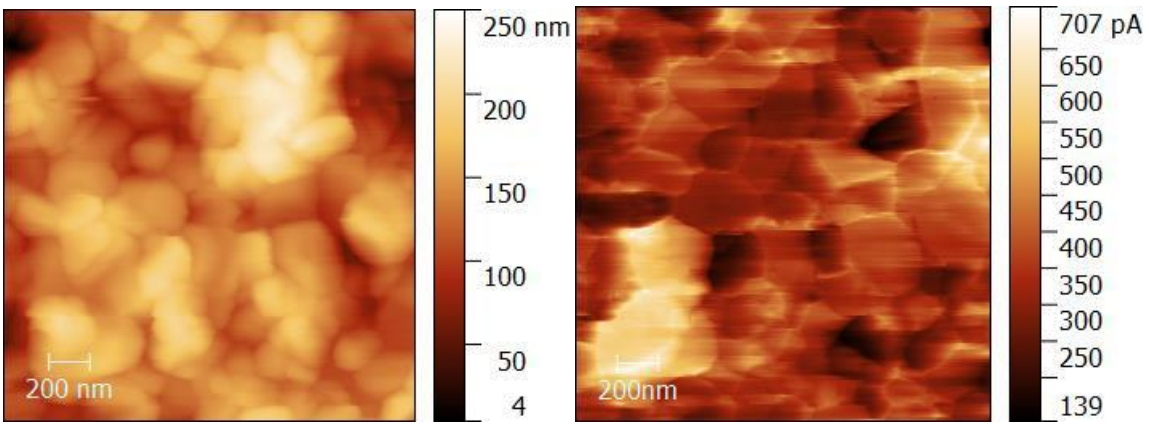

Figure 3.19: (a) On the left the topography of the sample while on the right (b) the short circuit current under illumination.

The magnitude of short circuit current (I_{SC}) reported in **Figure 2.19b** shows values in the order of hundreds of pico-Ampere (pA): Considering the pixel area from which the current is collected (~8 nm per pixel, ~64 nm^2 in the above figure), the current density is considerably high. The high current density indicates that the volume of charge extraction is higher than the contact size of the tip and the sample.

Furthermore, the current map shows inter granular variations in the magnitude of I_{SC} and similar phenomena are also noticed by Kutes et.al.[14] While the inter granular variations are clearly visible in the current map, there is no a direct correlation between the size of the grain and the magnitude of the current. Moreover the intra-grain variations are not present in the map on the right. At the grain boundaries and the grain edges the I_{SC} is usually higher compared to that one measured on the grain. This might be consistent with the high defect tolerance attributed to the high efficient polycrystalline organo-lead halide perovskite.

3.4.2. Cubic-like $CH_3NH_3PbI_{3-x}Br_x$ Crystals (dipping/LP-VASP)

The cubic-like grains are here characterized to see if there is some facet-dependence of the photo-generated current. In particular two samples are reported since covered with grains of different size: small grains (~ 0.5 µm) and medium grains (~ 1 µm). For the synthesis procedure see chapter 2.

3.4.2.1. Medium (~ 1 µm) Cubic-like Crystals

The morphology of the sample is slightly different from the usual flat halide perovskite previously commented. Here it is possible to see the characteristic cubic shape of the grain and appreciate the differences. Although the layer is fully converted into the desired semiconducting material no photocurrent is detected. For this reason a forward bias of -1.5 V is applied to the system. Also applying the voltage the extracted current is still low.

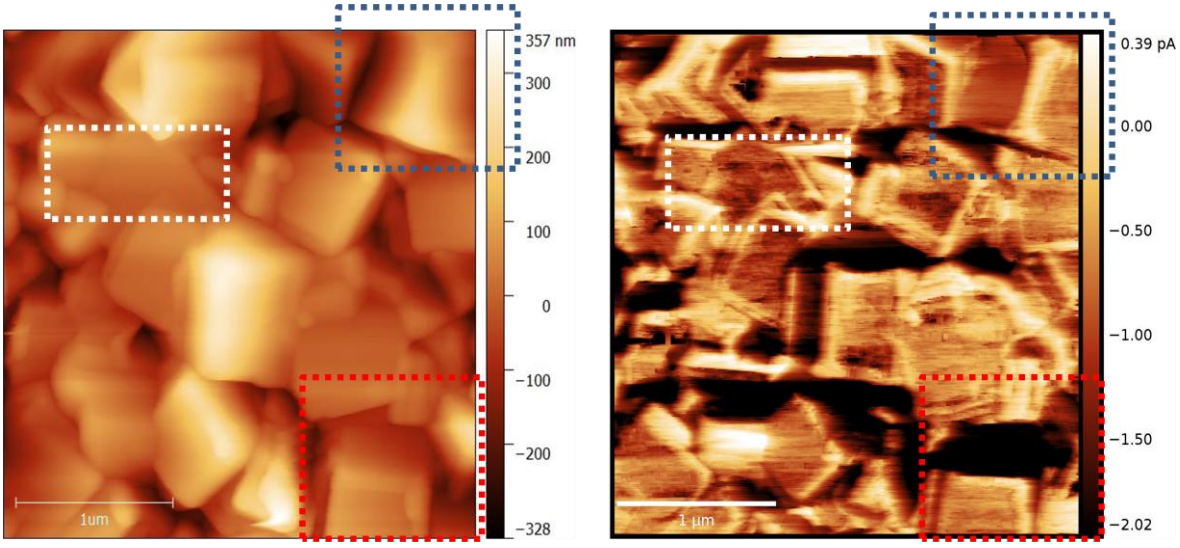

Figure 3.20: (a) On the left the topography of the sample while on the right (b) the current under illumination.

From the topography image (**Figure 3.23a**) the presence of the cubic morphology can be clearly appreciated: it is possible to recognize different facets belonging to the same grain. The current map shown in the **Figure 3.23b** clearly indicates that there is a facet dependent current on these crystals (highlighted in the blue and red rectangles). On the other side, in the region delimited by the white square the crystal shows uniform current through the whole grain.

To dispel any doubt about the possibility that the current variation is due to an artifact effect both the trace and re-trace scans are performed and here reported (**Figure 2.24**): the variation in the relative magnitude of the current is noticed for both the scans.

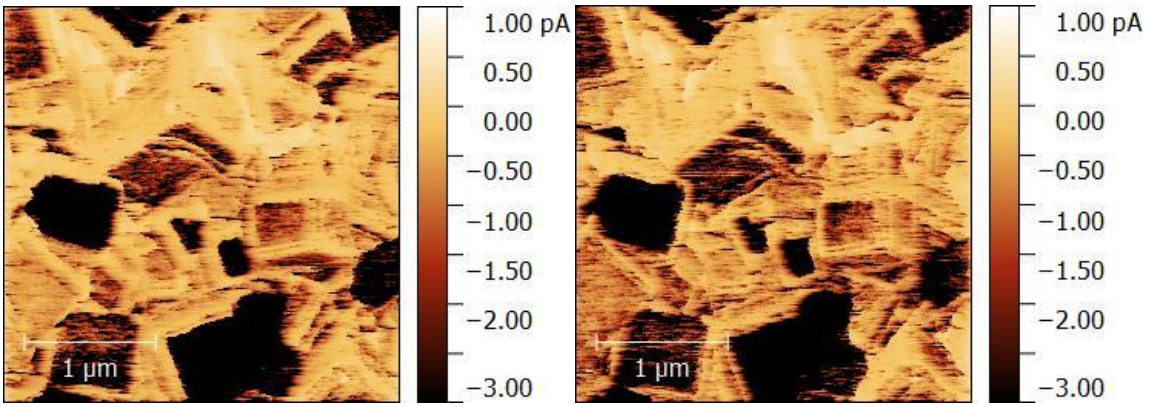

Figure 3.21: pc-AFm measurements of $CH_3NH_3PbI_{3-x}Br_x$ cubic-like morphology in a) trace scan and b) re-trace scan

3.4.2.2. Small (~ 0.5 µm) Cubic-like Crystals

Here the dimension of the grains is slightly smaller than the previous sample and the most interesting information extracted here is that the measured current is slightly higher (**Figure 3.25**).

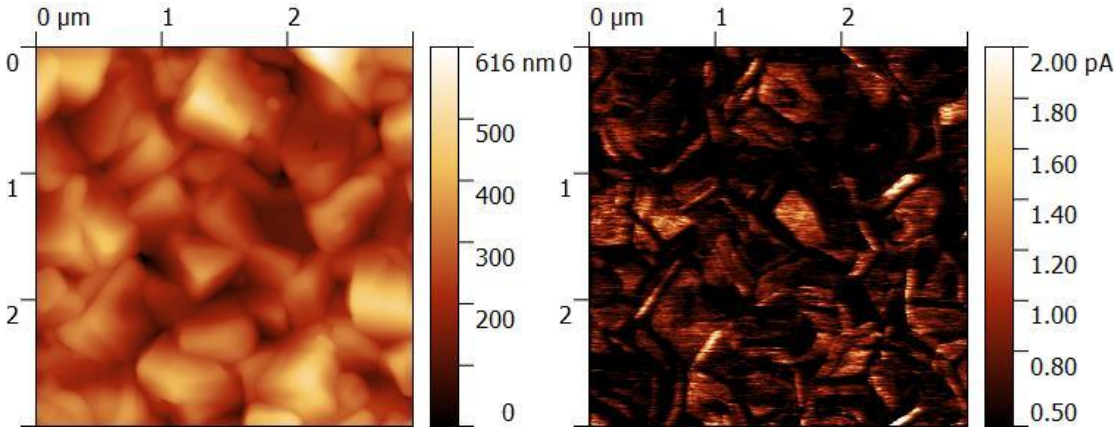

Figure 3.22: (a) On the left the topography of the sample while on the right (b) the current under illumination.

Also in this case no photocurrent is generate (I_{SC} = 0 at V = 0) while under applied bias (-1.5 V) the generated current is higher than the previous sample (bigger grains) indicating better electronic extraction properties. Again the facet-dependence of the current is present.

3.5. First Conclusions and future perspectives

From the preliminary data collected with the pc-AFM it is possible to roughly confirm the hypothesis advanced by Leblebici et al.[13] The synthesis of the cubic shaped crystals allows to scan different facets belonging to the same grain bringing some clear indications. In particular with this morphology the current under applied bias and illumination seems to be facet-dependent since different current values were mapped on the different facets of the same crystal. Moreover with different crystal sizes the recorded current assumes different values: in the medium size grains (~ 1 µm) the current is much lower compared with the small size crystals (~ 0.5 µm): this should focus the attention of the researchers on the relation between the optoelectronic properties of the material and the morphology of the photoactive semiconductor, especially on the dimensions of the crystal. This indication is also consistent with the data obtained from the PL characterization where the higher signals were detected for the smaller grains.

3.6. References

1. Song, Z., Watthage, S. C., Phillips, A. B. & Heben, M. J. Pathways toward high-performance perovskite solar cells: review of recent advances in organo-metal halide perovskites for photovoltaic applications. *J. Photonics Energy* **6,** 22001 (2016).
2. Schulz, P. *et al.* Interface energetics in organo-metal halide perovskite-based photovoltaic cells. *Energy Environ. Sci.* **7,** 1377–1381 (2014).
3. Li, Y. *et al.* Defective TiO2 with high photoconductive gain for efficient and stable planar heterojunction perovskite solar cells. *Nat. Commun.* **2,** 1–18 (2016).
4. Eperon, G. E., Burlakov, V. M., Docampo, P., Goriely, A. & Snaith, H. J. Morphological control for high performance, solution-processed planar heterojunction perovskite solar cells. *Adv. Funct. Mater.* **24,** 151–157 (2014).
5. Stranks, S. D. *et al.* Recombination Kinetics in Organic-Inorganic Perovskites: Excitons, Free Charge, and Subgap States. *Phys. Rev. Appl.* **2,** 1–8 (2014).
6. Liu, F. *et al.* Is Excess PbI2 Beneficial for Perovskite Solar Cell Performance? *Adv. Energy Mater.* **6,** 1–9 (2016).
7. Hsu, H. Y. *et al.* Optimization of PbI2/MAPbI3 Perovskite Composites by Scanning Electrochemical Microscopy. *J. Phys. Chem. C* **120,** 19890–19895 (2016).
8. Jiang, F. *et al.* Synergistic Effect of PbI2 Passivation and Chlorine Inclusion Yielding High Open-Circuit Voltage Exceeding 1.15 V in Both Mesoscopic and Inverted Planar CH3NH3PbI3(Cl)-Based Perovskite Solar Cells. *Adv. Funct. Mater.* **26,** 8119–8127 (2016).
9. Supasai, T., Rujisamphan, N., Ullrich, K., Chemseddine, a. & Dittrich, T. Formation of a passivating CH3NH3PbI3/PbI2 interface during moderate heating of CH3NH3PbI3 layers. *Appl. Phys. Lett.* **103,** 183906 (2013).
10. Wang, S. *et al.* Credible evidence for the passivation effect of remnant PbI2 in CH3NH3PbI3 films in improving the performance of perovskite solar cells. *Nanoscale* **8,** 6600–6608 (2016).
11. Sutter-Fella, C. M. *et al.* High Photoluminescence Quantum Yield in Band Gap Tunable Bromide Containing Mixed Halide Perovskites. *Nano Lett.* **16,** 800–806

(2016).

12. Giridharagopal, R., Shao, G., Groves, C. & Ginger, D. S. New Scanning Probe Techniques for Analyzing Organic Photovoltaic Materials and Devices. *Asylum Res. Appl. Note* (2009).
13. Leblebici, S. Y. *et al.* Facet-dependent photovoltaic efficiency variations in single grains of hybrid halide perovskite. *Nat. Energy* **1,** 16093 (2016).
14. Kutes, Y. *et al.* Mapping the Photoresponse of CH3NH3PbI3 Hybrid Perovskite Thin Films at the Nanoscale. *Nano Lett.* **16,** 3434–3441 (2016).

4. Perovskite Nanostructuring

This chapter reports the nanopatterning of the $MAPbI_3$ Perovskite. While the first trials were done with thermal nanoimprint lithography (T-NIL), the subsequent tests were focused on the Pulsed-NIL technology, an ultrafast version of the T-NIL, based on stamps with integrated heaters. By Pulsed-NIL it was demonstrated the possibility to replicate onto the hybrid perovskite the structures of a stamp having details in the sub-100 nm scale, in spite of its crystalline nature. This chapter shows the possibility of using organo metal halide perovskites for optoelectronic devices with more complex architectures than just planar films.

4.1. Motivation

Inspired by the use of textured Silicon wafers already in PV devices, we applied the same nanopatterning concept to organo-lead halide perovskite layers. As reported in literature, the structures (random pyramids or V-groove geometry) implemented in the mono-Si SC improve the efficiency of the device. Images showing the textured silicon surface are reported in **Figure 4.1a**. This enhancement in efficiency is due to the mitigation of light losses occurring at the interface between air and silicon, two media with different refractive index: in particular the morphology of the Si surface is modulated to minimize he energy loss due to reflection.

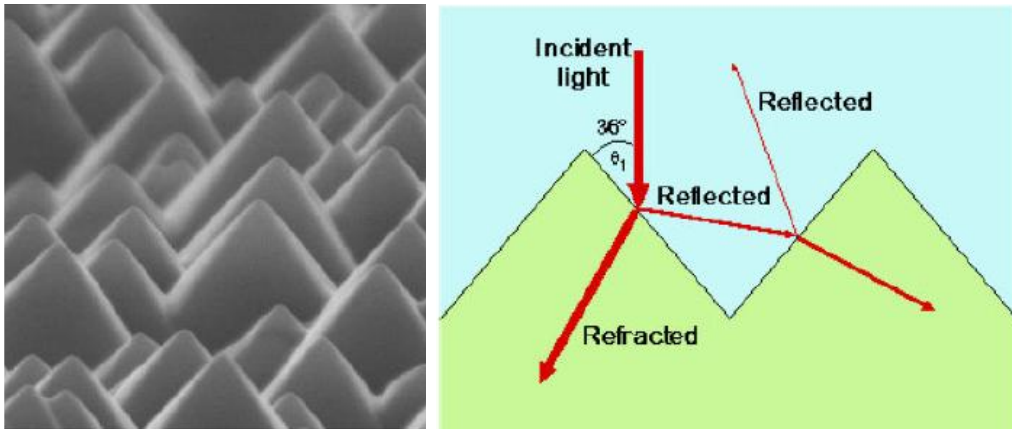

Figure 4.1: a) mono-Si wafer pyramid-textured and b) scheme of the reflected and refracted light hitting a textured Si-surface.

When the radiation hits a planar surface part of it pass through the material with a refracted angle while part is reflected back in the medium of provenience. This represents a loss, since not all the radiation (the reflected portion) reaches the photoactive material. An effective method to minimize the intensity of the reflected light is provided by texturing the surface (**Figure 4.1b**). A common method to obtain rather inexpensively the texturing of the crystalline silicon solar cell is to exploit the properties of the wet anisotropic etching of the silicon (100): in particular the (111) planes are slow etching planes; in a concentrated KOH bath the etching of a (100) silicon substrate results in surfaces with randomly distributed pyramidal defined mostly by (111) facets (**Figure 4.1a**).

In our case, the motivation of structuring the perovskite films was twofold, namely *i)* to find a method to exploit scattering structures in order to play with effects such as total internal reflection and the enhancement of optical path within the layer to enhance the absorption, *ii)* to find a general method to produce nanostructures in the halide perovskite film, for possible application in more complex optoelectronic devices, such as Distributed Bragg Reflector Lasers. Total internal reflection in particular occurs when the light pass from a medium with a certain refractive index (medium 1) to a material with lower refractive index (medium 2) (**Figure 4.2**).

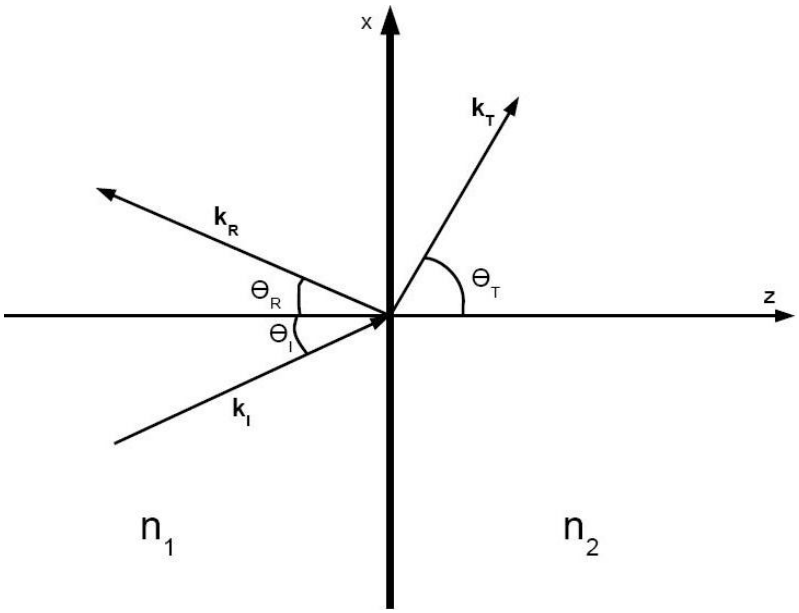

Figure 4.2: Snell's Law

This behavior is described by the Snell's law as following (**4.1**):

$$n_1 sin\theta_i = n_2 sin\theta_t \quad \textbf{(4.1)}$$

Where n_1 and n_2 are the refractive index of the two media, θ_i is the angle between the incident radiation and the normal to the interface and the θ_t is the angle between the normal and the transmitted light. Rearranging the equation (**4.1**) it is possible to obtain the equation below (**4.2**):

$$sin\theta_i = \frac{n_2}{n_1} sin\theta_t \quad \textbf{(4.3)}$$

It is necessary to introduce the concept of the critical angle: when radiation hits an interface at an angle larger than the critical angle the radiation is entirely reflected back, generating the total internal reflection. The critical angle corresponds to the condition $\theta_t = 90°$ or equivalently $\sin\theta_t = 1$. The angle $\theta_i = \theta_c$ for the incident beam corresponding to the transmitted beam parallel to the interface is now also expressed as following rearranging equation (**4.2**):

$$\theta_i = \theta_c = arcsin\frac{n_2}{n_1} \quad \textbf{(4.3)}$$

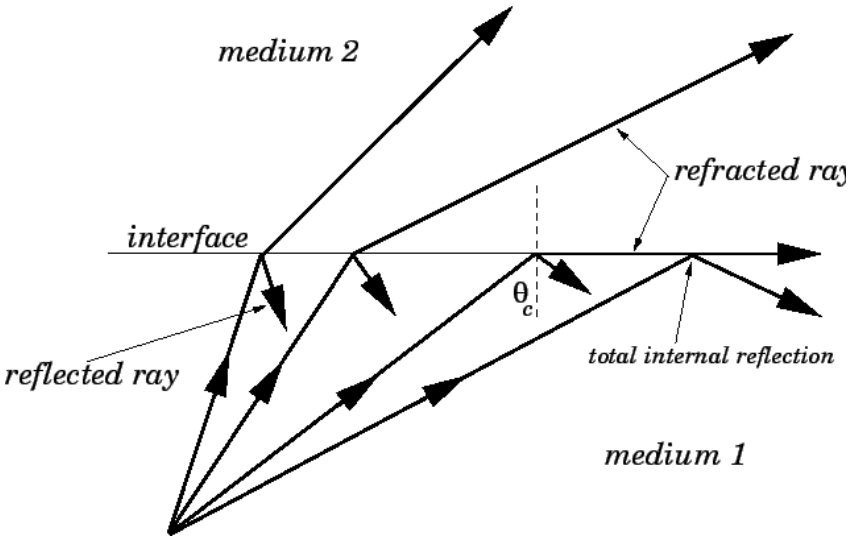

Figure 4.3: Total internal reflection

In the case of the perovskite solar cells the total reflection, and the consequent enhancement of optical path within the material could be exploited at the interface between the organic-lead halide perovskite and the Spiro-OMeTAD HTM. The desired

effect is the total reflection allowing the not absorbed radiation to cross again the absorbing material. In this way the radiation path is longer avoiding the use of thicker layers (which typically results in a reduced charge collection efficiency).

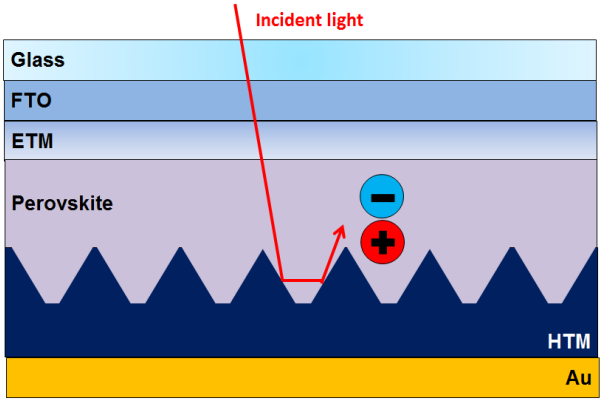

Figure 4.4: Conceptual representation of photonic nanostructures integrated in a perovskite photovoltaic cell.

In literature the refractive index for the semiconductor perovskite $CH_3NH_3PbI_3$[1] is reported to be in the range 2.5-2.7 and for the organic hole transporting material Spiro-OMeTAD 1.6-1.7[2], both depending on the wavelength within the region of interest for the SC. The electromagnetic radiation enters the p-SC from the side of perovskite absorber and then enters the Spiro. Calculating the critical angle with the equation (**4.3**) in the visible spectral window the minimum value obtained is 36.8°. Given this critical angle for the methylammonium lead iodide/Spiro-OMeTAD interface suitable light trapping structures are the same pyramids exploited as antireflective structures in the silicon based solar cells (**Figure 4.1**). Therefore, an effort was put into the patterning of similar pyramidal textures into the perovskite layer. To transfer this pattern I propose the imprinting lithography using as a stamp an array of inverse-pyramids (or V-groove) obtained by anisotropic wet etching of a silicon (100) substrate in potassium hydroxide (**Figure 4.5**).

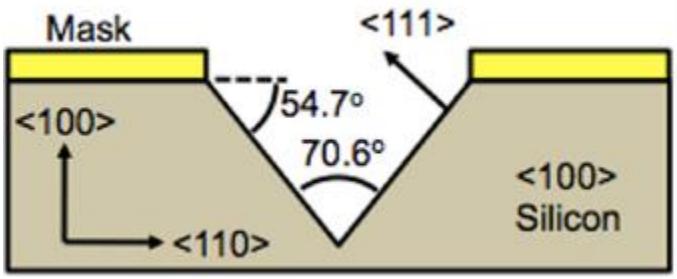

Figure 4.5: Etching of silicon by KOH

4.2. Thermal Nanoimprint Lithography (T-NIL) as preliminary approach to Pattern the Halide Perovskite

The T-NIL technique was the first one that I used to transfer the pattern on the halide perovskite layer. Thermal nanoimprint lithography is mainly used for nanostructuring thermoplastic polymers. Therefore, it was unclear whether it would have been possible to use the same process on the hybrid organic-inorganic perovskite. As before reported the semiconductor is polycrystalline and certainly does not behave, from the rheological point of view as usual imprinting resists.

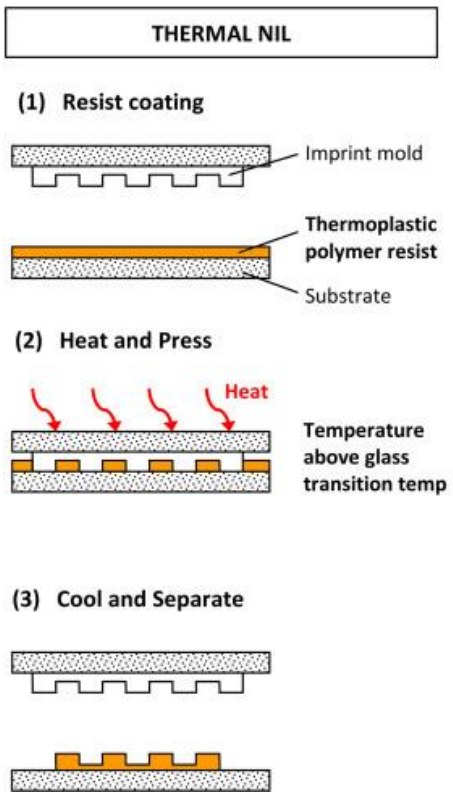

Figure 4.6: Thermal imprinting process

Nanoimprint Lithography is based on a rather simple working principle and simple setup (**Figure 4.6**). The latter consists of a press with two heating plates that are heated at the desired temperature in order to melt the material onto which the features of a nanostructured stamp are indented. Between the plates the substrate for the imprinting and a silicon mold with the interested pattern are loaded with the relevant sides facing to the other: the structures of the silicon master and the layer for the imprinting are exposed one to each other.

The implemented process can be sub-divided in steps as illustrated in **Figure 4.7**. The perovskite semiconductor is deposited onto the substrate *via* solution process and partially dried onto the hot plate (2' at 95°C). The sample is then transferred with the silicon master into the setup for the thermal imprinting: the plates are heated up to the desired temperature (100°C for the perovskite) then the pressure is applied (between 50 and 100 bar). After a certain indentation time (roughly 10' for the perovskite at the above conditions) the plates and the entire stack of stamp/substrate are cooled down to room temperature (RT) and the

pressure is released. The sample once separated from the stamp is ready to be characterized.

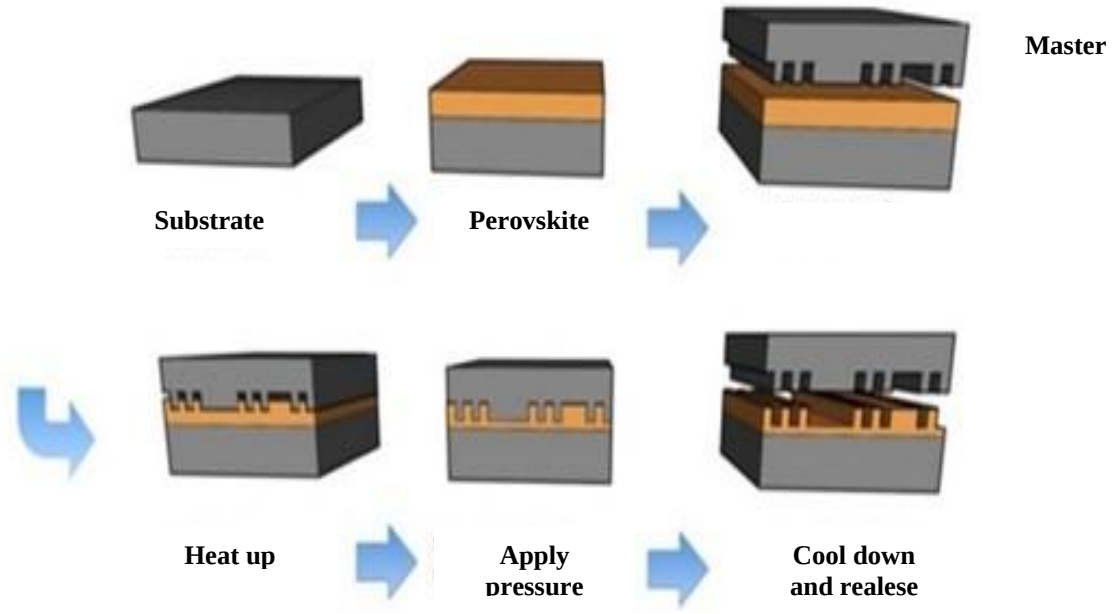

Figure 4.7: scheme of T-NIL steps

Several deposition and imprinting conditions were explored and optimized in part. SEM of the preliminary results obtained by T-NIL are shown below (**Figure 4.8**).

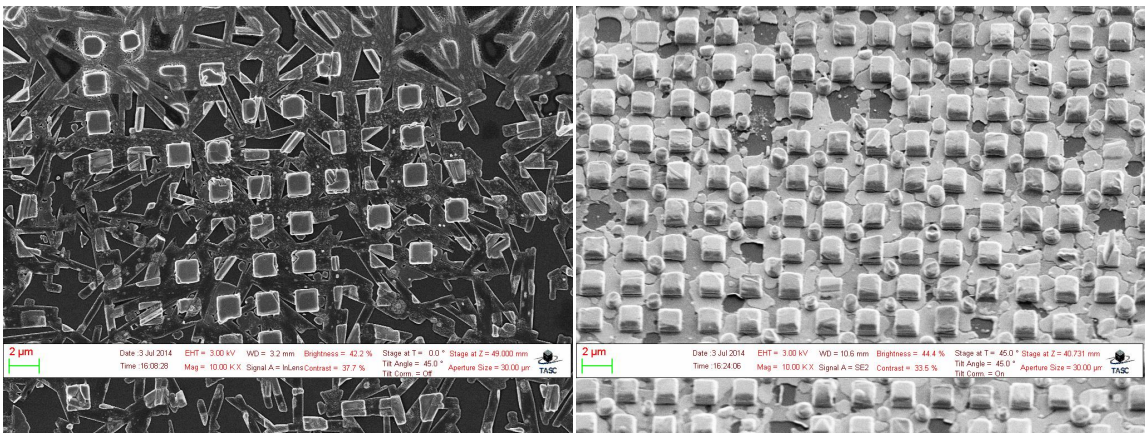

Figure 4.8: On the left top view of imprinted $CH_3NH_3PbI_3$. On the left a tilted view of nanopatterned PbI_2 layer.

On the left it is possible to observe in top view of the discontinuous $CH_3NH_3PbI_3$ layer deposited. The structures are imprinted, though not entirely but the main problem here it the quality of the deposited layer. On the right, in titled view (45°), PbI_2 is spin coated and again imprinted with the same master and conditions. Other experiments were carried out, but these preliminary results were considered sufficiently successful to motivate the next step, i.e. the testing of the *Pulsed-NIL* on the same task of patterning the perovskite films, in a much shorter time-scale.

Secondarily, the need to move to the *Pulsed-NIL* was due to some practical limitations of the thermal setup and of the T-NIL technique in general. In particularly the available setup had a poor force resolution in the pressure range (50-100 bar) required for the imprinting of small samples of 25 x 25 mm^2, usually used for the fabrication of SC at the IOM-CNR.

Since the analogue pulsed technique was available at the IOM-CNR laboratory, thanks to the cooperation with the company ThunderNIL, I decided to focus my attention on the optimization of the imprinting process using the "ULISS" Pulsed-NIL setup.

4.3. Patterning Methylammonium Lead Halide Perovskite by Pulsed Nanoimprint Lithography (P-NIL)

Cefarin N., Cian A., Sonato A., Sovernigo E., Suran F., Teklu Z., Zanut A., Pozzato A., Tormen M. Nanostructuring methylammonium lead iodide perovskite by ultrafast nano imprinting lithography. Microelectron. Eng. 176, 106–110 (2017)

The possibility to switch from the T-NIL to the Pulsed-NIL technique solved the practical issue about the pressure control. Moreover as below explained the P-NIL has the great advantage that the thermal cycle can be accomplished in less than one millisecond instead of several minutes (~ min 30). The only time consuming step is the motion of the press plate, which in future versions of the equipment could be reduced to below 10 sec.

Pulsed-NIL, an evolution of the nanoimprint lithography,[3] has enabled the patterning of thermoplastic films on full wafers (currently 4" but the process is scalable to larger areas) on the 100 µs time-scale.[4] The setup ULISS (**Figure 4.9**), developed by ThunderNIL Srl, is performed in a very different window for the relevant physical parameters than T-NIL.

Figure 4.9: on the left the ULISS setup. On the right P-NILchamber with the reflecting nanopatterned master.

In the P-NIL process a modified mold with an integrated heater (**Figure 4.10**) is connected to high-power pulse generator, and instantaneously heated by a short and intense current pulse. Due to the 2D-integrate Joule's heater buried below its patterned surface it can reach high temperature with a short duration current pulse (in the range of 10-100 µs): the surface of the mold is in contact with the layer or the substrate under process and there is a heat transfer at the interface.[4] The typical range of temperature reached within the cycle can be 400-600 °C, depending on the material being imprinted.

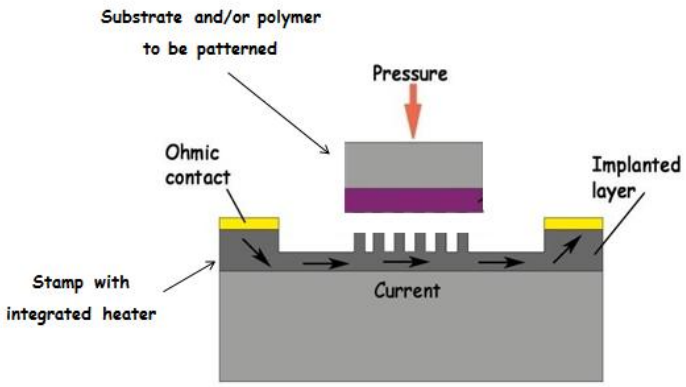

Figure 4.10: modified mold for the P-NIL setup

Figure 4.11 shows the conceptual differences for the heating step between the two techniques here considered: the ULISS setup does not heat unnecessarily large volumes (the steel plates with large thermal capacity) and the process can be carried out in a short time window. Another very interesting function of the P-NIL is the possibility of using the so called multi-pulse approach where several pulses are applied to the sample with the desired intensity an frequency.

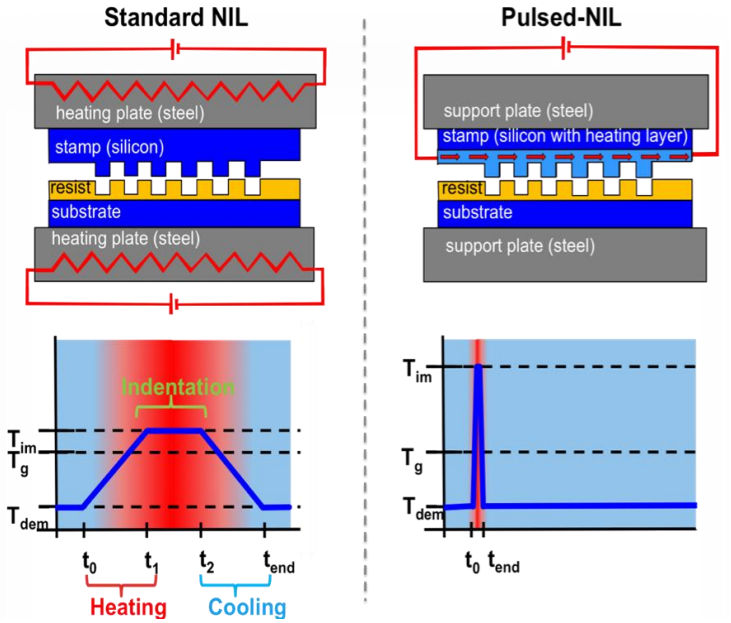

Figure 4.11: Comparison between the T-NIL and the P-NIL techniques

Also for this setup were prepared some simple silicon masters with squared holes in order to obtain the complementary pillars. In the next sections I report preliminary but very promising results obtained with silicon masters with inversed-pyramids and V-grooves.

4.3.1. Pyramidal Microstructures in Organo-Lead Halide Perovskite

As reported in the motivations, the most interesting structures for the PV technology it is possible to find the pyramidal shape. Below the fabrication of the master and the results obtained is described.

4.3.1.1. Master Fabrication

The fabrication of the silicon master was the first step to carry out the desired experiments. The nano-structured mold was obtained after the following steps. Onto the silicon substrate a suitable resist is spin coated and a fishnet structure is imprinted into it by conventional T-NIL: the surface has an array of squared pillar (width 400 nm with periodicity 800 nm) and a residual layer corresponding to the fishnet area. The thin residual layer is removed by oxygen plasma in order to remain with isolated resist square pillars with exposed silicon on the fishnet area. 25 nm of chromium are sputtered afterwards and the resist is removed in acetone: the substrate is coated with a net of Cr delimiting silicon squares (400 x 400 nm^2). The exposed silicon (100) is subjected to the wet anisotropic etching *via* KOH leading to inverted pyramids in the silicon master. The Cr/resist mask controls the dimensions of the resulting structures: since silicon surface is exposed in dots with diameter of 400 nm the resulting inverted pyramid has a squared base of 400 nm and the periodicity of 800 nm. Finally, the Cr mask is removed by wet etching, the surface is cleaned and activated by oxygen plasma and a layer of octadecylsilane is deposited on the surface as anti-adhesion treatment.

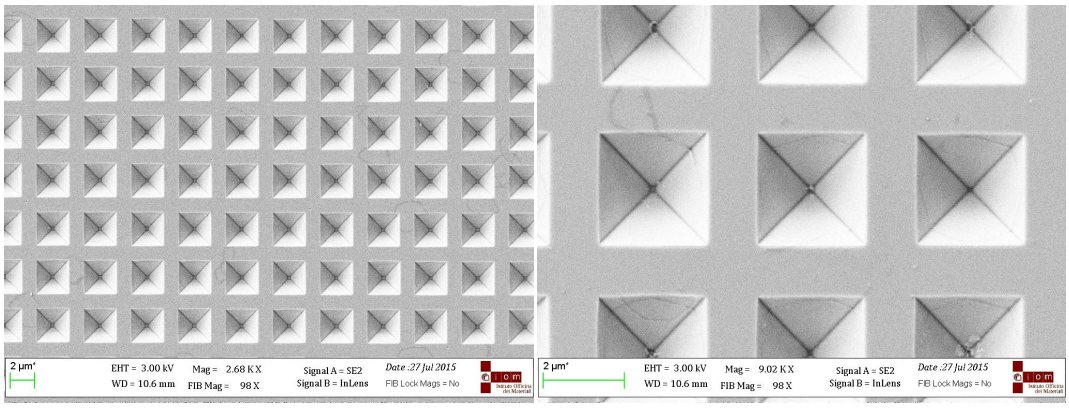

Figure 4.12: Inverse pyramid structures on the silicon master with different dimensions.

After the patterning of the stamp, the heating layer is contacted at two opposite edges with the copper ribbons acting as electrical contacts.

4.3.1.2. Imprinting Process

The pure iodine $CH_3NH_3PbI_3$ is spin coated with one solution process (i.e. dissolving two salts, metal halide and methylammonium halide, in an organic solvent) onto a silicon or glass/FTO substrate and dried for 2' at 95°C (the perovskite film was deposited in a nitrogen-filled glovebox at low humidity and oxygen conditions). The coated sample is then loaded into the ULISS setup: the conductive pyramid master is on the bottom of the chamber while the substrate is put on it faced down. To increase the uniformity of the process compliance layers are used between the plates and the samples. At that point the upper plate moves down and applies the desired pressure to the master/sample (50 bar if glass/FTO ad 100 bar if silicon): under this conditions the pulse (700 V, 350 A peak) is applied to heat up the system and to induce the process of indentation. Once the process is completed the pressure is released and the sample is removed. Below I report some SEM images to show the achieved results.

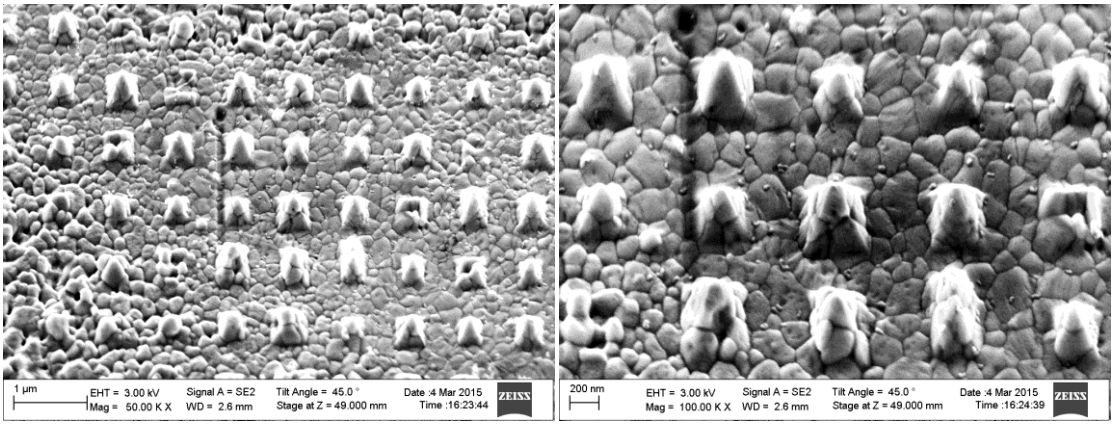

Figure 4.13: Methylammonium lead iodide patterned layer with pyramids

As it is possible to see in **Figure 4.13** the desired pyramidal shape is transferred into the photoactive layer. The grain boundaries due to the poly crystalline morphology are well visible on both the surface and the nano-structures. As it is possible to guess from the less magnified image, the imprinting process is not uniform and this is well visible in the following SEM image (**Figure 4.14**).

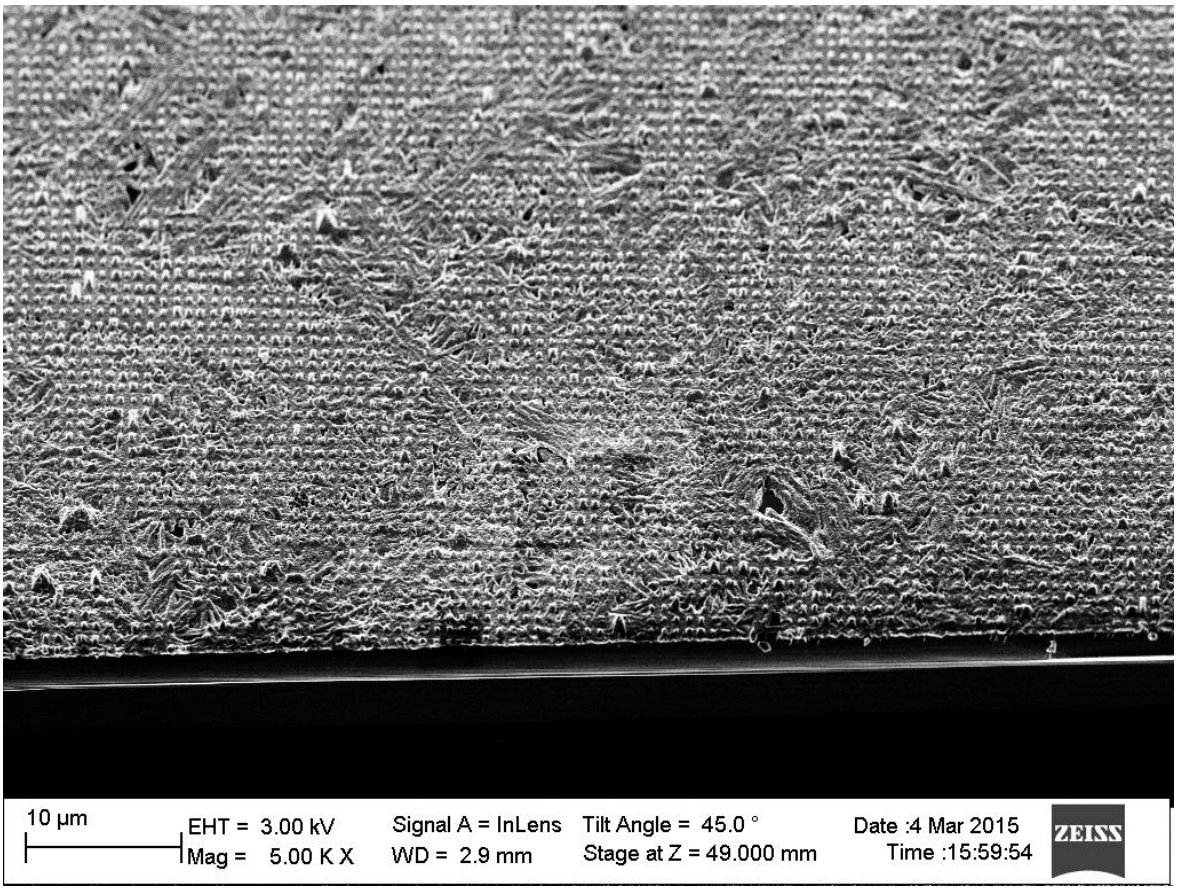

Figure 4.14: tilted view at low magnification of the patterned perovskite layer.

There are large regions where the nanostructures are well transferred and others where the surface is not affected by the process. Many trials were done to enhance the coverage of the layer with the desired pyramids. Unfortunately changing the parameters to more aggressive conditions (high pressure and pulse intensity) the glass substrate brakes, probably due to large thermo-mechanical stresses. The nano-structured pyramids have dimensions comparable with the grains size of the photoactive material: this condition is particularly suitable to tear away the patterned domains during the release of the pressure and the detachment of the substrate from the silicon master.

We tried also to fabricate some solar cell (**Figure 4.15**) with this layer without improving the efficiency with respect to flat layer SC. In the following figures it is possible to see the gold top contact layer of a complete device: it is easy to notice that the pyramids were not transferred homogeneously on the layer. Moreover some peak are not well covered with gold top contact.

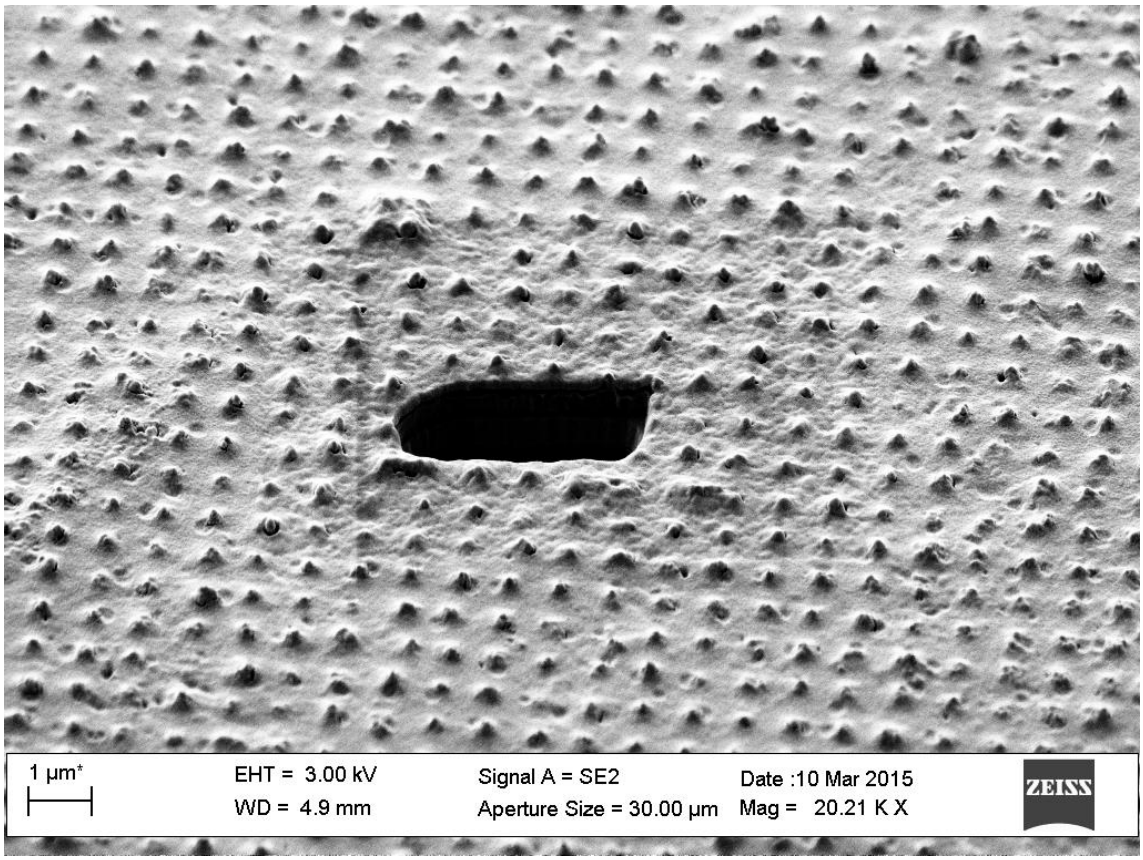

Figure 4.15: tilted view of a complete SC with patterned perovkite. The top material is Au

Due to the issues met during this process it was decided to try a different type of nanostructures suitable for the total internal reflection: the V-grooves.

4.3.2. V-groove Structures in Organo-Lead Halide Perovskite

V-groove microstructures seem to be more mechanically stable structures than micro-pyramids to survive to the step of stamp detachment. In fact grooves are tapered in one directions, while pyramids are tapered in two directions.

The nanostructures fabricated onto the master had a lateral width of around ~ 500 nm and a periodicity ~ 100 nm reaching a high ~ 380 nm. For this nanostructures Laser Interference Lithography (LIL) was used to pattern the resist necessary to complete the master fabrication.

4.3.2.1. V-groove:Master Fabrication

The stamp fabrication starts from a silicon (100) substrate with a top highly-phosphorous-doped layer, according to the preparation already described reported in

literature[4,5]and proceeds according to the following four steps (**Figure 4.16**): (1) Silicon is oxidized at the surface, (2) Interference Lithography is performed on a photoresist (3) the patterned is transferred into the oxide layer by wet etching (4) the oxide is used to mask the silicon during the wet anisotropic etching in KOH based aqueous solution.

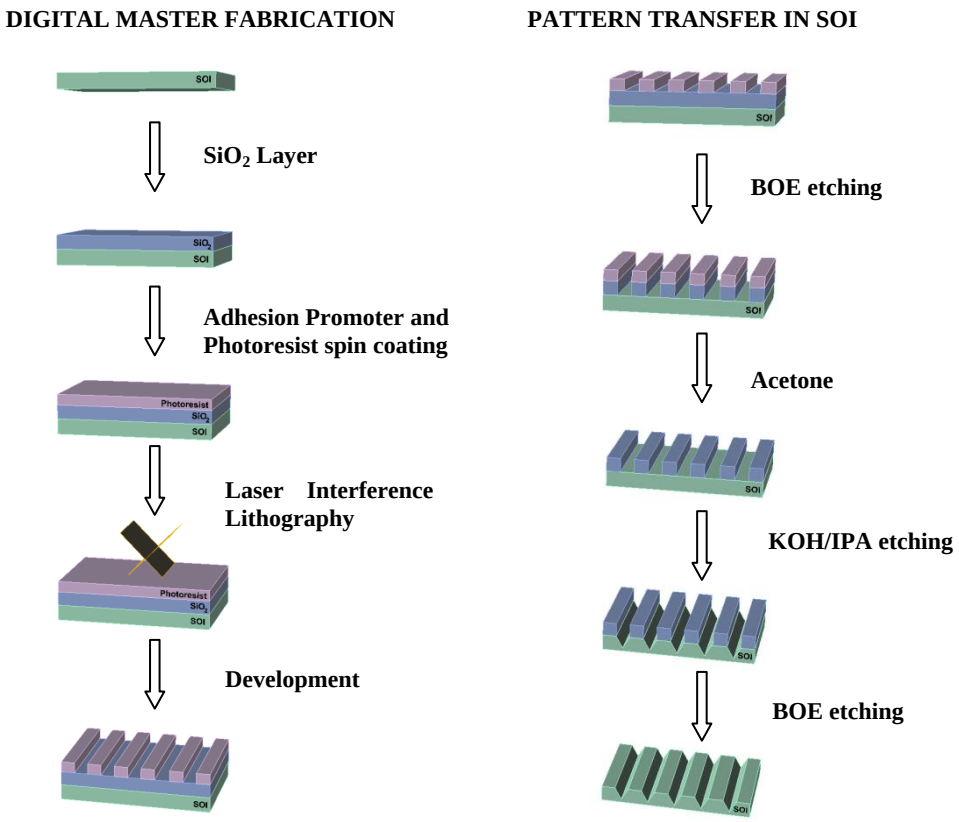

Figure 4.16: 2-step fabrication process of the mold for ultrafast thermal Nano-Imprinting Lithography. A digital photoresist grating on the Pulsed-NIL blank stamp is fabricated by using laser-interference lithography and used as mask for the pattern transfer into doped-silicon by wet anisotropic etching

More in detail the steps involved were the following. A SiO_2 film was obtained by wet oxidation of a doped-silicon substrate for 32 min at 1000°C. After cleaning (in H_2SO_4:H_2O_2 - 7:3 piranha - solution at 95°C for 5 minutes followed by oxygen plasma treatment) the substrate was coated with an adhesion promoter (HMDS) and then with S1805 photoresist diluted into propylene glycol monomethyl ether acetate (PGMEA) (2 : 3) by spin coating. After soft baking the sample was exposed by Laser Interference Lithography (LIL) with an optimized dose and at a precisely defined incidence angle (depending on the desired grating period). The laser beam is deflected by a system of aluminum mirrors before passing through a spatial filter that suppress high spatial-frequency noise components in order to produce a clean Gaussian beam profile. A part of

the beam section illuminates directly the sample whereas the rest of the beam section impinges first on a mirror positioned perpendicularly to the sample substrate and from the mirror is reflected onto the sample, leading to the interference of the direct and indirect beams. The frame supporting the mirror and the sample can be translated and rotated with respect to an axis orthogonal to the beam propagation direction with 0.01° precision providing a fine control on the structure periodicity. The development was performed and finally the sample was thoroughly rinsed in milliQ water. It is possible appreciate the final master with V-groove structure in the following SEM images (**Figure 4.17**):

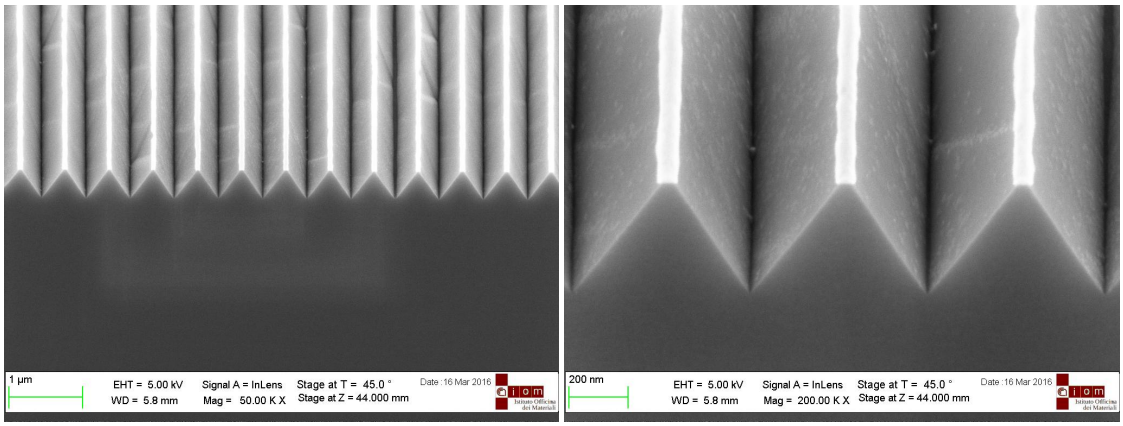

Figure 4.17: V-groove silicon master

4.3.2.2. V-Groove: Imprinting Process

Perovskite was synthesized according to the one-step deposition, i.e. dissolving two salts, metal halide and methylammonium halide, in an organic solvent. The solution of pure iodine perovskite $CH_3NH_3PbI_3$ is spin coated as previously reported in a nitrogen-filled glovebox with controlled humidity and oxygen conditions. The substrate is a doped-silicon coated by a titania film of 50 nm deposited via sol-gel technique. The substrate was then annealed at 95°C for 2 min in a glovebox. The sample was transferred to the ULISS setup and immediately imprinted applying 50 bar pressure and a single pulse equal to 700V using the V-groove stamp electrically connected to the power system.

As before, the imprinting process is successfully executed and the homogeneity of the structures higher compared to the pyramid texture. Again it is possible to recognize (**Figure 4.18**) the grain boundaries typical of the halide perovskite material. Some defects are present onto the structures due to the propagation of the defects from the master to the final substrate.

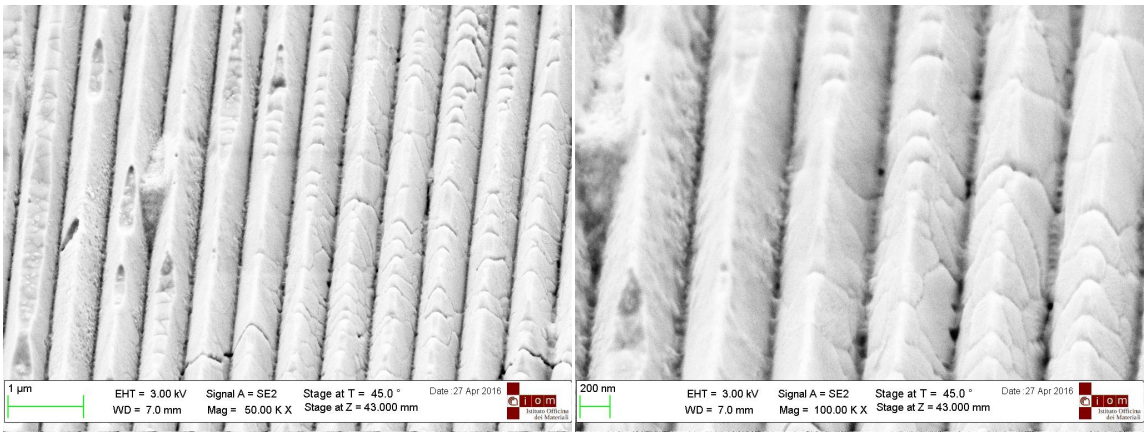

Figure 4.18: V-groove patterned $CH_3NH_3PbI_3$

The overall uniformity of the imprinted surface is better seen in SEM images (**Figure 4.19**) obtained at lower magnification. The holes in the film were clearly originated in the spin coating step.

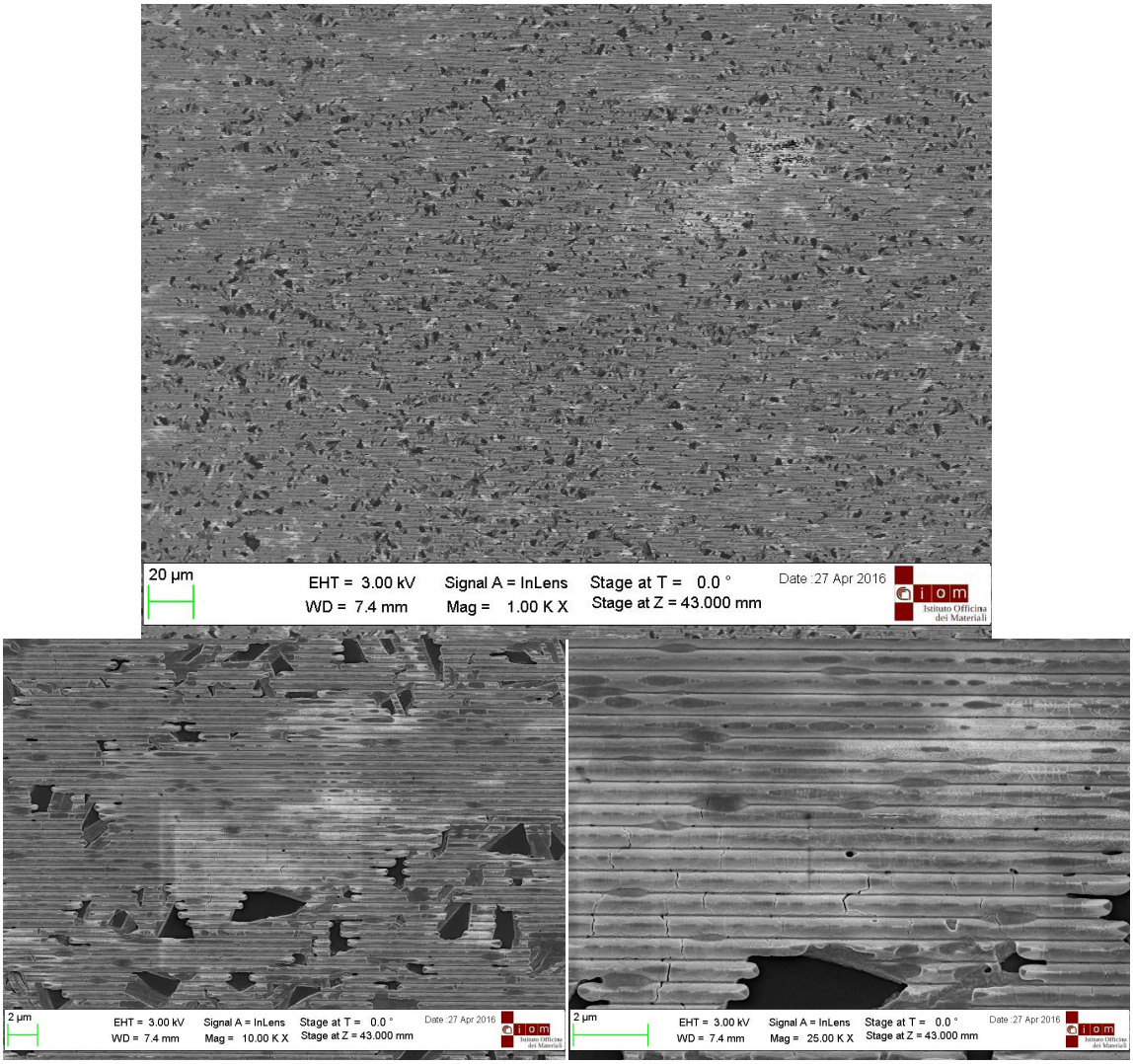

Figure 4.19: top view of V-groove patterned $CH_3NH_3PbI_3$

After the first promising trials for urgent and unexpected reasons linked to a problem of the building, the clean room with the necessary equipment was closed for a couple of months, stopping the program on the nanostructuring of the perovskite material, before I moved from Trieste to Berkley to continue the activity at the LBNL.

4.4. Conclusions

Very promising preliminary results were achieved demonstrating that the methylammonium lead iodide is suitable to be nanostructured *via* nanoimprint lithography. Thermal-NIL was a good starting point to test the imprinting of the polycrystalline material while the Pulsed-NIL confirms the possibility to transfer the desired structures to the layer in a fast and cost-effective way. Depending on the dimensions and the geometry of the structures the imprinting process might lead to more or less uniform imprinting. Next steps will comprise the chemical-physical characterization as well as the evaluation of the optoelectronic properties of the samples before and after the process. Moreover the V-groove sample will be integrated in a solar cell to see if there is a gain in efficiency due to the total internal reflection occurring at the interface between the semiconductor and Spiro-OMeTAD.

In addition, nanostructure the photoactive material holds promise for different optoelectronic applications.

4.5. References

1. Chen, C.-W. *et al.* Optical properties of organometal halide perovskite thin films and general device structure design rules for perovskite single and tandem solar cells. *J. Mater. Chem. A* **3,** 9152–9159 (2015).
2. Ball, J. M. *et al.* Optical properties and limiting photocurrent of thin-film perovskite solar cells. *Energy Environ. Sci.* **8,** 602–609 (2015).
3. Zhou, W. *Nanoimprint Lithography: An Enabling Process for Nanofabrication*. (213AD).
4. Tormen, M., Sovernigo, E., Pozzato, A., Pianigiani, M. & Tormen, M. Sub-100 l s nanoimprint lithography at wafer scale. *Microelectron. Eng.* **141,** 21–26 (2015).
5. Tormen, M. *et al.* Fast thermal nanoimprint lithography by a stamp with integrated heater. *Microelectron. Eng.* **85,** 1229–1232 (2008).

5. Materials and Methods

In this Chapter it is reported the fabrication of the organo-lead halide perovskite-based solar cell. The deposition methods of all the other transporting materials are then describe, as well as the LP-VASP and the sequential dipping processes.
The fabrication of the silicon masters (pyramidal and V-groove) and the imprinting steps are reported. Finally some general techniques and equipments are described.

5.1. Solar Cell Fabrication

The solar cell is fabricated layer by layer starting from the cleaning of the glass/FTO substrate. The other materials are then deposited in the following order: c-TiO_2, $CH_3NH_3PbI_{3-x}Br_x$, Spiro-OMeTAD and gold counter electrode.

5.1.1. Substrate Preparation

The substrate used for the fabrication at the LBNL is a glass coated with FTO (TFD, 7-10 Ω/sq) already patterned. The dimensions are 14 x 16 mm^2 and optimized to fit in the holder used for the sun simulator setup present at the Molecular Foundry (LBNL). Before the deposition of the TiO_2 interested material the sample is cleaned as following:[1]

- The sample is immersed in a detergent/deionized water solution (Alconox 1%) in an ultrasonic bath for 10 min;
- The detergent/water solution is discarded and the sample rinsed with milliQ water 5 times;
- The sample is immersed in acetone in ultrasonic bath for 10 min;
- The substrate is immersed in isopropanol in ultrasonic bath for 10 min;
- The sample is then dried with N_2 gun.

At the IOM-CNR the glass/FTO substrate (**Figure 5.1**) is purchased (VisionTek Systems, 15 Ω/sq) in large slides (100 x 100 mm^2): to prepare the samples the slide is cut in pieces 25 x 25 mm^2. Moreover to have regions with bare glass exposed, the FTO is etched on two opposite edges with Zn powder and HCl solution (2M).[2]

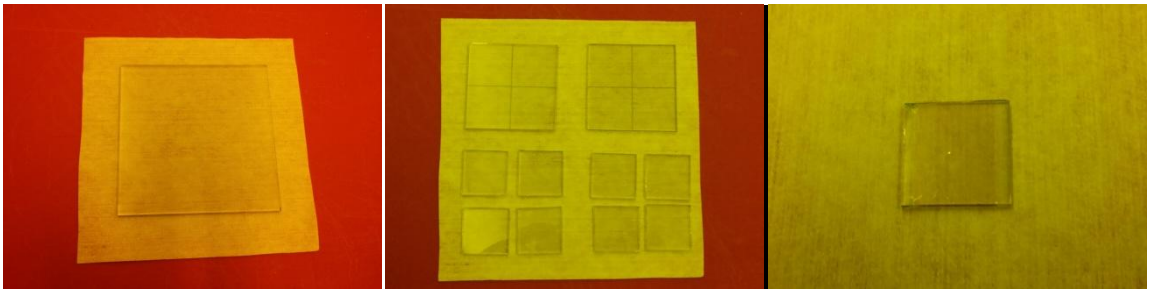

Figure 5.1: in order from left to right: 100x100 mm^2 glass coated with FTO, cut 25 x 25 mm^2 pieces and one sample with two etched sides.

5.1.2. Deposition of c-TiO2

The ETM is deposited onto the desired substrate with two different techniques: the sol-gel (IOM-CNR) and the electron beam evaporation (LBNL).

The sol-gel solution[3] consist of 0.23 M titanium isopropoxide (Sigma-Aldrich, 99.999%) and 0.013 M HCl solution in isopropanol (>99.9% Fisher Chemicals). The solution is prepared dissolving titanium(IV)-isopropoxide (555 µL) in isopropanol (7.62 mL). Finally, HCl (52.5 µL) was added dropwise to the titanium precursor solution under heavy stirring. The solution was filtered with a PTFE filter with 0.2 mm pore size before use. The solution is spin coated on the substrates at 2000 rpm for 30 seconds, then the sample annealed at 500 °C using the following ramp:

- 25°C → 500°C (10°/min, 48' total)
- 500°C 1h
- Cooling down overnight.

The final film is around 35 nm thick.

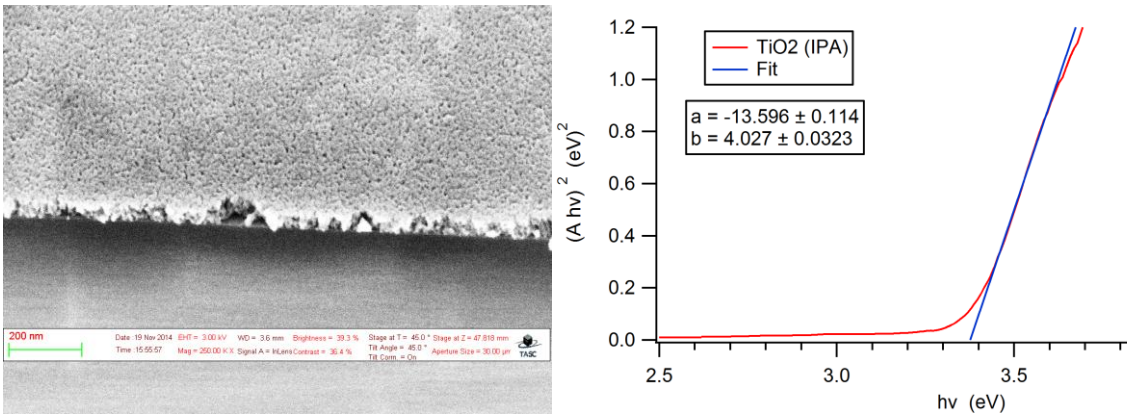

Figure 5.2: SEM image of compact TiO_2 layer obtained through spin coating and Tauc plot analysis.

From the SEM tilted (45°) image it is possible to observe a compact thin (~35 nm) film while from the Tauc plot analysis it is extracted a band gap smaller than 3.4 eV and in good agreement with the literature (3.2 eV).

At the LBNL facility the optimized deposition of the TiO_2 layer is performed by electron beam evaporation (Angstrom Engineering, NEXDEP). In particular TiO_2 pellets (Kurt J. Lesker, 99.9% purity) are used as source for the evaporation, conducted under an acceleration voltage of 7 kV and at a base pressure of ~ 4×10^{-6} Torr. To improve the quality of the material the substrate is heated at 350 °C and kept under rotation (27 rpm). The evaporation rate is low ~ 0.5 Å/s to obtain a flat and pinhole-free layer with a thickness of 80 nm.[4–6]

5.1.3. Methylammonium Lead Halide ($CH_3NH_3PbX_3$) Deposition

The $MAPbI_3$ is synthesized reacting the lead iodide (PbI_2) and the methylamine iodide (MAI) while the pure bromide analogue is obtained combining $PbBr_2$ and MABr. The lead halide salt is purchased while the organic compound is synthesized from methylamine and the relative halide acid.

Depending on the deposition process the methods are different. Below it is reported the synthesis of the methyammonium halide compounds, followed by the description of the LP-VASP and of the solution process.

5.1.3.1. Mehtylammonium Halide (CH_3NH_3X) Synthesis[1]

In a 250 mL round bottom flask equipped with a stir bar, ethanol (100 mL) and methylamine (190 mmol, 16.5 mL, 40%wt in H2O) are poured. The system is cooled to 0˚C with an ice bath and HI (76 mmol, 10 mL, 57%wt in H2O) or HBr (76 mmol, 8.6 mL, 48%wt in H2O) are added dropwise to the solution under stirring. The flask is sealed with a septum and the reaction left at 0˚C for 2 h. The reaction flask is removed from the ice bath and the solvent and unreacted volatile components are evaporated at reduced pressure with a rotary evaporator with a 60 ˚C water bath. The white powder so obtained is dissolved in warm (~50 °C) ethanol (100 mL) and slowly diethyl ether (200 mL) is added to induce crystallization of a white solid. First the flask is left to cool at room temperature for 4 h then is kept overnight at 4 ˚C. The desired product and the solution are filtered over Büchner funnel and filtering paper, then the powder is washed with cold (0˚C) ethanol. The white solid is dried under vacuum at 80 ˚C overnight. This procedure yields (58.9 mmol, 9.360 g, 77%) of methylammonium iodide (MAI) and (55.5 mmol, 6.229 g, 73%) of methylammonium bromide (MABr) and the compounds are stored in the dark and in a desiccator at room temperature in order to minimize decomposition over time. Both the products are also characterized by proton Nuclear Magnetic Resonance (^{1}H NMR):

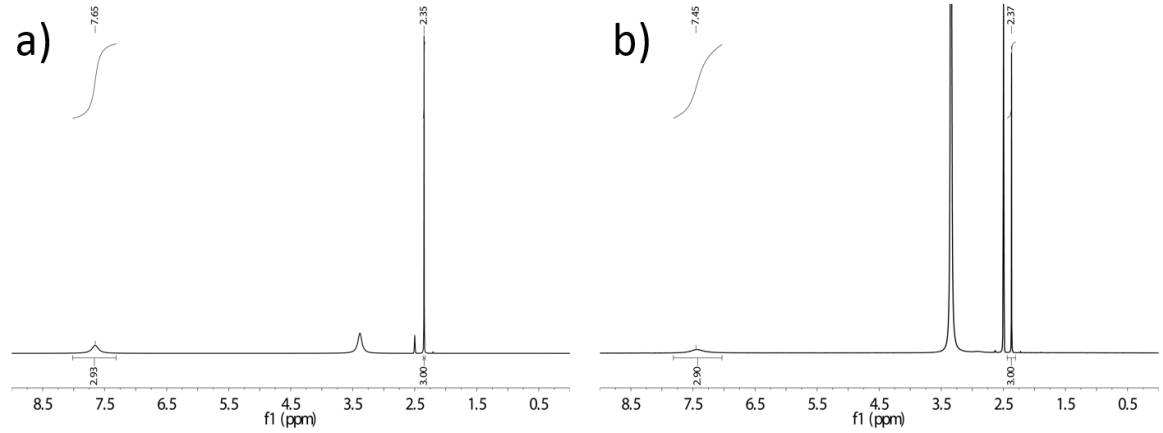

Figure 5.3: a) ^{1}H NMR of MABr in DMSO-d6. Peaks at δ 7.65 (br s, 3H) and 2.30 (s, 3H) ppm confirm the identity of the molecule.[7] b)^{1}H NMR of MAI in DMSO-d6. Peaks at δ 7.45 (br s, 3H) and 2.50 (s, 3H) ppm confirm the identity of the molecule.[8] The peaks at 2.50 and 3.33 ppm are due to residual DMSO and water.

5.1.3.2. Low Pressure-Vapor Assisted Solution Process (LP-VASP)[1,4–6,9]

Here it is presented a protocol for the deposition of pinhole-free, continuous $CH_3NH_3PbI_{3-x}Br_x$ thin films for the application in high efficiency solar cells and other optoelectronic devices. The whole process might be divided as following:

- test tube preparation
- precursor preparation
- lead halide deposition
- vapor-assisted annealing

5.1.3.2.1. Test Tube Preparation

A 50 mL Schlenk tube (diameter 2.5 cm) is loaded with 0.1 g of methylammonium halide. To prevent the chemicals sticking to the walls of the test tube, a weighing paper cylinder is used to transfer the methylammonium halide into the tube.

The tube is connected to a Schlenk line equipped with a rotary pump: the rube is evacuated and the pressure adjusted at 0.185 Torr. Then the test tube is immersed in a silicone oil bath pre-heated to 120°C, with a magnetic stirrer (600 rpm) for 2 hours (pre-conditioning of the Schlenk tube).

When the setup is not used the loaded tubes are maintained under N_2 flow and after 3 uses the old MAX powder is substituted with fresh powder.

5.1.3.2.2. Precursor Preparation

The precursor solution is obtained dissolving PbI_2 (0.8 mmol, 0.369 g) and $PbBr_2$ (0.2 mmol, 0.073 g) in 1 mL DMF to achieve a final concentration of 0.8 M of PbI_2 and 0.2 M of $PbBr_2$. The solution is dissolved with ultrasonic bath and slightly heating the solution (110°C). The so obtained solution is then filtered with a polytetrafluorethylene (PTFE) syringe filter with the porous size of 0.2 µm.

5.1.3.2.3. Lead Halide Deposition

The solution is pre-heated at 110°C then 90 µL are dropped onto the sample which is slowly rotating during the first 5” of the spin coating process. The spin coating program

is divided in two steps: 5" at a speed of 500 rpm followed by a rotation speed of 1500 rpm for 3 min. The precursor film is dried for 15 min at 110°C on a hot plate under flowing N_2.

5.1.3.2.4. Vapor-Assisted Annealing

The sample is loaded into the Schlenk tube (prepared according to instructions in section 1.2.2.1.1) and the pressure adjusted to 0.185 Torr. The sample sits in the test tube above the methylammonium halide without being in direct contact with it. To slow down incorporation of methylammonium, the lead halide surface is oriented to face away from the methylammonium halide. The test tube loaded with the sample is immersed in silicone oil bath heated to 120°C for 2 hours. After this time the sample is taken out and quickly rinsed by dipping the substrate in a beaker containing isopropyl alcohol. It is then immediately dried with a N_2 gun. At that point the substrate is coated with Spiro-OMeTAD or with the protective poly(methyl methacrylate) PMMA depending on the following experiments.

5.1.3.3. $CH_3NH_3PbI_3$ Solution Process[10]

The solution process method is used at the IOM-CNR labs to fabricate both devices and the substrates for the T-NIL and P-NIL. The perovskite precursor solution was prepared by mixing CH_3NH_3I and PbI2 at a 3:1 and 1: molar ratio in anhydrous N,N-dimethylformamide (DMF, from Sigma-Aldrich) to give a concentration of 30 wt%. The quantity used for the 3:1 ratio are 0.2g PbI_2 (0.4 mmol) and 1.2 g MAI (1.2 mmol) in 1 mL of DMF. For the MAI/PbI_2 1:1 in 1 mL of the same solvent are dissolved 0.302 g (0.7 mmol) of PbI_2 and 0.104 g (0.7 mmol) of MAI.

Before spin coated the solution is filtered with a syringe filter porous size of 0.45 µm. The deposition is done inside the glovebox in low humidity and low oxygen atmosphere by spin coating the solution at 2000 rpm for 1 minute then annealing the sample at 95 °C for 15'. For the imprinting process the layer is dried for 2' at 95 °C to keep the film partially wet.

5.1.4. Spiro-OMeTAD Deposition[5]

The precursor solution for the hole transport layer was prepared by dissolving 80 mg spiro-OMeTAD (Lumtec, 99.5%), 28.5 µL 4-tert-butylpyridine (Sigma- Aldrich, 96%) and 17.5 µL lithium-bis(trifluoromethanesulfonyl)imide (Li-TFSI, Sigma-Aldrich, 99.95%) solution (520 mg Li-TFSI in 1 mL acetonitrile) in 1 mL chlorobenzene (Sigma-Aldrich, 99.8%). The HTL was deposited by spin coating at 3000 r.p.m. for 30 s in air. After the spin coating the sample is leaved in a desiccators overnight to allow the doping of het material with the oxygen.

5.1.5. Gold Evaporation

A 100-nm-thick Au layer is deposited on top of the HTL through a metal shadow mask by EB evaporation at a base pressure of about 4 x 10^{-6} Torr and a deposition rate of about 1.5 Å/s. The active area for the solar cells is 0.065 cm^2.

5.2. Sequential Dipping for Cubic-like $CH_3NH_3PbI_{3-x}Br_x$

This process is performed onto the glass/FTO/TiO_2 substrate during the optimization of the deposition and for the characterizations with SEM, UV-vis, XRD and c-AFM measurements. For the PL measurements the layer is deposited onto cleaned (see section 5.1.1) bare glass.

The dipping process consists in two main steps: the precursor deposition and the conversion of the layer after dipping in MAX/IPA solution.

The precursor solution is obtained dissolving PbI_2 (0.8 mmol, 0.369 g) and $PbBr_2$ (0.2 mmol, 0.073 g) in 1 mL DMF to achieve a final concentration of 0.8 M of PbI_2 and 0.2 M of $PbBr_2$. The solution is dissolved with ultrasonic bath and slightly heating the solution (110°C). The so obtained solution is then filtered with a polytetrafluorethylene (PTFE) syringe filter with the porous size of 0.2 µm. The solution is pre-heated at 110°C then 90 µL are dropped onto the sample which is slowly rotating during the first 5" of the spin coating process. The spin coating program is divided in two steps: 5" at a speed of 500

rpm (solution dropping) followed by a rotation speed of 1500 rpm for 3 min. The precursor film is dried for 15 min at 110 °C on a hot plate under flowing N_2.

The lead halide thin film deposited onto the substrate is subjected to a pre-wet step lasting 10" to enhance the quality of the conversion during the dipping. Then it is immediately dipped into the MAX/IPA solution leaning on the bottom of the glass container faced up. The MAI solution has a concentration of 50.3 x 10^{-3} M (8 mg/mL) while for the MABr it is equal to 44,7 x 10^{-3} M (5 mg/mL). During the optimization steps of the MABr/IPA dipping the concentration of MABr in IPA is lowered to 26.8 x 10^{-3} M (3 mg/mL) and to 8.9 x 10^{-3} M (1 mg/mL).The isopropyl alcohol is anhydrous (99.5%, Sigma-Aldrich) and fresh spilled before each set of experiments.

The dipping step lasts for the desired time (from 30" up to 300") and is performed without any shacking neither stirring of the system.

After the dipping step the sample is dried with N_2 gun and annealed at 110 °C for 10 minutes. For the multiple dipping experiments the same procedure is repeated for the desired number of times (2 or 3).

5.3. Combination of the Sequential Dipping and the LP-VASP

To optimize the conversion degree of the cubic perovskite crystals the LP-VASP was implemented to the dipping process. Once the cubic morphology is obtained (after the dipping process) the sample is immediately loaded in the test tube and connected to the Schlenk line. At that point the LP-VASP is run as usual (see Section 5.2.2.2).

5.4. T-NIL and P-NIL Processes

The thermal imprinting process of the halide perovskite material is carried out in the glovebox with controlled levels of oxygen and humidity (see section 5.6.2). The pulsed technique on the other side performed in air conditions with the humidity ~ 60-70% and at the temperature of 20-21 °C (clean room - class 100).

5.4.1. T-NIL protocol

The sample with spin coated $CH_3NH_3PbI_3$ (solution process) is mildly dried for 2' at 95°C. With longer annealing time the layer is to crystalline to be imprinted while with no annealing part of the layer remains sticked on the mold.

The nano-patterned master is placed on the lower plate and on it the substrate: the plates are then moved and put in contact with the master/sample system and heated to 100°C once the temperature is reached the pressure of 50 bar is applied and kept constant for 10 minutes. once the process is complete the plates are cooled at RT and the pressure released. With the help of a razor blade the sample is separated from the mold.

5.4.2. P-NIL protocol

The sample is spin coated via solution process in the glovebox then annealed for 2' at 95°C. It is immediately transported from the glovebox to the ULISS setup and the place in the press system. On the lower plate there is the master with integrated heating system and on it the perovskite sample is placed. The intensity of the pulse (from 200V up to 800V) and the pressure (from 50 up to 100 bar) are set and the process initialized. Automatically the pressure is applied then the pulse is generate. The pressure is released and the sample dived from the master.

5.4.3. Fabrication of Nano-structured Masters

Below I report the fabrication of the two masters with the nanostructures suitable for the total internal reflection (pyramidal and V-groove). The main approach it to exploit the anisotropic wet etching of the silicon (100) substrate with KOH solution.

5.4.3.1. Fabrication of Pyramid-Structured Master

A silicon (100) substrate is cleaned in H_2SO_4:H_2O_2 - 7:3 piranha - solution at 95°C for 5 minutes followed by oxygen plasma treatment. A SiO_2 film (25 nm) is growth by oxidation (O_2) on the substrate for 32 min at 1000°C. The sample is again cleaned in piranha solution as before described for the SiO_2 deposition. After cleaning, the imprinting resist mr-I 7030 (microresist GmbH) is spin coated at 3000 rpm then heated at

140 °C for 2’ (soft baking) resulting in 300 nm of thickness. The substrate is then thermally imprinted (T-NIL) with a silicon master having an array of pillars (period 800 nm, diameter 250 nm and height 300 nm): the process is done at 100 °C applying a pressure of 10 MPa for 15’. Once the time is finished, the hot plates of the press are cooled down at 35 °C then the pressure released (**Figure 5.4**).

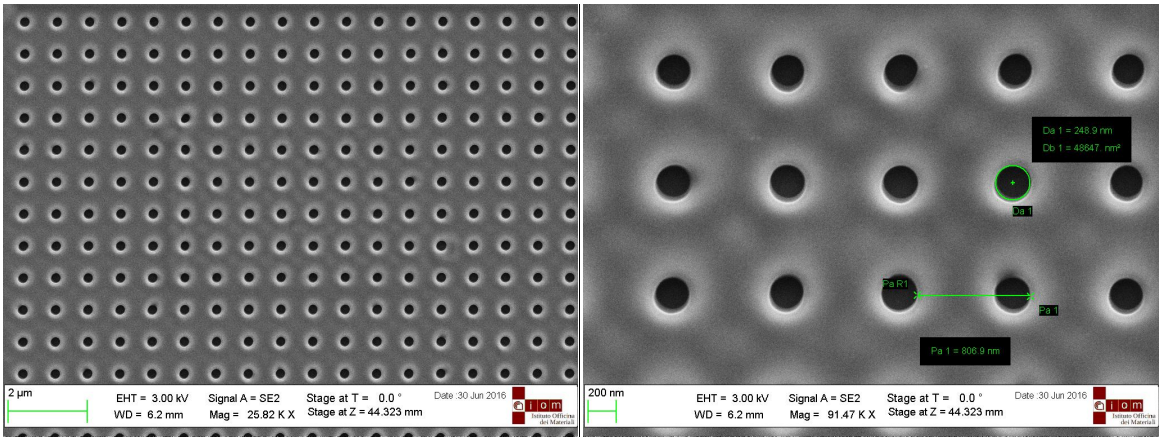

Figure 5.4: imprinted circular holes after T-NIL

The residual layer of the resist is removed *via* controlled oxygen plasma (15”) using ICP plasma etcher (Coil Power 200 W, Platen Power 10 W, O2 Flow 40 sccm, Pressure 4mTorr, BIAS 35 V). The pattern is transferred to the SiO_2 layer using a Buffered Oxide Etching solution (BOE 7:3 - *j.T. Baker*): the substrate is immersed in the solution for 30” then rinsed by water. The desired structures are then obtained by wet anisotropic KOH etching: in particular a KOH 30%wt solution is heated at 80 °C then the silicon substrate immersed for 15” afterward rinsed by water. Before using the master with the so obtained inverted pyramids it is necessary to remove the SiO_2 mask using again the BOE solution (1’ in excess). The nanopatterned substrate is again cleaned H_2SO_4:H_2O_2 - 7:3 piranha - solution at 95°C for 5 minutes followed by oxygen plasma treatment. The anti-sticking layer of octadecyltrichlorosilane is deposited *via* evaporation in a vacuum chamber for at least 10 hours (overnight).

5.4.3.2. Fabrication of V-groove Master

A SiO_2 film is obtained by wet oxidation of a doped-silicon substrate for 32 min at 1000°C. After cleaning (in H_2SO_4:H_2O_2 - 7:3 piranha - solution at 95°C for 5 minutes followed by oxygen plasma treatment) the substrate is coated with an adhesion promoter

(HMDS – Microchem) and then with S1805 (MICROPOSIT ™) photoresist diluted into propylene glycol monomethyl ether acetate (PGMEA) (Microresist Technology) (2 : 3) by spin coating at 4000 rpm for 30 s. After soft baking (115 °C, 1 min.) the sample is exposed by Laser Interference Lithography (LIL) with a dose of 110 mJ cm^{-2} and at an incidence angle of 15.7°, using a Lloyd configuration LIL setup.[11] Development is performed in MF-321 (MICROPOSIT™) for 26 s and finally the sample is thoroughly rinsed in milliQ water. For the LIL step we used a lab-made Lloyd's configuration setup with a 50 mW Helium Cadmium (He-Cd) laser emitting a TEM_{00} single mode at 325 nm was used.

A buffered oxide etching (BOE - Microchem) process is used to remove the SiO_2 layer in correspondence of the exposed photoresist portions. The sample is left in the BOE solution at room temperature for 32 sec, rinsed in milliQ water and then in acetone at 60°C to remove residual photoresist. A Potassium Hydroxide/Isopropyl Alchool (KOH/IPA) solution (60°C , 10 min.) is used for the silicon etching. A BOE solution is then used to remove the SiO_2 residual layer by immersing the sample in the etchant for 2 min. Finally the nanostructured substrate is cleaned in a 7:3 piranha solution before the deposition of the metallic contacts by sputtering necessary for the connection of the mold to the ULISS machine. The anti-sticking layer of octadecyltrichlorosilane is deposited *via* evaporation in a vacuum chamber for at least 10 hours (overnight).

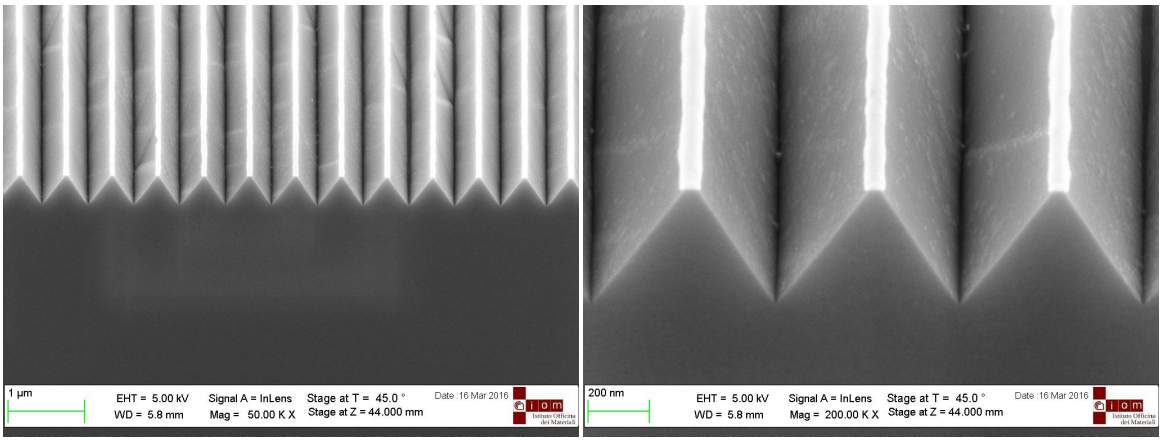

Figure 5.5: V-groove nano-structured Si master

5.5. Characterization Tools

Electrical atomic force microscopy Conductive AFM and photo-conductive AFM are electrical AFM techniques which allow for the simultaneousmeasurement of surface topography and current. While in C-AFM, a DC voltage bias is used as stimulus, an optical excitation is used as stimulus in PC-AFM to drive current. All the electrical AFM measurements are done using a Park AFM NX10 which is encased in a Nitrogen glovebox to prevent sample degradation. The Relative Humidity in this chamber during the measurements is kept <1%. Commercially available Pt/Ir coated tips with spring constant of 2.8 N/m are used in these measurements.

For PC-AFM, the sample is illuminated from the top using a white LED with an output wavelength from 375 nm to 800 nm. Keeping in mind that initial light exposure can modify the performance oflead halide solar cells, the samples were light soaked for at least an hour before electrical AFM measurements were acquired.

Sun Simulator J-V characteristics of the solar cells were measured in air using a solar simulator (Newport, 91192) equipped with a 150-W Xe lamp and an AM 1.5G filter as light source and a Keithley 2400 source meter. Light intensity was calibrated with an NREL-calibrated Si solar cell with a KG-5 filter to 1 sun (100 mW/cm2).

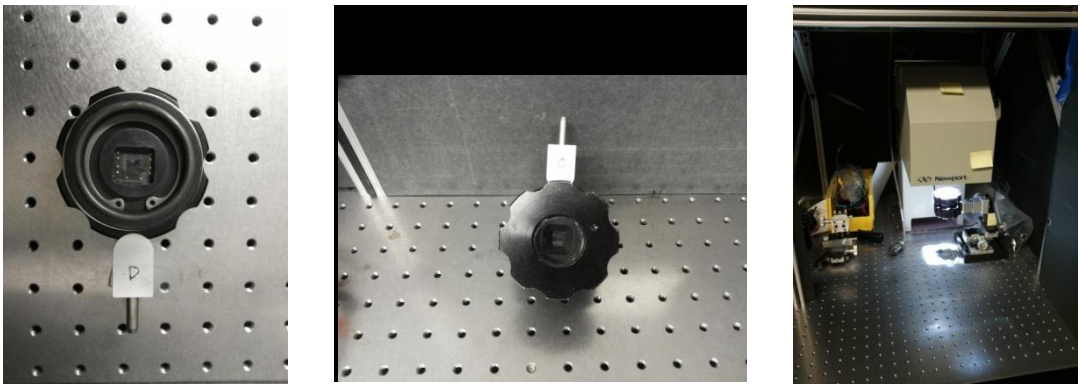

Figure 5.6: Solar cell holder and Sun Simulator

Steady-state photoluminescence measurements are obtained with a home-built micro-PL setup using the 514.5 nm line of an Ar ion laser. Measurements were conducted in ambient conditions (20° to 21°C, 40 to 60% relative humidity). The measurements are conducted by focusing the laser beam onto the sample using an 80× objective (MD plan, NA = 0.9, ~3 µm2 spot size) and the PL signal is collected through the same objective and

detected by a Si CCD camera (Andor iDus BEX2-DD). Before each measurement the background was taken and subtracted from the actual PL measurement.

SEM The SEM images of the samples were acquired using a FEI QUANTA FEG 250, Zeiss Supra 40 SEM with a Gemini EFSEM column or JEOL EB6300FS EBL system.

Figure 5.7: SEM FEI QUANTA FEG 250

XRD patterns of the samples were measured with a Rigaku SmartLab X-ray diffractometer using Cu Kα radiation at 40 kV and 40 mA. Medium resolution spectra are collected in grazing incidence conditions (parallel beam parallel slit analyzer PB/PSA).

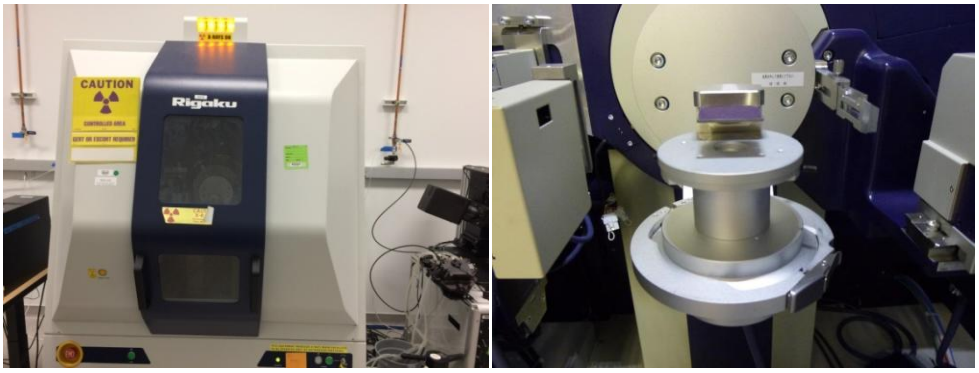

Figure 5.8: Rigaku SmartLab XRD

Absorbance (A) measurements were taken at room temperature with a SolidSpec-3700 UV-VIS-NIR spectrophotometer (SHIMADZU).

Figure 5.9: UV-vis setup for Absorbance characterization

5.6. Various Setup

5.6.1. P-NIL: ULISS setup[12]

The ULISS setup consists of two modules, a process module and an auxiliary module. In the process module, a class 10 mini-environment is enclosed in a Faraday cage and contain an hydraulic press. A high-voltage pulse generator is located under the Faraday cage. The auxiliary module essentially contains a high-voltage dc power supply, a hydraulic pump, and the electronics controlling the entire system via computer (using a National Instruments cRIO 9074 PLC, and FPGA – LabVIEW interface). The system can deliver pulses of 35, 70 and 105 µs, up to 30MW power. In addition, it can also operate as a standard thermal NIL tool up to 350 °C (with fast heating and cooling), or even in a mixed standard-NIL/pulsed NIL mode.

5.6.2. T-NIL setup and T-NIL Glovebox Setup

The thermal-NIL setup is basically a press composed by two large plates with the possibility to be heated up to 200 °C. An hydraulic system is connected to the plates and the pressure is finely adjusted thanks to a digital monitor. A smaller version is also installed in the glovebox but with samples with 25 x 25 mm^2 the maximum pressure is about 50 bar.

5.6.3. Glove box and Spin Coater (IOM-CNR)

At the IOM-CNR facility the steps concerning deposition or treatments of the ETM, the photoactive layer and HTM were performed inside a glovebox bought from GS Glovebox Systemtechnik (Germany). The glovebox is equipped with a solvent and particle filtering system, is nitrogen filled with a continuous nitrogen flow. The content of oxygen and water inside the glove box are respectively 50-500ppm and 50-80ppm, monitored with a O2X1 Oxygen Transmitter from Ge Infrstructure Sensing Inc (US). and a Easidew Hygrometer from Michell instruments.

The spin coating of the materials were performed using a bench spin coater from Laurel technology model WS-650SZ-GnPP/lite installed inside the glovebox.

5.7. Reference

1. Yanbo Li, Carolin M. Sutter-Fella, Nicola Cefarin, Aya K. Buckley, Quyhn P. Ngo, Ali Javey, Ian D. Sharp, F. M. T. Low Pressure Vapor-Assisted Solution Process for Tunable Band Gap Pinhole-free Methylammonium Lead Halide Perovskite Films. *J. Vis. Exp.* (2017).
2. Lee, M. M., Teuscher, J., Miyasaka, T., Murakami, T. N. & Snaith, H. J. Efficient hybrid solar cells based on meso-superstructured organometal halide perovskites. *Science* **338,** 643–7 (2012).
3. Docampo, P., Ball, J. M., Darwich, M., Eperon, G. E. & Snaith, H. J. Efficient organometal trihalide perovskite planar-heterojunction solar cells on flexible polymer substrates. *Nat. Commun.* **4,** 2761 (2013).
4. Li, Y. *et al.* Defective TiO2 with high photoconductive gain for efficient and stable planar heterojunction perovskite solar cells. *Nat. Commun.* **2,** 1–18 (2016).
5. Li, Y. *et al.* Fabrication of planar heterojunction perovskite solar cells by controlled low-pressure vapor annealing. *J. Phys. Chem. Lett.* **6,** 493–499 (2015).
6. Sutter-Fella, C. M. *et al.* High Photoluminescence Quantum Yield in Band Gap Tunable Bromide Containing Mixed Halide Perovskites. *Nano Lett.* **16,** 800–806 (2016).
7. Gonzalez-Carrero, S., Galian, R. E. & Pérez-Prieto, J. Maximizing the emissive properties of CH 3 NH 3 PbBr 3 perovskite nanoparticles. *J. Mater. Chem. A* **3,** 9187–9193 (2015).
8. Zhou, H. *et al.* Antisolvent diffusion-induced growth, equilibrium behaviours in aqueous solution and optical properties of CH3NH3PbI3 single crystals for photovoltaic applications. *RSC Adv.* **5,** 85344–85349 (2015).
9. Leblebici, S. Y. *et al.* Facet-dependent photovoltaic efficiency variations in single grains of hybrid halide perovskite. *Nat. Energy* **1,** 16093 (2016).
10. Zhang, W. *et al.* Ultrasmooth organic-inorganic perovskite thin-film formation and crystallization for efficient planar heterojunction solar cells. *Nat Commun* **6,** 6142 (2015).
11. Zacco, G. *et al.* Microelectronic Engineering Sinusoidal plasmonic crystals for bio-detection sensors. *Microelectron. Eng.* **88,** 1898–1901 (2011).

12. Tormen, M., Sovernigo, E., Pozzato, A., Pianigiani, M. & Tormen, M. Sub-100 l s nanoimprint lithography at wafer scale. *Microelectron. Eng.* **141,** 21–26 (2015).

Conclusion

During this Ph.D. project, I studied how to control the growth and pattern organo-lead halide perovskites.

This photoactive material was successfully synthesized and characterized through several techniques. In particular, we achieved control on the morphology, thereby obtaining perovskite cubes with interesting optoelectronic properties. The fabrication of the SC devices was achieved, and the efficiency measurements were performed to evaluate the quality of the complete stack. The LP-VASP was used to deposit the methylammonium lead iodide perovskite leading to SC with high performance (PCE of 15.9 %), and low hysteresis behavior.

Several deposition methods of the organo-lead halide perovskite were learned and studied: they are the solution process, the sequential dipping deposition and the LP-VASP. To deposit well faceted halide perovskite grains for pc-AFM characterization a new protocol was successfully developed: a similar version of the sequential dipping deposition was exploited to grow $CH_3NH_3PbI_{3-x}Br_x$ cubic-like crystals controlling the dimensions. Moreover the implementation of the LP-VASP was the fundamental progress needed to obtain layers of fully converted cubic crystals. The morphology and the chemical-physical properties were characterized *via* SEM, XRD, UV-vis and PL.

To understand the relationship between photo-generated current and cube's facets, we performed pc-AFM characterization. We found indication that the current assumes different values on different facets of the same grain. In addition, a dimension-dependence was noticed: bigger grains generate less current than the smaller ones and this trend is consistent with PL measurements. These data show the necessity to control the deposition and finely direct the growth of the halide perovskite photoactive crystallites to avoid the presence of electrically low conductive domains affecting the overall efficiency of the PV device. Despite the still controversial relation between the optoelectronic properties and the dimension of the crystals, from the PL maps it was noticed that smaller grains are more photoactive than bigger grains.

In addition, a nano-fabrication approach was used to transfer pyramidal and V-groove structures to the photoactive material. The silicon master were successfully fabricated exploiting different NIL techniques as the T-NIL and the LIL. The first trials with T-NIL showed the possibility to imprint the methylammonium lead iodide while with P-NIL the process was optimized. The imprinting with the pyramidal structures showed low homogeneity and often the nano-structures are tear off from the surface. On the other side the V-groove geometry showed immediately higher homogeneity during the transfer of the pattern. Moreover the mechanical resistance given by this geometry prevents undesired pealing of the structures. This result opens the possibility to implement the PV devices with nanostructured layers to enhance the total efficiency. Depending on the dimensions and the geometry of the structures the imprinting process might lead to homogeneous uniform imprinting. Changing the geometries and/or the structures is a promising new path to enhance the performance of the perovskite used for other optoelectronic applications.